Title
Theory, Design, and Fabrication of Nanoplasmonic Architectures for Molecular Diagnostics

Author
Ross, Benjamin Maxwell

Publication Date
2011

Peer reviewed|Thesis/dissertation

THEORY, DESIGN, AND FABRICATION OF NANOPLASMONIC ARCHITECTURES FOR MOLECULAR DIAGNOSTICS

By

Benjamin Maxwell Ross

A dissertation submitted in partial satisfaction of the

requirements for the degree of

Doctor of Philosophy

in

Applied Science and Technology

in the

Graduate Division

of the

University of California, Berkeley

Committee in charge:

Professor Luke P. Lee, Chair
Professor Ming Wu
Professor Ronald Fearing

Spring 2011

Abstract

Theory, Design, and Fabrication of Nanoplasmonic Architectures
for Molecular Diagnostics

by

Benjamin M. Ross

Doctor of Philosophy in Applied Science and Technology

University of California, Berkeley

Professor Luke P. Lee, Chair

This dissertation presents new advancements in the theory, design, and fabrication of nanoplasmonic structures for molecular detection.

After introducing nanoplasmonics, I ask a deceivingly simple question: are the various commonly used measures of localized surface plasmon resonance (LSPR) really equivalent? I then develop a theoretical framework that proves that important differences occur among the measures of LSPR. Specifically, the optimum wavelength for maximizing the near field can be significantly redshifted compared to the optimum wavelength for far field scattering, which can in turn be significantly redshifted compared to the optimum wavelength for absorption. I show how these differences are dependent upon critical parameters, such as the material, the particle size, and particle shape. This theory, based on the quasi-static approximation, is also verified rigorously using using Mie theory and finite element analysis. The implications on design for molecular detection are discussed.

I then focus on fabrication techniques, developing new tools which can control the geometry and interparticle distance of nanoplasmonic antenna initially fabricated with nanosphere lithography. I introduce active polymer fabrication and electroless metal deposition as two methods that can significantly decrease the nanogaps in nanoplasmonic systems and create enhancements in spectroscopic signal for molecular detection.

Next, I investigate the issue of nanoplasmonic geometry in great detail for four structures, with a focus on new systems in which the close proximity of two or more nanoplasmonic components causes their resonances to be linked together (i.e. plasmon-coupling). I demonstrate the coupling in these structures can cause high electric fields ideal for molecular detection. Four such structures are discussed: the

nanocrescent, the crescent-shaped nanohole, the plasmon enhanced particle-cavity (PEP-C) system, and the core-satellite system. The nanocrescent and its counterpart, the crescent-shaped nanohole, utilize both sharp tips and intra-particle coupling to achieve high local field enhancement. The PEP-C system combines particle and cavity geometries to create a high density of hot-spots. The core-satellite system is based on the interaction of a central nanoparticle with multiple smaller particles.

Finally, I introduce a special class of bioinspired nanoplasmonic structures called nanocorals, designed for molecular sensing within or on the surface of living cells. Nanocorals are unique in that they combine cellular specific targeting with biomolecular sensing, yet decouple the two functional modes. Analogous to natural sea corals that use rough surfaces to maximize surface area for efficient capture of light and food particles, nanocorals utilize a highly roughened surface at the nanoscale to increase analyte adsorption capacity, and create a high density of surface-enhanced Raman spectroscopy (SERS) hot-spots.

Table of Contents

List of Figures

Acknowledgments

Firstly, I thank my adviser, Luke Lee, for his patience, unfailing support, and advice throughout my years at Berkeley.

Many BioPOETS have been a great help in the work that makes up this dissertation. Liz Wu has been a close collaborator during my time as a BioPOET, and I thank her for enjoyable and productive collaboration. Thanks to Savas Tasoglu for his collaboration on near and far field plasmonic computations. John Waldeisen and Tim Wang were great collaborators in the study of core-satellite nanoparticle systems, and I thank them for the opportunity to work on this project.

Discussions with SoonGweon Hong led me to begin investigating many of the theoretical results comparing near and far field scattering of nanoplasmonic systems; his dedication and inquisitive mind is unmatched. Also I thank Professor Xiang Zhang for his support on near/far field theory, which originated as a project in his plasmonics class. Yolanda Zhang has been a constant guru for biological experiments, Yeonho Choi has been taught me many spectroscopy techniques, Eric Lee has answered my almost daily "chemistry question of the day" with a smile and without fail.

Jason Silver has been a dedicated undergraduate collaborator for over 2 years. I thank him for his dedication and help on many projects, particularly PEP-C and electroless deposition, which was also advanced significantly by Ben Fortson. Edwin Lee has been a great help in unravelling the mysteries of nanoplasmonic trapping and other projects. I also thank summer students Crystal Bray and Lance Zhang for their contributions to active polymer fabrication.

Additionally, I don't believe there is a single labmate during my time as a BioPOET who has not helped me in some way or another. I sincerely thank each one of them.

Thanks is also due to my previous advisor Aklesh Lakhtakia of the Engineering Science and Mechanics department at Penn State. He taught me many of the fundamentals of electromagnetics theory.

I also appreciate Yu-lin Xu for making his GMM Fortran code publicly available.

Finally, I deeply appreciate the NSF and Berkeley for providing fellowships (NSF graduate research fellowship and The Berkeley Fellowship) during my time as a graduate student.

List of Acronyms

AFM	atomic force microscopy
FEM	finite element method
FDTD	finite difference time domain
POC	point-of-care
LSPR	localized surface plasmon resonance
SPR	surface plasmon resonance
SERS	surface-enhanced raman spectroscopy/scattering
SEF	surface-enhanced fluorescence
SEM	scanning electron microscopy
PRET	plasmon resonance energy transfer
LFE	local field enhancement
μm	micrometer (10^{-6} meters)
nm	nanometer (10^{-9} meters)
M	molarity
TEM	transmission electron microscopy
IR	infrared
NIR	near infrared

List of Principal Symbols and Operators

Symbols

a	nanoparticle radius
$\mathbf{a}$	acceleration
α	particle polarizability
$\mathbf{B}$	magnetic field
c_0	speed of light in free space
d_{sat}	surface-to-surface distance between the core and satellite particles
$\mathbf{D}$	electric induction field
ϵ	complex relative permittivity
ϵ_0	permittivity of free space
ϵ_m	permittivity of the surrounding medium
$\mathbf{E}$	electric field
$\mathbf{E}_i$	incident electric field
$\mathbf{F}$	force
γ	damping factor
$\mathbf{H}$	magnetic induction field
$\mathbf{H}_i$	incident magnetic induction field
i	$\sqrt{-1}$
$\mathbf{J}$	external current density
k	free-space wavenumber
λ, λ_0, λ_i	free-space wavelength
μ	relative permeability
μ_m	permeability of the surrounding medium
μ_0	permeability of free space
$\mathbf{M}$	magnetization
n_{sat}	number of satellite particles in the core-satellite system
$\mathbf{n}$	outward facing unit normal
ω	angular frequency
$\mathbf{P}$	polarization
r	radial position
r_{core}	radius of the central particle in the core-satellite system
r_{sat}	radius of the satellite particle in the core-satellite system
σ	external charge
t	time
θ	angle of incidence with respect to z axis
x, y, z	Cartesian coordinates

Operators

$\{.\}^*$	complex conjugate
$\{.\}^{-1}$	inverse
$\mathrm{Im}\{.\}$	imaginary part of
$\mathrm{Re}\{.\}$	real part of
$\{.\}^S$	symmetric component of
$\times$	cross product
∇	gradient operator
$\cdot$	dot product

Chapter 1

Introduction to Nanoplasmonics

"Whoever is careless with the truth in *small* matters cannot be trusted with important matters."

Albert Einstein

1.1 Introduction to Nanoplasmonics

1.1.1 What is Nanoplasmonics

The term "nanoplasmonics" is a compound word, which may be at first intimidating. The first part "nano," referring to the nanometer length scale (on the order of 10^{-9}), is familiar enough to modern engineers and scientists, but what of this "plasmonics?" Actually, this term also is related to a more familiar term: "plasma." A plasma is a gas-like state of matter in which some electrons are ionized from their host atoms. While a plasmon is distinct from this state, both plasmas and plasmons share the common theme of the motion of electrons distinct from their host atoms.

Plasmons occur in conductive solids, and are most strong in highly conductive metals such as gold or silver. As commonly learned in the introductory study of materials, these metals are conductive because of the presence of free electrons. That is, there are electrons which are not bound to specific atoms, and can move across the solid. Under certain conditions, these free electrons can become coupled to an incident electromagnetic wave, and can propagate either along the surface (surface plasmon) or through the volume (volume plasmon) of the metal.

Now, to combine "nano" and "plasmonics" we ask, what happens if we take a very small volume of a metal, for example a nanoparticle, and apply an electromagnetic wave? That is the precisely the question that concerns this dissertation. In this chapter, we will review the current state of what is known about this question, with a particular focus on how such a system may be used for molecular diagnostics.

1.1.2 The Field of Nanoplasmonics

We are in the midst of a surge of interest in plasmonics, and in particular nanoplasmonics. Over the past decade, plasmonics has seen over a fourfold increase in publications. In particular, nanoplasmonics[1] has truly exploded, with only a handful of papers published annually in the mid 1990s to over 600 in 2008. Starting near the turn of this century clearly something is drawing much interest to the field.

Therefore, it may be surprising that the fundamental understanding of nanoplasmonics was established at the turn of the *previous* century. Mie solved the exact solution for electromagnetic scattering by a sphere of arbitrary size and homogeneous composition in 1901 [2], and Drude established his model for the permittivity of metals in 1900 [3, 4]. So what has caused the sudden interest in this old subject?

First, several fabrication advances have facilitated the creation of metallic nanostructures. For example, progress in colloidal science has allowed monodisperse solutions of particles of a wide range of sizes and geometries to become available. Many

[1] roughly calculated by the search terms plasmon* and nanoparticle

can be fabricated in 1-2 days work, or purchased commercially. Bottom-up or wet fabrication techniques for attaching a monolayer of these colloids to surfaces have become widespread. Additionally nanosphere lithography, pioneered by the van Duyne group and others, has provided another route for the inexpensive and rapid fabrication of nanoplasmonic structures [5]. Other tools such as electron-beam lithography, focused ion beam lithography, and nanoimprint lithography have allowed the fabrication of a wide range of structures. Because of the growth of nanotechnology in general, these machines, as well as characterization equipment such as scanning electron microscopy (SEM), transmission electron microscopy (TEM), and atomic force microscopy (AFM) have become widespread.

In addition to these experimental advances, advances in computing power have only recently made the theoretical study of complex nanosystems feasible. While Mie's theory and its extensions are exact for spherical particles, nonspherical structures, particularly those with sharp features, must be solved with computationally intensive numerical techniques such as the finite element method (FEM) and finite difference time domain (FDTD) method. Even in the past 5 years, the improvements in computer power and software have drastically increased the number of scenarios which can be solved on a personal computer.

Finally, and perhaps most importantly, several promising applications and fundamental advances have emerged for nanoplasmonics. In 1997, Kneipp et al. showed single molecule detection using surface-enhanced Raman spectroscopy (SERS) with nanoplasmonic silver particles [6]. In 1998, Ebbesen et al.'s observation of extraordinary optical transmission through subwavelength holes brought wide interest to the field [7]. The conceptual understanding of nanoplasmonics as optical electronics has attracted attention in creating optical circuits [8]. More recently, light generation in nanoplasmonic structures has attracted interest [9]. Halas' group has pioneered the use of nanoplasmonic particles for photothermal cancer therapy [10]. In short, nanoplasmonics is blossoming into a field that touches physics, chemistry, materials science, electrical engineering, and bioengineering.

We will now introduce the mathematical and conceptual fundamentals of nanoplasmonics. For a thorough introduction to plasmonics, Stephan Maier's *Plasmonics: Fundamentals and Applications* [11] is recommended. In addition, a thorough understanding of time-harmonic electromagnetic waves is also highly useful, e.g. Jackson's classic textbook [12, ch. 7]. We begin will a purely conceptual description of nanoplasmonics, and then proceed to a more rigorous mathematical approach.

1.2 Conceptual Understanding of Nanoplasmonics

Fortunately, many of the important features of nanoplasmonic systems can be understood intuitively, with analogies to familiar oscillator systems. In this section[2], we develop a completely nonmathematical interpretation of resonance in nanoplasmonic systems and its importance to biomolecular detection. The goal is to make a wide variety of nanoplasmonic phenomena intuitively clear to a reader with a high school level background of physics. While the analogies presented have their limits, they are very useful in developing a mental picture of plasmonic phenomena. In the following subsection, we will turn to a more rigorous mathematical understanding.

Let us begin by imagining a metal nanoparticle. As long as the particle is large enough (let us say greater than 10 nm), there are abundant free electrons present in the metal. The term "free electron" implies that it is not bound to a particular atom of the nanoparticle–it is free to wander about. However, in general the electrons are not free to leave the nanoparticle, because if they do, they will leave behind the positive "core" of atoms (which do not move). The attractive coulomb force between the stationary positive cores and the free electrons keeps the system in balance.

Now let us imagine that we apply a steady electric field across this nanoparticle (for example, imagine placing the particle in a large parallel plate capacitor). What will happen? The free electrons will tend to migrate over to one side of the particle, until the coulomb force between the displaced electrons and the positive core balances with the applied electric field. Because the free electrons will tend to be on one side of the particle, one side of the particle will show a negative charge, and the other side a positive charge. Simple enough.

Now what happens if we begin to oscillate the applied electric field back and forth (e.g. by switching the charges on the parallel plate capacitor)? If we oscillate it very slowly, the electrons will move to one side, settle, move to the other side, settle, and so forth, behaving quite similar to the case of a static field. If instead we oscillate the electric field extremely fast, the electrons will not have time to move significantly in one direction before the field changes direction. In this case it is as if there is no electric field at all.

But instead what if we imagine an electric field that is oscillating at a "sweet spot?" Just like a child on a swing, we can imagine the electric field oscillating the electrons *in resonance*—just as the electric field is changing direction, the electrons are also being pulled by the coulomb force of the core and traversing across the nanoparticle (and losing some of their energy due to collisions). Therefore, just like the swing, or a mass-spring system, or a pendulum, a nanoparticle should have a resonance, what we call a plasmon resonance, which is this "sweet spot" frequency

[2]This section is loosely based on a presentation (including interpretive dance!) that I gave to undergraduate and new graduate students joining the Biopoets lab in the summer of 2009.

for its free electrons. This concept is the essence of nanoplasmonics.

What is this sweet spot resonance for typical metal nanoparticle systems? It turns out to be quite fast–approximately 500×10^{12} hz for gold. Coincidentally, this happens to be within the narrow range of electromagnetic radiation that humans can readily detect, in the form of visible light (green). Indeed this is quite a fortunate coincidence in creating useful nanoplasmonic sensors, since absorption of common materials such as air, water, glass, and cellular material is low in this regime.

Now that we have developed a basic conceptual understanding of nanoplasmonics, let us apply it to some fundamental questions.

1.2.1 Nanoparticle Size Dependence

What would we expect to occur as the nanoparticle size is increased? If we imagine an electron oscillating back and forth across the positive core, as the particle increases in size, the electron has further to traverse to reach the other side. Assuming the speed of the electron does not change significantly, it must take a longer time time to get across the particle. Therefore, we can predict the resonance of the electron will occur at a *longer* wavelength (i.e. redshift), or lower frequency, as the particle size is increased. This is analogous to a pendulum oscillator system, where a longer pendulum results in a longer wavelength of resonance. In addition, as the particle gets larger, the electron will undergo more collisions with atoms on its way across the particle. Since some energy is lost during these collisions (e.g. dissipated as heat), we can expect more loss to occur for larger particles. Indeed both the redshift and particle loss are predicted with rigorous theory and observed experimentally.

It is worth noting that in our mental model we have assumed the electric field is constant across the distance of the nanoparticle. In other words, the particle size is small compared to the wavelength of light. This regime is called the quasi-static approximation, and is discussed in detail in the next section. When the particle size increases to be significant compared to the wavelength of light, the electric field may no longer be constant across the particle. The incoming wave is "retarded" over the distance of the nanoparticle, and this retardation can introduce some effects which will be considered in more detail in later.

1.2.2 Effect of Surrounding Media

Thus far we have not considered the region surrounding the nanoparticle. How would we expect the plasmon resonance to change if the particle is immersed in different media, e.g. water vs air? Much as we would expect a spring-mass (or pendulum) oscillator to have a longer wavelength as it is immersed in water, we expect a more "optically viscous" medium should slow down the electron and cause the resonance to

redshift. Indeed, this is what is observed, and is the basis for molecular sensing based on localized surface plasmon resonance shift (LSPR-shift). The "optical viscosity" is simply the dielectric constant of the surrounding medium, which is the ratio of the speed of light in air to that in the material; the higher the dielectric constant, the more redshift is observed. Since the electrons cannot move far from the positive core, it is only the dielectric constant within a few nanometers of the nanoparticle that is important to this shift, which is beneficial for sensing. If molecules of interest can be made to specifically attach to the nanoparticle, then we should observe a redshift upon the attachment of these molecules, as long as their dielectric constant is distinct from that of the environment.

1.2.3 Particle-Particle Interactions

What would we expect to occur as two nanoparticles are brought together? Of particular interest is when the nanoparticles are brought very close together, so that their interaction is strong. In this case, the oscillating electrons of one particle are attracted toward the positive core of the adjacent particle, essentially creating a capacitor between the two particles. Intuitively, these forces cause the electrons to take longer to resonate back and forth across the particle, and hence cause a redshift of the resonance wavelength. As the particles get closer together, the effect is more significant, and a greater redshift is expected. Indeed, these effects are observed experimentally in many systems.

1.2.4 Local Electric Field Effects

The electrons which are oscillating due to the incident electric field in turn *generate* an electric field. This is commonly referred to as the scattered field, and can give nanoparticles solution their beautiful color. If we imagine the region within a few nanometers from the nanoparticle, this field can be very high, since we are very close to the electrons. This is called the local field. In fact, the local field can reach approximately 1000 times the incident field. For many applications, it is desirable to increase this local field as high as possible.

Let us consider two common schemes for increasing local fields, and how they can be understood intuitively.

One common scheme is to bring nanostructures extremely close together, separated by small nanogaps of air or dielectric material. The concept of this method can be understood in terms of the particle-particle interactions discussed above: since we can imaging two particle behaving like a capacitor, and since the electric field inside a capacitor is approximately proportional to the inverse of the distance between the walls, decreasing the distance between particles increases the electric field.

A second common scheme is to create ultra-sharp nanostructures. If forcing the electrons onto the edge of the nanoparticle creates a high electric field, then forcing them into a smaller space (i.e. sharp tip) should further increase the electric field. This effect, called the lightning-rod effect, is analogous to the lightning rod effect of electrostatics.

1.2.5 Analogies and Conceptual Frameworks

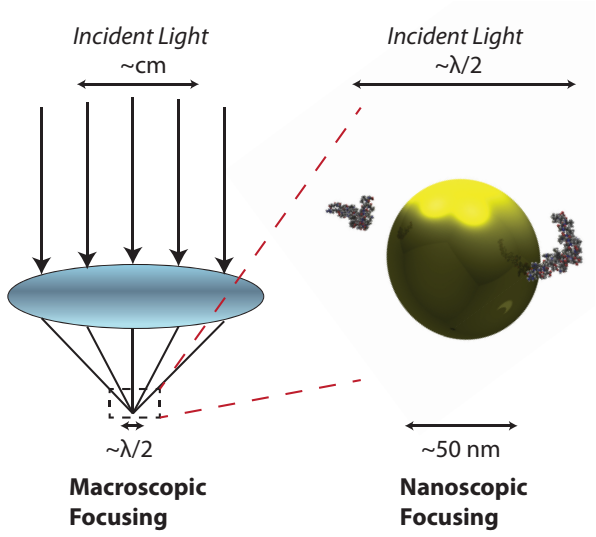

(a)

Figure 1.1: Concept of nanofocusing. Focusing light with traditional lenses is diffraction limited to approximately half the wavelength of the incident light. Nanoplasmonic components allow focusing of light to reach the nanoscale.

In addition to the intuitive framework developed in the previous section, several useful conceptual and mathematical frameworks have been developed in recent years to better understand nanoplasmonic phenomena. These are briefly outlined in this section.

Nanofocusing

Traditional optical lenses are diffraction limited to approximately the wavelength of light divided by 2. That is, the smallest spot to which light can be focused with a traditional lens is $\lambda/2$; or, alternatively, the smallest object that can be resolved by a traditional lens is approximately the size $\lambda/2$. For optical light, this limit is in the range of approximately 200-400 nm. As illustrated in Figure 1.1, nanoplasmonic

components (e.g. gold nanospheres) can be thought of as nanoscale lenses, as they allow focusing of light to regions much smaller than the diffraction limit of $\lambda/2$.

Metamaterials

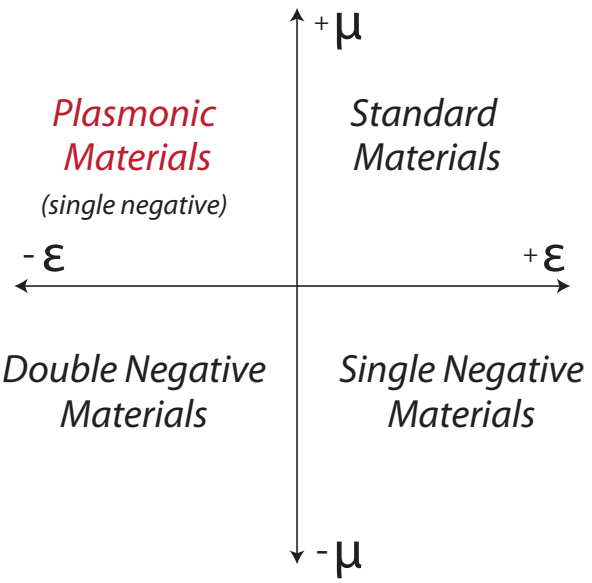

(a)

Figure 1.2: Plasmonics within the framework of metamaterials. Plasmonic materials can be considered "single negative" metamaterials, with a negative permittivity and a positive permeability.

Nanoplasmonics can also be thought of as part of the more general framework of metamaterials, which has received widespread attention recently. Optically speaking, any material can be characterized by its permittivity ϵ, which describes its electric properties, and its permeability μ, which describes its magnetic properties. As illustrated in Figure 1.2, materials can be characterized based on the sign of these two properties. Broadly speaking, metamaterials can be defined as materials that have a negative value for one or both of ϵ and μ. However, most of the focus of metamaterials study is on "double negative" materials; that is, materials that have both negative ϵ and μ. Plasmonic materials fit in this framework as "single negative" metamaterials, since they exhibit a negative ϵ but a positive μ.

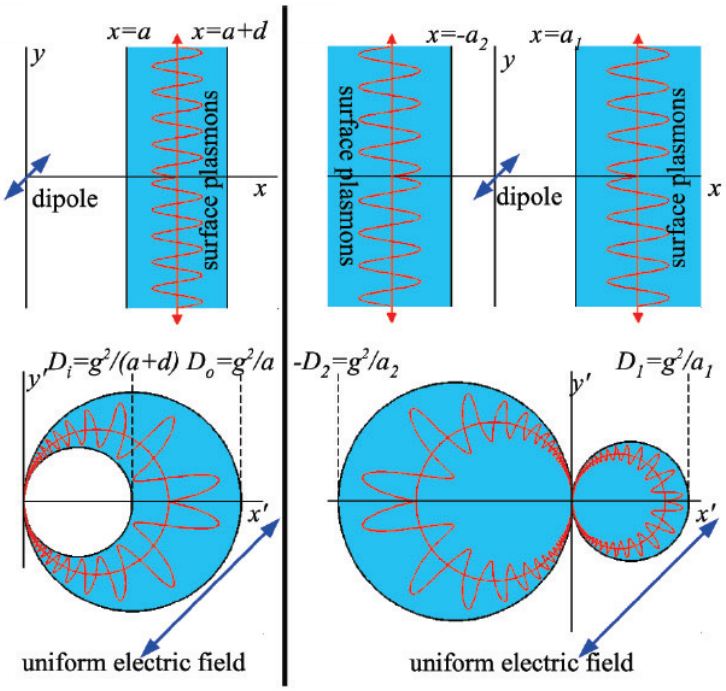

(a)

Figure 1.3: Example of transformation optics. (Top) A thin layer of metal and two semi-infinite metallic slabs separated by a thin dielectric film support surface plasmons that couple to a dipole source, transporting its energy to infinity. (Bottom) The transformed materials are now a cylinder with cross-section in the form of a crescent and two touching cylinders, respectively. The dipole source is transformed into a uniform electric field. From ref. [1].

Transformation Optics

Pendry, the father of the field of metamaterials, has also led development of a framework called transformation optics which can be used to understand metamaterials and metamaterials design. This framework has also been applied for nanoplasmonic design. For example, starting with an ideal plasmonic system that captures a broadband spectrum, a mathematical transformation can be applied to convert the infinite structure into a finite one, while preserving the desired spectrum characteristics [1]. This is demonstrated in Figure 1.3.

1.3 Mathematical Understanding of Nanoplasmonics

In this dissertation, attention is restricted to time–harmonic electromagnetics; that is, we assume that all electromagnetic fields oscillate with a time dependence $\exp(-i\omega t)$. For the vast majority of problems in nanoplasmonics to date this assumption is valid, with the notable exception of femtosecond pulsed laser heating. This assumption is relevant to continuous lasers and white light sources. We assume the surrounding medium is linear, homogeneous, isotropic, nonabsorbing, and has permittivity ϵ_m. The material properties of metal nanoparticles (also linear, homogeneous and isotropic) are modeled by a complex permittivity $\epsilon(\lambda)$, which is a function of wavelength λ. For the nanostructures studied here, we assume the permittivity is the same as that for the bulk metal, which is a valid assumption as long as the particles are large enough such that quantum effects are not significant (typically > 10 nm). We assume the permeability of both the material and surrounding medium are $\mu = \mu_m = 1$, which indicates that materials studied do not have significant magnetic characteristics at optical frequencies.

Let us begin with the time-harmonic Maxwell equations:

$$\nabla \cdot \mathbf{D} = \rho \tag{1.1}$$

$$\nabla \cdot \mathbf{B} = 0 \tag{1.2}$$

$$\nabla \times \mathbf{E} = i\omega \mathbf{B} \tag{1.3}$$

$$\nabla \times \mathbf{H} = \mathbf{J} - i\omega \mathbf{D}. \tag{1.4}$$

Herein, the external charge ρ and current densities $\mathbf{J}$ are zero. The four fields are related by the constitutive relations for linear materials:

$$\mathbf{D} = \epsilon \mathbf{E} = \epsilon_0 \mathbf{E} + \mathbf{P} \tag{1.5}$$

$$\mathbf{B} = \mu \mathbf{H} = \mu_0 \mathbf{H} + \frac{1}{\mu_0} \mathbf{M}\,, \tag{1.6}$$

where $\mathbf{P}$ is the polarization and $\mathbf{M}$ is the magnetization.

In a source-free region, Maxwell's equations (1.1-1.4) can be reduced to a single wave equation, called the Helmholtz equation:

$$(\nabla^2 + \omega^2 \epsilon \mu)\mathbf{E} = 0. \tag{1.7}$$

This is a central result for many propagating wave phenomena.

1.3.1 Drude Model

The Drude model derives the permittivity of a plasmonic material based on simple classical model of a free electron in a metal. Because this model is useful and intuitive,

we go through the derivation here.

Consider a free electron in a metal with an applied electric field acting on it. The total field on the electron will be that due to the electric field, and that due to a damping force γ, which we assume varies linearly with the velocity of the particle. We can then write the equation of motion of the electron from Newton's second law:

$$\mathbf{F} = m\mathbf{a}\,, \tag{1.8}$$

$$(-e)\mathbf{E} - m\gamma\dot{\mathbf{x}} = m\ddot{\mathbf{x}} \tag{1.9}$$

where e is the magnitude of the charge of the electron, m is its mass, x is the electron's position, and the dot represents derivative with respect to time. Assuming a time-harmonic incident field, the resulting position is also time-harmonic. This results in the expression for the position of the electron:

$$\mathbf{x} = \frac{e}{m(\omega^2 + i\gamma\omega)}\mathbf{E}\,. \tag{1.10}$$

Now, the polarization of a displaced electron is the electron charge times its displacement. Similarly, if there are many free electrons, the polarization is simply the sum of the individual polarizations: $\mathbf{P} = -ne\mathbf{x}$, where n is the number of electrons. Combining this with Eq. 1.10 and the constitutive relation Eq. 1.5, we arrive at the result:

$$\mathbf{D} = \epsilon_0(1 - \frac{\omega_p^2}{\omega^2 + i\gamma\omega})\mathbf{E}, \tag{1.11}$$

and therefore

$$\epsilon = 1 - \frac{\omega_p^2}{\omega^2 + i\gamma\omega}, \tag{1.12}$$

where the plasma frequency has been defined $\omega_p = \frac{ne^2}{\epsilon_0 m}$. Eq. 1.12 is the central result, describing how the permittivity of a metal varies with wavelength.

If the damping is small, then the permittivity $\epsilon \approx 1 - C\lambda^2$, where C is a constant which depends on the metal. Thus, the permittivity is near 1 for small wavelengths, and decreases to negative numbers with increasing wavelength.

How accurate are the results of the Drude model? Generally, its results match well to the optical properties of metals observed experimentally for gold and silver [13]. However, the Drude model fails to predict some important loss characteristics observed experimentally, which are due to absorption of electron energy levels (i.e. D-band electrons) at certain wavelengths. For numerical calculations in this dissertation, the experimental data is used; nevertheless, the Drude model provides useful insight into the origin of the observed optical properties of plasmonic metals.

1.3.2 Scattering by Spherical Particles

Mie theory solves Maxwell's equations for an electromagnetic wave incident on a spherical particle of arbitrary size. The details of the solution are quite lengthy and mathematically intensive, and so will not be provided in detail here. They can be found in classic electromagnetic texts [2, 14, 15]. While Mie solved this problem over 100 years ago, only in the past few decades has the theory been extended to take into account multiple spheres. The generalized multiparticle Mie (GMM) theory now allows an exact solution [16–20].

The solution to both the Mie and GMM theories are in the form of an infinite series (which converges after a finite number of terms). Therefore, while the solutions are exact, and are typically achieved with much less computation than numerical methods discussed below, the resulting mathematics does not provide much physical insight itself. A simplification to Mie theory, called the quasi-static approximation, sacrifices the exactness of the Mie solution for valuable insight, and is discussed in detail in the next section.

1.3.3 Quasi-static Approximation

The quasi-static approximation gives the solution of Maxwell's equations for an electromagnetic wave incident on a particle which is small compared to the wavelength of the incident wave. In other words, the retardation of the wave over the particle is not considered. The key results of the quasi-static approximation are the expressions for the polarizability of the particle, and for the electromagnetic fields at all positions outside of the particle:

$$\alpha = 4\pi a^3 \frac{\epsilon - \epsilon_m}{\epsilon + 2\epsilon_m} \tag{1.13}$$

$$\mathbf{E} = \mathbf{E}_i + \frac{1}{4\pi\epsilon_0\epsilon_m}\{k^2(\mathbf{n}\times\mathbf{p})\times\mathbf{n}\frac{e^{ikr}}{r} + [3\mathbf{n}(\mathbf{n}\cdot\mathbf{p}) - \mathbf{p}](\frac{1}{r^3} - \frac{ik}{r^2})e^{ikr}\} \tag{1.14}$$

$$\mathbf{H} = \mathbf{H}_i + \frac{ck^2}{4\pi}(\mathbf{n}\times\mathbf{p})\frac{e^{ikr}}{r}(1 - \frac{1}{ikr})\,, \tag{1.15}$$

where $\mathbf{p} = \epsilon_0\epsilon_m\alpha\mathbf{E}_i$, $\mathbf{H}_i$ and $\mathbf{E}_i$ are the incident waves, $k = 2\pi/\lambda$ is the free-space wavenumber, a is the particle radius, $\mathbf{n}$ is the unit vector to the point of interest.

The concept of localized surface plasmon resonance (LSPR) can be readily seen via Eq. 1.13: if loss is small ($\mathrm{Im}(\epsilon) \approx 0$), then the polarizability will blow up at the condition $\epsilon = -2\epsilon_m$. This is called the Frölich condition. Given the permittivity of a particular material as a function of wavelength (e.g. using the Drude model, or the experimental data), this condition can be solved for a particular wavelength.

1.3.4 Measures of Plasmon Resonance

The expressions for the electromagnetic field outside the particle (Eqs. 1.14-1.15) are related to several important measures. In the far field, the scattering and extinction cross sections are commonly used. These measures indicate the flux of electromagnetic energy far from the particle, and are defined by:

$$C_s = \frac{1}{I_i}\int_A \mathbf{S}_s \cdot \hat{\mathbf{e}}_r dA \tag{1.16}$$

$$C_{ext} = \frac{1}{I_i}\int_A \mathbf{S}_{ext} \cdot \hat{\mathbf{e}}_r dA \tag{1.17}$$

$$C_{abs} = C_{ext} - C_s \tag{1.18}$$

where I_i is the incident irradiance, and the time-averaged Poynting vectors are given by

$$\mathbf{S}_s = \frac{1}{2}\mathrm{Re}(\mathbf{E}_s \times \mathbf{H}_s^*) \tag{1.19}$$

$$\mathbf{S}_{ext} = \frac{1}{2}\mathrm{Re}(\mathbf{E}_i \times \mathbf{H}_s^* + \mathbf{E}_s \times \mathbf{H}_i^*)\,, \tag{1.20}$$

where the subscripts s, i represent the scattered and incident fields, respectively, the superscript $*$ represents the complex conjugate.

Eqs. 1.16 are general to an arbitrary particle. By carrying out these integrals using the field expressions from the quasi-static approximation (Eqs. 1.14 and 1.15), one arrives at the far field expressions for the quasi-static approximation:

$$C_{sca} = \frac{k^4}{6\pi}|\alpha|^2 \tag{1.21}$$

$$C_{abs} = k\mathrm{Im}(\alpha) \tag{1.22}$$

$$C_{ext} = C_{sca} + C_{abs}\,. \tag{1.23}$$

For the near field, which is typically shown in computations, the electric field amplitude $|\mathbf{E}|$ is a common measure. Since the surface-enhancement mechanisms such as surface-enhanced Raman spectroscopy (SERS) are believed to depend to approximately to the fourth power of the electric field amplitude, this is a useful measure to predict the molecular sensitivity of a nanoplasmonic structure. Where (spatially) should this electric field be measured? There are several choices, that in general may not give the same results. We define the two measures, the surface maximum $|\mathbf{E}|_{max}$, and the surface average $|\mathbf{E}|_{SA}$ local field amplitudes:

$$|\mathbf{E}|_{max} = \mathrm{Max}(|\mathbf{E}|)\,, r = a \tag{1.24}$$

$$|\mathbf{E}|_{SA} = \frac{\int_S |\mathbf{E}| dS}{\int_S dS}\,, \tag{1.25}$$

The concept of resonance becomes more difficult if we consider the observable measures of plasmon resonance. An in depth discussion of this issue is deferred to Chapter 2.

1.3.5 Plasmonic Based Forces

Once the electromagnetic field surrounding a particle (e.g. a dielectric particle, cell, or nanoparticle) is known, the force on that particle can be computed via the Maxwell stress dyadic, defined by

$$\underline{\underline{T}}(z) = \frac{1}{2}\,\mathrm{Re}[\underline{D}^*(z)\underline{E}(z) + \underline{B}^*(z)\underline{H}(z) - \frac{1}{2}(\underline{D}^*(z)\cdot\underline{E}(z) + \underline{B}^*(z)\cdot\underline{H}(z))\underline{\underline{I}}]\,, \quad (1.26)$$

where $\underline{\underline{I}}$ is the identity dyadic. The time–averaged force over any surface S can then be determined as

$$\underline{F} = \int_S \underline{\underline{T}}\cdot\hat{n}\,dS\,, \quad (1.27)$$

where $\hat{n}$ is the outward facing unit normal to that surface.

1.4 Detection Schemes

An increasing arrays of cellular and molecular detection techniques based on nanoplasmonics are actively being developed. These include surface enhanced Raman spectroscopy (SERS), surface-enhanced fluorescence (SEF), and plasmon resonance energy transfer (PRET). In addition, traditional scattering and absorption techniques can be used. There are large bodies of literature on each of these detection techniques; here, we will restrict ourselves to a basic introduction to each technique.

1.4.1 SERS

Raman spectroscopy utilizes the transfer of energy between an incident electromagnetic wave and the vibrational resonance of a molecule. Because the vibrations of a molecule are particular to the shape and composition of the molecule, the Raman spectrum can provide a molecular "fingerprint." While the Raman energy transfer occurs naturally, it is a fairly rare event: typically far less than 1 photon in 1000 exhibits this interaction. However the Raman signal can be greatly enhanced when the molecule of interest is located very close to a plasmonic structure, which can locally enhance the incident electric field. This phenomenon is called surface-enhanced Raman spectroscopy (SERS).

SERS was first discovered in 1974, when Fleischman and coworkers reported a strong Raman scattering signal from pyridine adsorbed onto electrochemically roughened silver [21], and this finding generated large interest in engineering metal surfaces with nanoscale roughness in hopes of increasing the local electromagnetic field enhancement [22–28]. Many biophysical SERS experiments performed on amino acids, purine and pyrimidine bases, proteins, DNA, and RNA have been reported on roughened surfaces [29], which typically consist of large areas of continuous films or sheets. It was later discovered that noble metal nanoparticles and their aggregates can also exhibit SERS, and their nano-scale dimensions give them potential for cellular SERS detection [6].

While random nanoparticle aggregation produces regions of high electromagnetic field enhancement (hot-spots), these regions are unpredictable and nonuniform, which limits the quantification of molecules of interest [30–32]. Therefore, recent work has focused on strategies to create nanoplasmonic architectures which can give a reproducible SERS signal.

1.4.2 SEF

Surface-enhanced fluorescence is the near field coupling between a fluorescent molecule and the high local electromagnetic field surrounding a plasmonic surface. The resulting fluorescence can be enhanced several orders of magnitude [33]. Controlling the distance between the fluorescent molecule of interest and the surface is critical–for relatively large distances (e.g. >100nm) the effect is small, and for molecules located on or within nanometers to the surface, fluorescent quenching is likely to occur. While SEF has received less attention than SERS, its interest has been growing for biological application, in part due to the familiarity and widespread use of fluorescence.

1.4.3 PRET

Plasmon resonance energy transfer is analogous to traditional absorption spectroscopy, except that the absorption occurs in the region immediately surrounding a nanoplasmonic structure. In this case the absorption peak of the molecule of interest is subtracted from the scattering spectrum of the nanoparticle. The resulting spectrum is the scattering spectrum with dips at the signature absorption peaks of the biomolecule. This requires the scattering spectrum of the nanoparticle and the absorption spectrum of the molecule to overlap. PRET is an emerging technique pioneered by the Lee lab and others [34].

1.4.4 LSPR-shift

Detection using localized surface plasmon resonance shift (LSPR-shift) takes advantage of the sensitivity of nanoplasmonic structures to optical properties of the closely surrounding environment (within tens of nm) [35, 36]. In the simplest case, the adsorption of a molecule of interest on the surface of the nanoparticle causes a change in the effective permittivity surrounding the particle, and shifts the resonance peak of the scattering or absorption spectrum. The peak shift is typically measured with a spectrometer, however larger shifts may be detected directly with the human eye. Extensions of this technique, for example using core-satellite architectures (discussed later), may allow an LSPR-shift readily detectable by the eye.

Optical Viscosity

As noted in section 1.2, LSPR-shift sensing can also be thought of as measuring the optical viscosity of a local region. Just as local fluid viscosity can give information about the composition and state of a cell, the optical viscosity can reveal useful information about the optical characteristics of a region.

1.4.5 Comparison with Other Sensors

Scattering and Absorption Cross-Section

The distinction of the optical properties of nanoplasmonic particles in comparison to other optical probes can be largely understood in terms of scattering and absorption cross-sections. The scattering and absorption cross sections describe the likelihood that an incident photon will be scattered or absorbed, respectively, by a particle. For example, a single silver nanosphere 80 nm in diameter reaches a scattering cross-section of $3 \times 10^{-2} \mu\text{m}^2$, which is a million times greater than the fluorescence of a fluorescein molecule. Even if a nanosphere the same size were packed with fluorescein to the self-quenching limit, the scattering section of the silver nanoparticle is still a thousand times greater [37]. Nanospheres of dielectric composition (e.g. silica or polystyrene spheres), exhibit only a fraction of the scattering cross-section in the optical regime, and have minimal absorption [38]. In addition, it is important to note that dielectric particles do not exhibit the plasmon peaks, and cannot be readily tuned by choice of geometry.

Directionality Control

Apart from fully symmetric structures such as spheres, most nanoplasmonic systems possess an asymmetry that can be utilized. For example, the asymmetry of nanorods, nanocrescents, and crescent-shaped nanoholes causes light interactions that are highly

dependent on the polarization of the incident light. In these cases, different plasmon modes (and different peak wavelengths) can be excited depending on the incident polarization. The detailed dependence on polarization of nanocrescents and crescent-shaped nanoholes will be discussed later.

1.5 Cellular and Molecular Manipulation

While not directly our focus, nanoplasmonics can also be used to manipulate cells and molecules, primarily using two mechanisms: optical forces and local heating. As described in Section 1.3.5, optical forces are generated when light is incident on a nanostructure. This can be used either to manipulate the nanostructure directly, or to manipulate other structures in close proximity (e.g. molecules, beads, or cells). In this regard, nanoplasmonics allows an extension of traditional optical tweezers [39]. Local heating of nanoplasmonic structures occurs when incident light is absorbed, an effect which is drastically increased near the plasmon resonance of a structure. Therefore, nanoplasmonic structures can serve as local heat sources, capable of optical release of molecules [40], as well as photothermal killing of cells [10]. Unlike traditional heat sources, nanoplasmonics allows heat to be carefully controlled temporally and spatially. While we will not study heat generation explicitly, our focus on absorption is directly related to heat generation in a nanoplasmonic structure.

Chapter 2

Differences Between Near and Far Field Measures of Nanoplasmonic Resonance

"What is life but the angle of vision? A man is measured by the angle at which he looks at objects."

Ralph Waldo Emerson

2.1 Introduction

When a new nanoplasmonic structure is proposed, or when structures are to be compared, a deceivingly simple question arises: how should the plasmonic characteristics of the nanostructure(s) be characterized? Two classes of measures are currently in common use: far-field quantities of scattering, extinction, and absorption cross sections, and the near-field quantities of electric field amplitude, intensity, and their maximum and surface-average values. The far-field measures remain the most commonly used, at least in part because they are easier to obtain experimentally. However, it is the localized field enhancement that is responsible for surface-enhanced spectroscopic processes (e.g. SERS [36]) discussed in Chapter 1; hence, local field measures are those most intimately tied with the sensing capabilities of a structure.

The use of such a variety of measures presents several problems. Firstly, it makes comparing the effectiveness of different structures difficult, which is a significant difficulty given the dozens of different geometries that have been proposed, with many more likely to emerge in the coming years. Secondly, it is unclear which (if any) of the measures are interchangeable: if the spectrum (plasmon band) is considered, should the peak magnitude, width, or position be the same for any of these measures? Finally, if there is a difference between the different measures, then how are they related?

Such questions are relevant both for improving fundamental understanding of spectroscopic processes, and for practical applications. For example, consider the common case of a researcher hoping to match a nanoplasmonic device with an incident laser wavelength to maximize a local surface-enhanced effect such as SERS. He/she takes a scattering spectrum of the structure, and matches the laser wavelength to its peak (or alternatively, tunes the nanostructure geometry until the scattering spectrum matches a given incident laser). If the near-field resonance is matched to the scattering spectrum, then this method is valid; however, if the near-field spectrum is blue or redshifted vs the scattering spectrum, then this difference may cause poor excitation of the local field. This is conceptually illustrated in Fig. 2.1.

While it has been known for decades that differences occur between near- and far- field measures of spherical metallic particles [41], the subject has received little attention recently, and no systematic study of the relationship between measures has been carried out. In this chapter we tackle this problem from 3 different angles. First, by using the quasi-static approximation and its extensions, we establish a conceptual understanding of the conditions in which differences among the measures of plasmon resonance occur. We then use a combination of the exact analytical solution (for spheres) and the finite element method (for nonspherical geometries) to provide rigorous solutions. We show that significant differences can indeed arise for physically relevant systems of both gold and silver particles. We expect that taking into

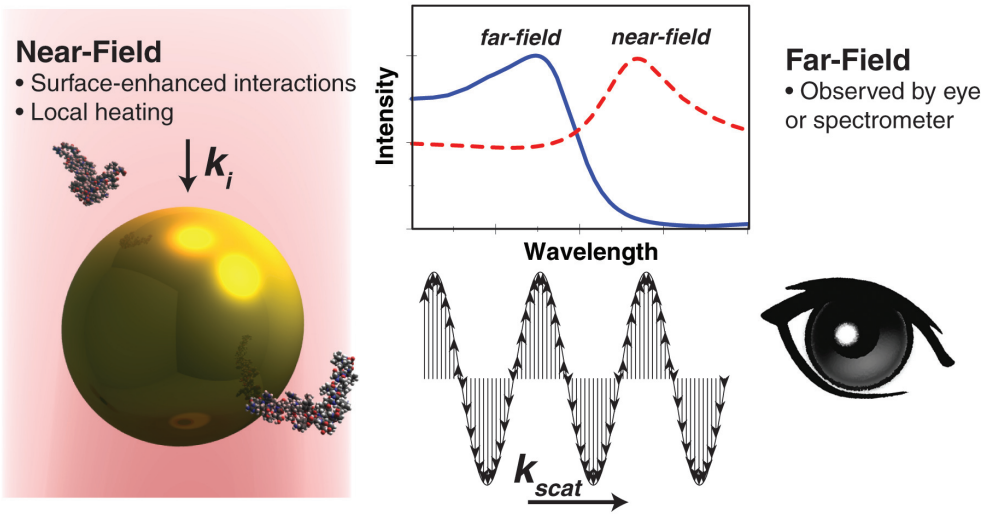

Figure 2.1: Schematic of the potential differences between the near- and far- field measures of plasmon resonance. The near-field resonances may occur at significantly different wavelengths than the observed far-field resonances.

account these differences can provide improvement in understanding and optimizing surface-enhanced spectroscopies.

2.2 Differences in the Quasi-Static Approximation

Considering the quasi-static approximation, differences between near- and far-field resonances around a particle might be expected: the near-field is dominated by a $1/r^3$ term, while in the far-field a $1/r$ term dominates (see Equation 1.14). Physically, the near-field measures indicate the ability of the particle to convert incoming light into a local field, while the far-field measures indicate the ability of the particle to absorb light and/or convert it into a propagating wave. Thus, one should not, in general, expect a single wavelength to optimize both conditions. This is visualized in Figure 2.2 with the exact Mie theory solution: for a plane wave of wavelength 700 nm incident on a gold particle (radius 100 nm), the local field is maximized, while at 600 nm a more distinct propagating scattered field emerges.

Let us consider the quasi-static approximation in more detail. Consider a particle with polarizability α and radius a present in an isotropic lossless medium. Assuming an incident plane wave (with $|\mathbf{E}_i| = 1$), the total electric field surrounding the particle is then given by equation 1.14, reproduced here:

$$\mathbf{E} = \mathbf{E}_i + \frac{1}{4\pi\epsilon_0\epsilon_m}\{k^2(\mathbf{n}\times\mathbf{p})\times\mathbf{n}\frac{e^{ikr}}{r} + [3\mathbf{n}(\mathbf{n}\cdot\mathbf{p}) - \mathbf{p}](\frac{1}{r^3} - \frac{ik}{r^2})e^{ikr}, \tag{2.1}$$

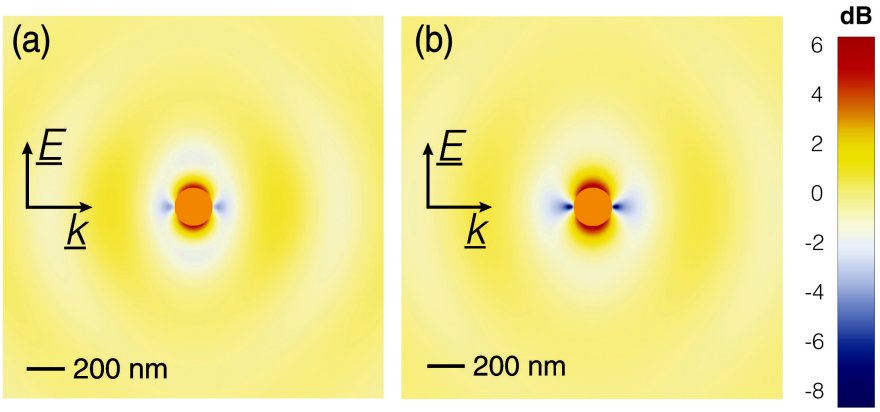

Figure 2.2: The electric field amplitude surrounding a gold nanoparticle with an incident plane wave with free-space wavelength (a) 600 nm and (b) 700 nm, computed with Mie theory.

where ϵ_0 is the permittivity of free space, ϵ_m is the relative permittivity of the surrounding medium, $k = 2\pi/\lambda$ is the wavenumber, n is the unit vector in the direction of $\mathbf{r}$, $r = |\mathbf{r}|$, and the dipole moment

$$\mathbf{p} = \epsilon_0 \epsilon_m \alpha \mathbf{E}_i \,. \tag{2.2}$$

The electric field is maximized at positions where the unit normal $\mathbf{n}$ and the dipole moment $\mathbf{p}$ are parallel. By setting $r = a$ and $\mathbf{n}$ parallel to $\mathbf{p}$ we compute:

$$\frac{|\mathbf{E}|^2_{\max}}{|\mathbf{E}_i|^2} = 1 + \frac{1 + a^2k^2}{4a^6\pi^2}|\alpha|^2 + \frac{1}{a^3\pi}\{[ak\,\mathrm{Im}(\alpha) + \mathrm{Re}(\alpha)]\cos(ak) + [-\mathrm{Im}(\alpha) + ak\,\mathrm{Re}(\alpha)]\sin(ak)\}. \tag{2.3}$$

The quasi-static approximation relies on the assumption $a << \lambda$. Hence, we can invoke $ak = a2\pi/\lambda \approx 0$. Therefore, equation 2.3 can be approximated as

$$\frac{|\mathbf{E}|^2_{\max}}{|\mathbf{E}_i|^2} \approx 1 + \frac{1}{4a^6\pi^2}|\alpha|^2 + \frac{1}{a^3\pi}\mathrm{Re}(\alpha). \tag{2.4}$$

To arrive at the surface-average electric field intensity at the surface of the nanoparticle, the expression $|\mathbf{E}|^2$ must be integrated over the surface and normalized to the surface area of the particle:

$$|\mathbf{E}|^2_{\mathrm{SA}} = \frac{1}{SA}\int_S |\mathbf{E}|^2 dA \,, \tag{2.5}$$

where S is the surface of the nanoparticle and SA is the surface area of the nanoparticle. Using equations 2.1 and 2.10, we arrive at:

$$\frac{|\mathbf{E}|^2_{\mathrm{SA}}}{|\mathbf{E}_i|^2} = 1 + \frac{3 + a^2k^2 + a^4k^4}{24a^6\pi^2}|\alpha|^2 + \frac{k^2}{3a\pi}[\mathrm{Re}(\alpha)\cos(ak) - \mathrm{Im}(\alpha)\sin(ak)] \,. \tag{2.6}$$

Again, applying $ak \approx 0$, this is simplified to:

$$\frac{|\mathbf{E}|^2_{\mathrm{SA}}}{|\mathbf{E}_i|^2} \approx 1 + \frac{1}{8a^6\pi^2}|\alpha|^2 + \frac{k^2}{3a\pi}\mathrm{Re}(\alpha)\,. \tag{2.7}$$

Note that because the polarizability is proportional to the volume of the particle, both the second and third terms of equations 2.4 and 2.7 are of comparable magnitude.

Combining these results with the well-known far field expressions, we have:

$$C_{abs} = k\,\mathrm{Im}(\alpha) \tag{2.8}$$

$$C_{sca} = \frac{k^4}{6\pi}(\mathrm{Re}(\alpha)^2 + \mathrm{Im}(\alpha)^2) \tag{2.9}$$

$$|\mathbf{E}|^2_{\mathrm{SA}} \approx 1 + \frac{1}{8a^6\pi^2}[\mathrm{Re}(\alpha)^2 + \mathrm{Im}(\alpha)^2] + \frac{k^2}{3a\pi}\mathrm{Re}(\alpha) \tag{2.10}$$

$$|\mathbf{E}|^2_{\mathrm{max}} \approx 1 + \frac{1}{4a^6\pi^2}[\mathrm{Re}(\alpha)^2 + \mathrm{Im}(\alpha)^2] + \frac{1}{a^3\pi}\mathrm{Re}(\alpha)\,, \tag{2.11}$$

Equations (2.8) and (2.9) are the absorption and scattering cross sections, respectively, while (2.10) and (2.11) represent the surface-average and maximum value of the square of the electric field amplitude at the surface of the nanoparticle.

The real and imaginary components of the polarizability $\mathrm{Re}(\alpha)$ and $\mathrm{Im}(\alpha)$ are shown explicitly in (2.8-2.11). Written this way, it becomes clear that the different measures of plasmon resonance depend differently on the polarizability. Namely, absorption (2.8) depends only on $\mathrm{Im}(\alpha)$, scattering (2.9) depends equally on $\mathrm{Re}(\alpha)$ and $\mathrm{Im}(\alpha)$, and the third terms in (2.10-2.11) demonstrate that the near-field is more dependent on $\mathrm{Re}(\alpha)$ than $\mathrm{Im}(\alpha)$. *Therefore, the differences among the measures of plasmon resonance are proportional to the differences between the real and imaginary parts of the polarizability.* For example, consider a case where $\mathrm{Re}(\alpha)$ is maximized at a wavelength $\lambda = 700\,\mathrm{nm}$ while $\mathrm{Im}(\alpha)$ is maximized at $\lambda = 600$. This would cause absorption (which depends on $\mathrm{Im}(\alpha)$) to be maximized near 600 nm, while the near-field (which depends primarily on $\mathrm{Re}(\alpha)$) would be maximized toward $\lambda = 700\,\mathrm{nm}$, while scattering would be maximized somewhere in between.

The key question now remains: at what conditions are the real and imaginary parts of the polarizability different? To answer this question, we first consider a general form of the polarizability

$$\alpha = \frac{V}{S + \frac{\epsilon_m}{\epsilon - \epsilon_m} - iL}\,, \tag{2.12}$$

where we have defined S to be a generalized geometrical factor term, and L to be a generalized damping loss term. This general model is useful because it can describe a variety of particle shapes and conditions. For example, for a small sphere, $S = 1/3$

and $L \approx 0$, while for an 4:1 aspect ratio spheroidal particle [42] $S \approx 0.07$ and $L \approx 0.02$ (specifically, long axis = 80 nm, $\epsilon_m = 1$, $\lambda = 700$ nm). While the parameters S and L may depend on factors including the particle volume and wavelength, we consider them here to be arbitrary parameters for generality, and later consider the possibility of engineering materials and geometries to achieve desired values of S and L.

Given the general polarizability of (2.12), we next compute at what conditions the real and imaginary parts are maximized. This is accomplished by 1) separating (2.12) into its real and imaginary parts and 2) finding the maximum of each part by solving $\partial[\mathrm{Re}(\alpha)]/\partial[\mathrm{Re}(\epsilon)] = 0$ and $\partial[\mathrm{Im}(\alpha)]/\partial[\mathrm{Re}(\epsilon)] = 0$, respectively. This results in expressions for $\mathrm{Re}(\epsilon)$ as a function of the permittivity of the surrounding medium and $\mathrm{Im}(\epsilon)$. Given the properties ϵ for a given material, the wavelengths which satisfy (2.13) and (2.14) can be computed, respectively. Hence, we arrive at our central result:

$$\mathrm{Max}[\mathrm{Re}(\alpha)] : \mathrm{Re}(\epsilon) = \frac{S-L-1}{S-L}\epsilon_m + \frac{L+S}{L-S}\mathrm{Im}(\epsilon)\,, \tag{2.13}$$

$$\mathrm{Max}[\mathrm{Im}(\alpha)] : \mathrm{Re}(\epsilon) = \frac{S-1}{S}\epsilon_m + \frac{L}{S}\mathrm{Im}(\epsilon)\,. \tag{2.14}$$

These equations represent the conditions in which the real and imaginary parts of the polarizability are maximized, and hence are the generalized Frölich conditions. The difference between the optimal conditions for the real and imaginary parts of the polarizability, indicated by (2.13 - 2.14), indicate the differences between the measures of LSPR.

To understand the implications of (2.13 - 2.14), we begin with the simplest case and proceed gradually to the most general case. For a small sphere in the quasi-static limit, $L \approx 0$ and $S = 1/3$. In this ideal regime, (2.13) and (2.14) reduce to:

$$\mathrm{Max}[\mathrm{Re}(\alpha)] : \mathrm{Re}(\epsilon) = -2\epsilon_m - \mathrm{Im}(\epsilon)\,, \tag{2.15}$$

$$\mathrm{Max}[\mathrm{Im}(\alpha)] : \mathrm{Re}(\epsilon) = -2\epsilon_m\,. \tag{2.16}$$

For an ideal lossless material ($\mathrm{Im}(\epsilon) = 0$), these equations further reduce to the well known Frölich condition $\mathrm{Re}(\epsilon) = -2\epsilon_m$. We emphasize that it is only for this ideal case that both $\mathrm{Re}(\alpha)$ and $\mathrm{Im}(\alpha)$ are maximized at the same condition. Hence only in this ideal case are the various measures of plasmon resonance optimized at a single condition.

For any real metal with a nonzero loss, $\mathrm{Re}(\alpha)$ is optimized for $\mathrm{Re}(\epsilon) < -2\epsilon_m$. These results are shown in Fig. 2.3(a-b), where we show the real and imaginary polarizability (normalized to the particle volume) as a function of the particle permittivity (normalized to the permittivity of the surrounding medium). The peak of $\mathrm{Im}(\alpha)$ remains fixed at $-2\epsilon_m$ (i.e. the Frölich condition), while the peak of $\mathrm{Re}(\alpha)$ becomes increasingly more negative as the material loss increases. For any plasmonic

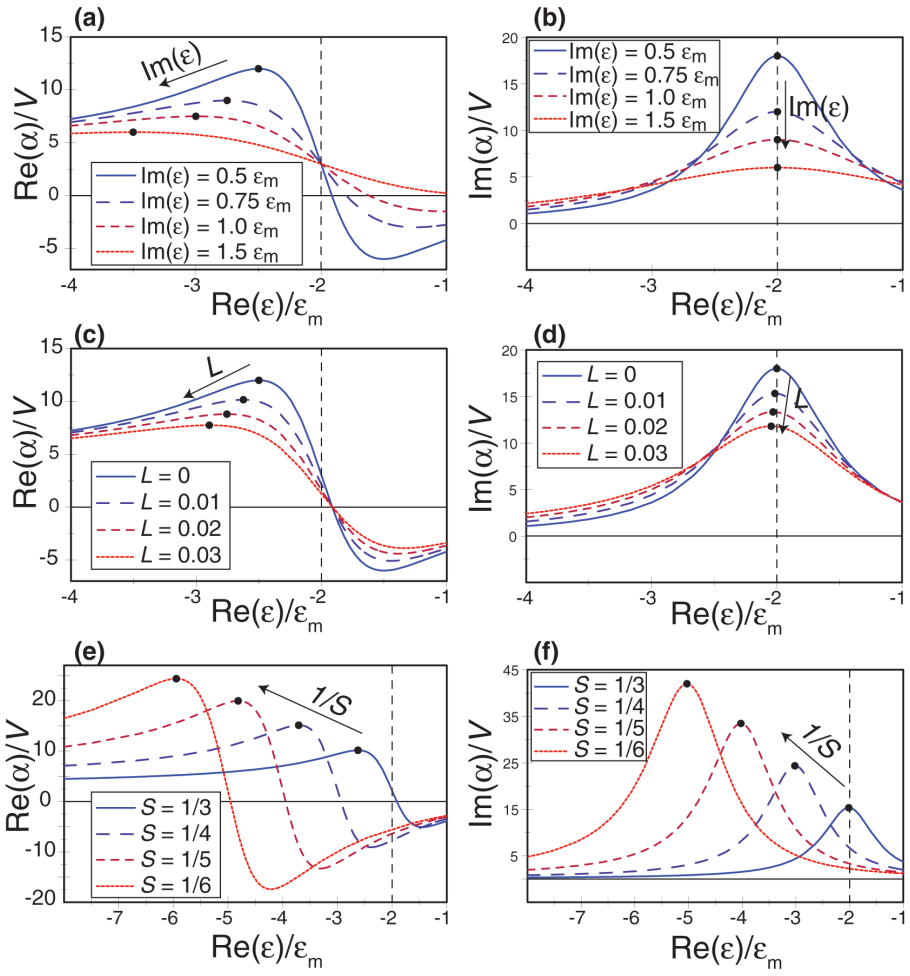

Figure 2.3: The dependence of the real and imaginary polarizability on (a-b) material loss, (c-d) damping loss, and (e-f) particle shape factor. The difference between the optimal conditions for the real and imaginary polarizability corresponds to the differences among the measures of plasmon resonance, as shown in equations (2.8-2.11). The dot indicating the maximum condition for each curve is determined by equations (2.13) and (2.14).

metal, the negative slope of $\mathrm{Re}[\epsilon(\lambda)]$ indicates that this condition will be satisfied for a longer wavelength than in the Frölich condition.

As discussed above with (2.8-2.11), near-field depends more strongly on the real part of the polarizability, while absorption depends entirely on the imaginary part of the polarizability; hence, for any small plasmonic sphere, the optimal wavelengths for

each measure satisfy

$$\lambda_{max,\,near} \geq \lambda_{max,\,scattering} \geq \lambda_{max,\,absorption}\,, \tag{2.17}$$

with the differences increasing with the material loss. In addition, since the differences among the measures are expected to increase with material loss (from (2.15)), we can predict that the differences are greater for a small gold sphere versus a small silver sphere, since gold is lossier. We also note that the material loss causes a broadening of the polarizability peak, and hence broadens the plasmon peak of each measure.

For a larger a sphere, damping loss factors such as radiation damping (due to the direct radiative decay of electrons [11, ch. 5]) occur due to the geometry. We take this into account with the general loss factor L in the polarizability (2.12). In this case, $S = 1/3$ and $L > 0$, and equations (2.13) and (2.14) simplify to:

$$\mathrm{Max}[\mathrm{Re}(\alpha)] : \mathrm{Re}(\epsilon) = \frac{2+3L}{-1+3L}\epsilon_m + \frac{1+3L}{-1+3L}\mathrm{Im}(\epsilon)\,, \tag{2.18}$$

$$\mathrm{Max}[\mathrm{Im}(\alpha)] : \mathrm{Re}(\epsilon) = -2\epsilon_m - 3L\mathrm{Im}(\epsilon) \tag{2.19}$$

The influence of L, shown in Fig. 2.3(c-d), causes both $\mathrm{Re}(\alpha)$ and $\mathrm{Im}(\alpha)$ to be satisfied for $\mathrm{Re}(\epsilon) < -2\epsilon_m$; however the reduction is more significant for $\mathrm{Re}(\alpha)$ than $\mathrm{Im}(\alpha)$. Therefore, damping is expected to cause a redshift for all measures of plasmon resonance, but the redshift is much more significant for the measures which depend on the real part of the polarizability. Hence again (2.17) is satisfied, with the differences among the measures increasing with the damping loss L.

Finally, nonspherical particles can be described by changing the shape factor S in the general polarizability (2.12). In this general case described by (2.13) and (2.14) we have $S \neq 1/3$ and $L > 0$. As the shape factor is decreased, a pronounced redshift occurs for both the real and imaginary permittivities, as shown in Fig. 2.3(e-f). Unlike the redshift induced by the material loss or damping, the shift due to the shape factor retains the sharpness of the polarizability peak.

To conclude, in this section we have presented a theoretical framework based on the quasi-static approximation, in which differences among the measures of plasmon resonance can be well understood. We have shown the general relation $\lambda_{max,\,near} \geq \lambda_{max,\,scattering} \geq \lambda_{max,\,absorption}$, while the difference among the measures depend on both material loss and damping. Specifically, differences among the measures for small structures are due primarily to material loss, differences increase with particle volume due to damping effects. Changing the particle shape (via the shape factor L) can shift the peak of all measures without causing a divergence between them.

Let us summarize the predictions of our model as they relate to the structures investigated rigorously in the following section: (i) differences among the measures for small structures are due primarily to material loss; (ii) differences among the

measures should increase with particle volume due to damping effects; (iii) rodlike shapes (which decrease the shape factor) should cause a redshift of all measures equally.

2.3 Rigorous Solutions

In the previous section, we have developed a model to understand differences between resonances in the near- and far-field. However the quasi-static approximation, on which this model is based, is strictly valid for particles of diameter much smaller than the incident wavelength. In addition, particles of arbitrary shape can only be understood with a generalized shape factor. Therefore, to test the validity of the quasi-static model developed in the previous section, we utilize the exact analytic solution (Mie theory) to consider spheres of arbitrary size, and use the finite element method to consider nonspherical shapes.

2.3.1 Spherical Particles of Arbitrary Size

We consider spherical gold and silver particles each with complex permittivity ϵ given by an analytical model [43] of the experimental data [13] for bulk gold and silver. The particle is present in free space ($\epsilon_m = 1$), and the permeability of both the particle and surrounding medium are assumed to be $\mu = 1$. Mie theory[2, 14, 15] is used to compute the exact solution, and series terms were added until the results converged. The quasi-static model presented above, which can be thought of as an approximation to Mie theory, valid when the particle size is much smaller than the wavelength of the incident light [15], is used in providing physical understanding.

In Figure 2.4 we compare the spectra of the normalized values of the absorption, extinction, and scattering cross sections, as well as the near-field measures of maximum and surface-average intensity, for a gold sphere (radius = 25 nm). There is a notable difference between the measures, even for this relatively small particle size.

As the particle size is increased, the differences between the measures becomes more pronounced. In Figure 2.5, we show the peak wavelength and bandwidth for each measure for both gold and silver spherical particles as a function of particle size. For silver particles, all five measures converge for small particle size, and begin to diverge as the particle radius exceeds 40 nm. For gold, on the other hand, there is a distinct difference between the measures even for small particle size, and the difference increases as the particle size is increased. As the particle radius nears 100 nm for both silver and gold, the peak wavelengths for the different measures spans 200 nm for gold and 300 nm for silver. Such a range is certainly significant for current spectroscopic techniques.

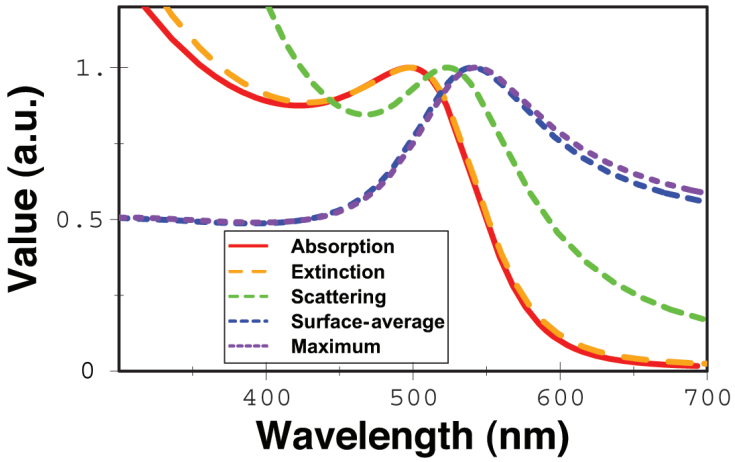

Figure 2.4: A comparison of the normalized values of absorption, extinction, and scattering cross sections, and the surface–average and maximum electric field intensity at the surface of a gold sphere (radius = 25 nm) as a function of wavelength, computed via Mie theory.

As particle size increases beyond $a = 100\,\text{nm}$, the difference in peak wavelength for the measures continues to diverge; however, the plasmon band is significantly broadened in this regime. We demonstrate this effect in Figure 2.5, where we show 10% of the full width of the plasmon band at 90% of its maximum value. The value of 90% was chosen because for some conditions (e.g. for C_{abs}) the more common full-width at half-maximum (FWHM) is not well-defined, and only 10% of the value is chosen for clarity of the figure. It is clear that the plasmon bandwidth for all measures increases with particle size, with the near-field measures showing larger broadening (again due to their dependance on $\text{Re}(\alpha)$). Thus, while the difference in peak wavelength increases, the concept of peak wavelength ceases to have significant meaning for larger particles. We note that the differences in absorption peak broadening between gold and silver indicate that material properties play a large role, while the peak broadening for all other measures is largely defined by radiation damping.

The curves of Figure 2.5 can be fit by simple phenomenological expressions, which are presented in Tables 2.1 and 2.2. We model the near-field gold and silver curves with exponential and sigmoidal fits, respectively, while the scattering and extinction curves are best modeled by power law fits. Absorption curves, which both and decrease with increasing particle size, were fit with piecewise curves.

The equations in Tables 2.1 and 2.2 essentially provide a means of converting between the 5 near- and far-field measures: given the optimal wavelength for a single measure, one can quickly estimate the expected optimal wavelength for the remaining four measures. While the fits shown are simple, they provide excellent agreement

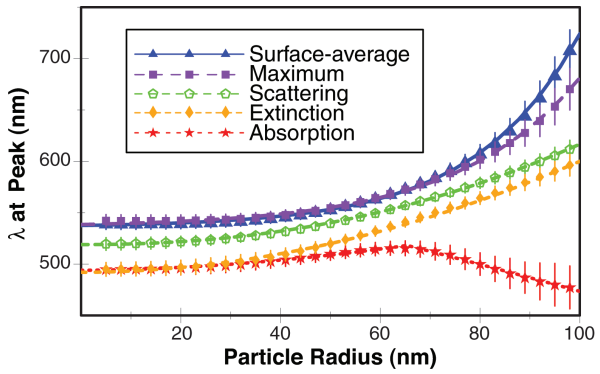

(a)

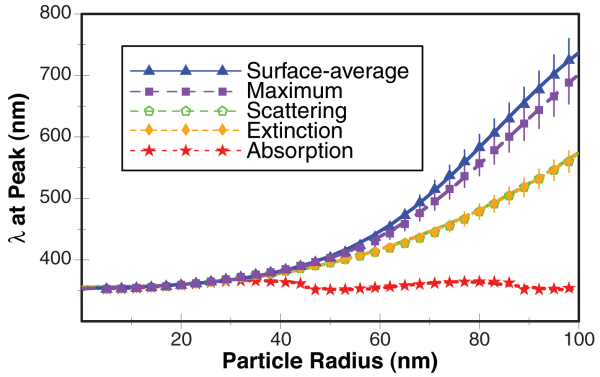

(b)

Figure 2.5: The peak wavelength for the primary resonance for the measures in Figure 2.4 as a function of particle radius for (a) gold and (b) silver. Symbols represent exact data (Mie theory), while solid and dashed lines represent curve fits presented in Tables 2.1 and 2.2. The vertical bars represent 10% of the full–width of the plasmon band at 90% maximum.

Table 2.1: Fits (shown in Figure 2.5a) for peak wavelength as a function of particle radius a for gold (a and λ in nm).

Measure	Curve Fit Equation
Absorption	$\lambda_{abs} = 494 + 0.0120\,a^{1.82}$, $a \leq 65$
	$\lambda_{abs} = 586 - 0.469\,a^{1.19}$, $a > 65$
Scattering	$\lambda_{sca} = 519 + 0.00389\,a^{2.20}$
Extinction	$\lambda_{ext} = 492 + 0.0136\,a^{1.95}$
Surface–average intensity	$\lambda_{SA} = 536 + 1.58\,\mathrm{Exp}[0.0478\,a]$
Maximum intensity	$\lambda_{max} = 536 + 2.53\,\mathrm{Exp}[0.0405\,a]$

Table 2.2: Fits (shown in Figure 2.5b) for peak wavelength as a function of particle radius a for silver (a and λ in nm).

Measure	Curve Fit Equation
Absorption	$\lambda_{abs} = 360 - 6.41\cos(0.117\,a - 0.791)\,,\ a \leq 45$
	$\lambda_{abs} = 358 - 6.33\cos(0.140\,a - 1.21)\ \ ,\ a > 45$
Scattering	$\lambda_{sca} = 356 + 0.00229\,a^{2.49}$
Extinction	$\lambda_{ext} = 356 + 0.00228\,a^{2.49}$
Surface–average intensity	$\lambda_{SA} = 351 + \frac{520}{1+\mathrm{Exp}[5.33-0.0639\,a]}$
Maximum intensity	$\lambda_{max} = 350 + \frac{518}{1+\mathrm{Exp}[5.10-0.0585\,a]}$

with Mie theory: for a particle size ranging from 5 nm to 100 nm, the maximum and mean error of each fit is < 4 nm and < 2 nm, respectively. Given that this variation is comparable to or less than the variation which occurs due to the differences in analytical fits of the complex permittivity of the metals [43, 44], further improvement in the fits is unnecessary at the present time.

The rigorous Mie theory results for spherical particles match well with the predictions of the quasi static theory developed in the previous section. The rule $\lambda_{max,\,near} \geq \lambda_{max,\,scattering} \geq \lambda_{max,\,absorption}$ is obeyed, and the lossier gold shows a greater difference among the measures than silver. For both materials, as the particle size increases (increased damping) the differences among the measures increases, also as predicted by the quasi-static theory.

2.3.2 Nonspherical Particles

While spherical particles have been widely used for many plasmonic applications, many nonspherical particles have been developed in recent years. Nonspherical particles offer significant advantages over spherical ones, such as wide plasmon tunability, increased local field enhancement, and increased heat generation [22]. Given that significant differences in the near- and far-fields can arise for spherical particles, as shown above, it is natural to ask, how does geometry affect these differences? Spheroidal particles are a natural starting point for this investigation, since the spheroid geometry can vary continuously from a sphere to a needle-like particle. Spheroids are important physically because they serve as a good approximation to nanorods, which are becoming widely used nanoplasmonic probes.

Nonspherical particles present a challenge theoretically, since analytic techniques for scattering by arbitrary particle shape are not known. However, computational techniques are now available that can solve for complex geometries. In this subsection, we use finite element analysis to study spheroidal particles, with the same material properties assumed as in our Mie calculations. Fig. 2.6a demonstrates the

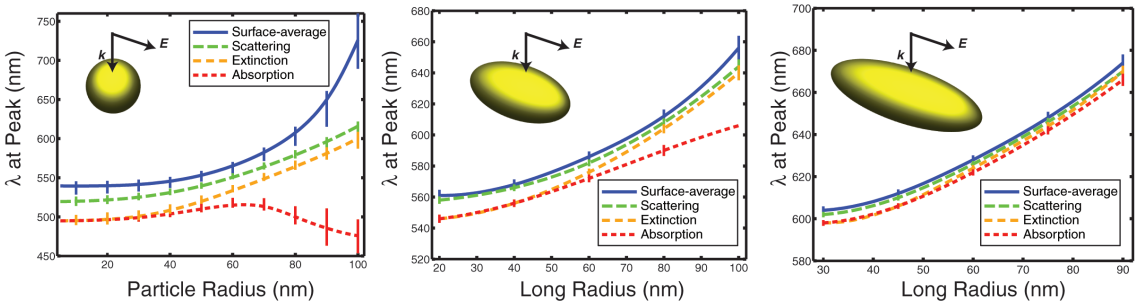

Figure 2.6: Peak wavelength as a function of particle size for gold spheroidal nanorods for an aspect ratio of (a) 1:1 (sphere), (b) 2:1 and (c) 3:1. The vertical bars represent 20% of the full-width of the plasmon band at 90% maximum. Results are computed with a finite element model, with the exact Mie solution superimposed in (a).

convergence of the finite element model to the exact theory. We note that due to the difficulty in reliably obtaining convergence of the maximum field, and because of its similarity with the surface-average field, we do not consider the maximum field in this subsection.

By varying the spheroid aspect ratio, the progression from sphere to nanorod is shown in Fig. 2.6. The electric field polarization is taken to be along the long axis of the nanorod. The size trend observed for spheres is also apparent for nanorods: namely, at any aspect ratio, as the size of the particle increases, the difference between the measures increases. As in the case of the sphere, the near-field is always redshifted compared to the far-field, with absorption the bluest measure. This trend is consistent with the analysis of the quasi-static and extended quasi-static approximation.

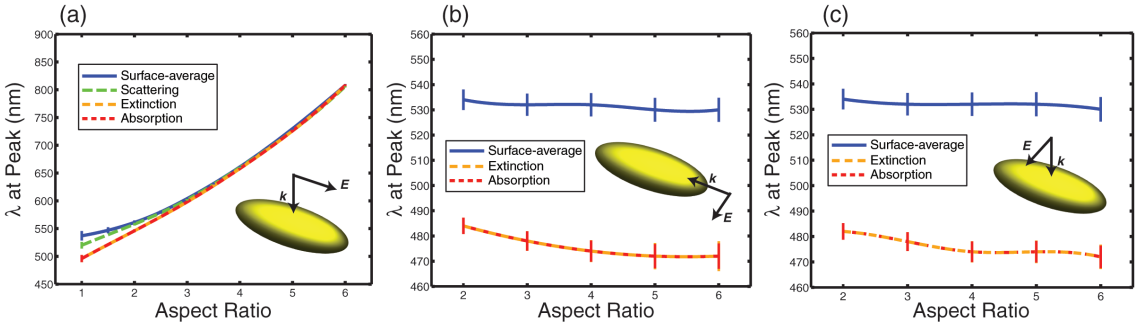

Figure 2.7: (a-c) Peak wavelength as a function of aspect ratio for spheroidal nanorods with polarizations as shown; the vertical bars represent 20% of the full-width of the plasmon band at 90% maximum.

In addition, as the aspect ratio increases, the measures converge: while for a sphere radius of 100 nm, there is over a 200 nm difference among the measures, for a

3:1 spheroid with the long axis radius of 100 nm, only a 10 nm difference is observed. This trend suggests only small difference among the measures will be observed for particles with sharp features.

Finally, we consider the effect of polarization, fixing the short axes of the nanorod at 10 nm and varying the aspect ratio in Fig. 2.7. For the electric field polarization parallel to the long axis of the nanorod, the measures converge for increasing aspect ratio. In contrast, for polarizations perpendicular to the long axis, the aspect ratio has little effect. This might be expected, since the cross-section of the particle in these cases remains unchanged. The approximately constant difference of 50 nm between the near- and far-fields is nearly identical to that observed for small spherical particles of the same cross-section.

Again, the rigorous computations match well with the predictions of the quasi static theory. The rule $\lambda_{max,\,near} \geq \lambda_{max,\,scattering} \geq \lambda_{max,\,absorption}$ remains obeyed, while the measures become close together as the particle aspect ratio increases. This was indeed predicted by the change in shape factor in Section 2.2.

2.4 Conclusion

In this chapter we have presented a systematic investigation of the differences in the measures of plasmon resonance for spherical and spheroidal nanoparticles. It has been conclusively demonstrated that there is no single wavelength that optimizes the measurable quantities indicative of plasmon resonance. We have shown the near-fields are consistently redshifted compared to the far-field measures, and the difference can reach over 200 nm for gold and silver nanoparticles. For spherical particles we have provided simple phenomenological fits which provide conversion between the 5 commonly used near- and far-field measures.

We have presented a theoretical framework based on the quasi-static approximation, in which differences among the measures of plasmon resonance can be well understood. We have shown the general relation $\lambda_{\mathrm{max,\,near}} \geq \lambda_{\mathrm{max,\,scattering}} \geq \lambda_{\mathrm{max,\,absorption}}$, while the difference among the measures depend on both material loss and damping. Specifically, differences among the measures for small structures are dependent upon the material loss, and differences increase with particle volume due to damping effects. Changing the particle shape (via the shape factor L) can shift the resonance of all measures without causing a significant divergence between them. We have verified these predictions theoretically and computationally using Mie theory and finite element analysis. These studies have also quantified the differences among the measures for relevant geometric parameters.

Apart from the fundamental importance in understanding plasmon resonance, taking these differences into account should improve spectroscopic signal for a wide range of applications of molecular detection, plasmonic heating, and optical release.

In turn, it may be possible to use these results to characterize key properties of a nanoplasmonic system: for example, by measuring the differences in peak wavelength between the absorption and scattering spectra, one may infer the significance of loss in the system.

Chapter 3

Active Polymer Nanofabrication

> "If you want to build a computer chip, you need a giant semiconductor fabrication facility. But nature can grow complex molecular machines using nothing more than a plant."
>
> Ralph Merkle

Thus far, we have emphasized the importance of design rules in creating useful nanoplasmonic sensors. In particular, sharp tips are required to utilize the lighting rod effect, and nanogaps between structures are needed to utilize the capacitor effect. In addition, as we will discuss in Chapter 7, achieving high densities of nanoplasmonic antenna is also critical.

In general, these requirements are very difficult to meet using current fabrication methods. Top down techniques such as focused ion beam (FIB) or electron beam lithographies can reach resolutions of ≈ 10 nm; however these are serial processes, which makes fabricating practical devices over large areas unfeasible. Nanoimprint lithography is a rapidly developing technology that can also reach features of this scale, but masks are extremely expensive, and become damaged with use. In contrast, bottom-up methods such as nanosphere lithography or copolymer-based lithography offer the potential to create inexpensive large area arrays with sub-100 nm features, but can only be used to generate a limited set of geometries. Therefore defining features in the sub-10 nm regime reproducibly and over large areas is difficult. Yet this regime is essential for achieving strong plasmonic coupling between adjacent structures.

We have tackled this problem by developing two new tools which can control the geometry and interparticle-distance of nanostructures initially fabricated with a traditional method. That is, these methods do not create nanoplasmonic structures from scratch, but instead they take structures created using a standard method,

and modify them to improve their nanoplasmonic properties. For the starting structures we focus on nanosphere lithography, since it can quickly and inexpensively produce nanoplasmonic structures over reasonably large areas. The resulting structures, namely nanoprism arrays, have been well-characterized by previous work.

In both this and the following chapter, we begin with nanoprism arrays fabricated via nanosphere lithography, and then tune this initial structure to vary the nanoplasmonic properties and create nanogaps. In Chapter 3 we use active polymers to achieve this manipulation, while in Chapter 4 we use electroless metal deposition.

3.1 Introduction

Since the beginning of the microfabrication era, devices for a wide range of nano- and microtechnology applications have been almost invariably fabricated on mechanically rigid surfaces [45]. In contrast, in the natural world, "substrates" are rarely rigid. As is well known in developmental biology, nano and microstuctures are often formed in flexible and changing environments during morphogenesis, and spacing of individual components may change significantly during the course of development [46]. An example relevant to optics is the morphogenesis of the compound eye in insects such as *Drosophila*, where the eye forms on a flat imaginal disc before developing into its complex 3-dimensional geometry [47–49]. Taking inspiration from this natural phenomenon, in this chapter we demonstrate the transformation capability of active soft-matter to define nanoscale architectures below the resolution limit of conventional lithography. In addition, the macroscale morphology can be manipulated into arbitrary 3-dimensional geometries, demonstrated with the fabrication of an omnidirectional nanoplasmonic antenna lens.

Shape-changing polymers, also called active or smart polymers, have been studied in recent years for their ability to deform significantly on the macro-scale when a stimulus is applied. Such stimulus may come in the form of thermal, electric, magnetic, or optical excitation [50–52]. While active polymers have been studied primarily at the macroscopic level, or at least the microscopic [53], we demonstrate that uniform deformations can be engineered to create high density nanostructures with nanogaps below the resolution limit of conventional methods. Control of deformation at the nanoscale allows the possibility of fabricating complex nanostructures in a way comparable to that achieved naturally during morphogenesis, as illustrated in Figure 3.1(a-d). Specifically, the contraction of an active polymer substrate allows nanostructure repositioning in a way analogous to apical constriction during morphogenesis (process shown in Figure 3.2).

The ability to control substrate dimensions after deposition of structures can confer the significant advantages over standard rigid substrates that biology has achieved [54, 55], such as i) the potential to alter structure-to-structure distance, surpassing

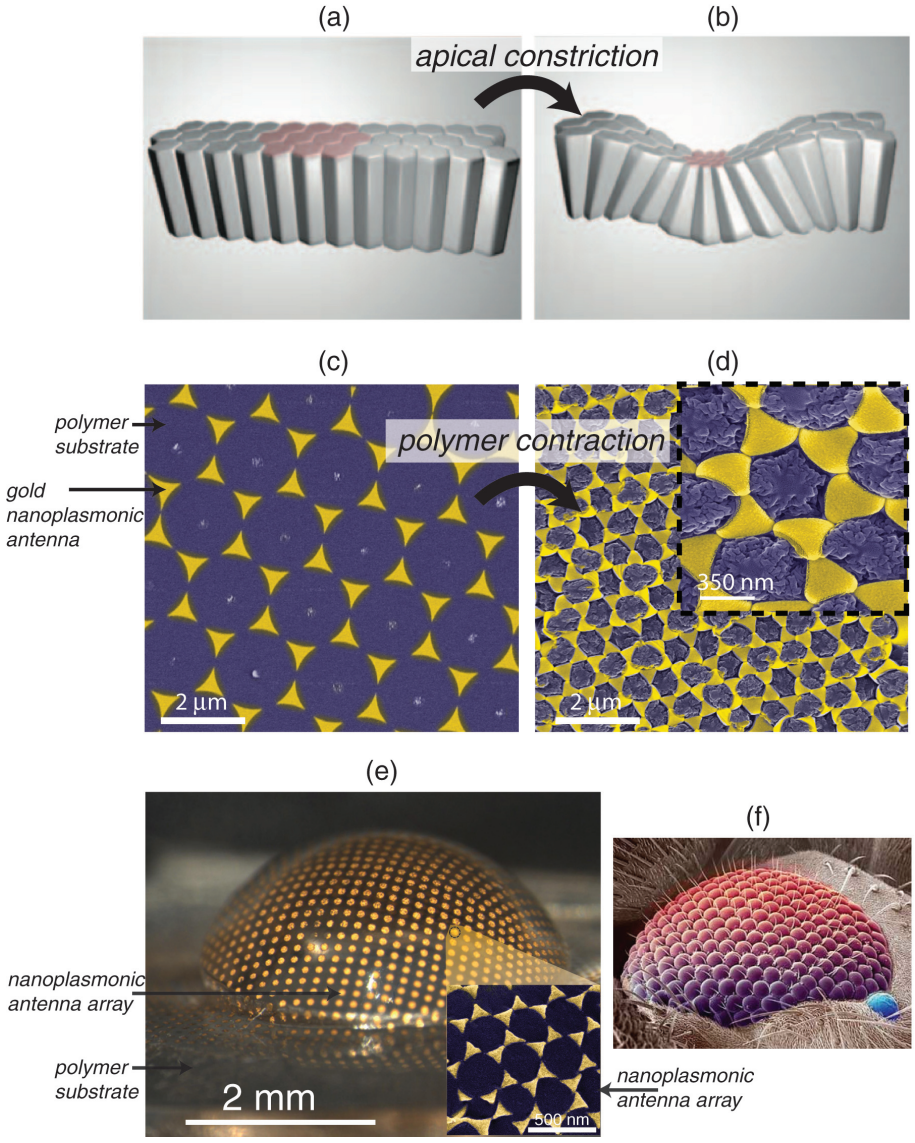

Figure 3.1: (a,b) Schematic of natural structure definition due to apical constriction; (c,d) active polymer fabrication uses an analogous process to produce ultra-dense nanoprism arrays; (e) omnidirectional nanoplasmonic antenna lens inspired by the compound eye; inset shows the nanoprism arrays, which are present at each "pixel" of the lens; (f) natural compound eye; panels (a-b) reprinted by permission from Macmillan Publishers Ltd: Nature Reviews Molecular Cell Biology 8, 633, copyright 2007; panel (f) courtesy of Raija Peura.

both resolution and structural density of the initial placement, and ii) the potential to deform nanostructures in a predictable way to form complex geometries without

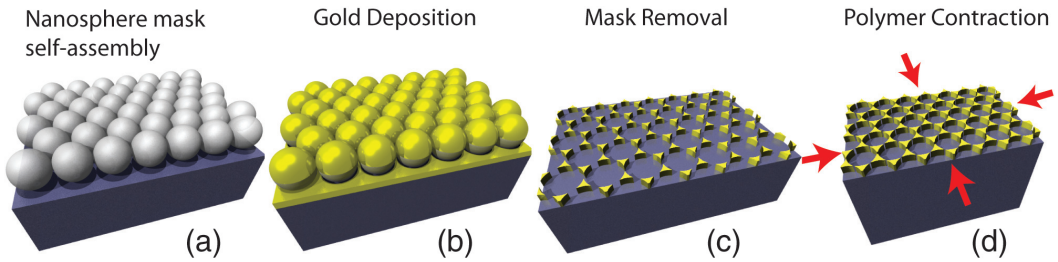

Figure 3.2: Active polymer nanofabrication process; (a) PS nanosphere self-assemble onto the active polymer substrate, (b) gold is evaporated on the substrate at normal incidence, (c) the nanospheres are removed, and (d) the polymer is thermally activated, resulting in contraction.

losing the valuable functions of the nanoscale devices. The former benefit is of wide interest in reducing feature size of devices, while the latter is of particular interest in microelectromechanical and nanoelectromechanical systems fabrication.

Nature often hierarchically combines components from the nano- to macro-scale to achieve a final structure [56]. Similarly, active polymers can be readily deformed into complex 3-dimensional geometries at the macroscale, while the nanoscale morphology is retained on the polymer surface. This provides a platform for integrating nanoarchitectures into stretchable devices ranging from flexible displays, to bio-inspired lenses, to biomedical systems [57]. We demonstrate a bio-inspired omnidirectional nanoplasmonic antenna array in Figure 3.1(e), based on the shape of the natural compound eye. The artificial eye is achieved by heating the contracted polymer until it is moldable (process shown in Figure 3.3), and its optical properties are discussed below.

Both the nano- and macro-scale deformations of active polymers are well-suited to the needs of nanoplasmonic antennas. Because the molecular detection sensitivity is closely related to the nanostructure geometry, the nanogap distance between structures, and the density of such structures [37, 58], active substrates offer the possibility of creating a new class of highly sensitive nanoplasmonic sensors. In addition, the local electromagnetic field controlled by nanoplasmonic antennas can be used to create new light sources, for example through second harmonic generation effects [9].

We demonstrate the potential of active polymer nanofabrication in creating ultradense nanoplasmonic antenna arrays. The nanoprisms are defined with nanosphere lithography, which is a well-characterized and cost-effective method for nanostructure patterning over large areas [5]. The size and periodicity of the nanoprisms can be tuned by choice of the nanosphere size. In addition, no high temperatures or corrosive chemicals are required, which makes processing fully compatible with the active polymer substrate used. After the nanoprisms are defined, the polymer is contracted

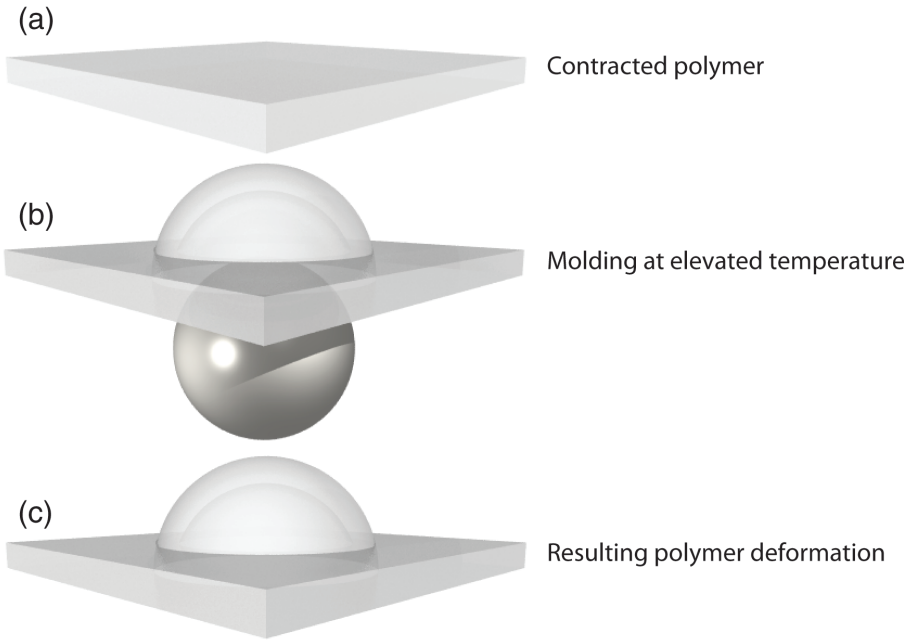

Figure 3.3: Macroscopic deformation of active polymers; (a) the contracted polymer is (b) heated and molded, and (c) cooled to achieve its final structure.

via thermal activation (process shown in Figure 3.2).

3.2 Methods

Materials: Colloidal polystyrene (PS) nanospheres of various diameters were purchased from Polysciences. Preheated stretched polystyrene substrate purchased from K & B Innovations.
Synthesis of Substrates: A closely packed (PS) nanosphere array on the polystyrene substrate was prepared as follows: the polymer sheet was cut into a $1.5 \times 1.5\,\mathrm{cm}^2$ square, followed by oxygen plasma treatment for 20 seconds (Plasma-Therm PK-12, at 50 sccm, 100 W) to make its surface hydrophilic. PS nanosphere solution and methanol were mixed at a $1:1$ ratio, and $10\,\mu$L of mixed solution was dropped onto the polymer substrate and allowed to evaporate, resulting in self-assembly of the PS nanospheres into a hexagonal array. The nanosphere-masked substrates were then loaded into an electron-beam thermal evaporator (Edwards EB3), and coated with a 2 nm Ti adhesion layer, followed by Au deposition of specified thickness. The PS nanospheres were then removed with clear tape (Scotch, 3M), resulting in a substrate covered with nanoprism arrays. Finally, the substrate was heated to 170°C for 3 mins, resulting in a biaxial contraction of 37.5%.

Characterization: The nanoprism arrays were characterized by scanning electron microscope (SEM) (S-5000, Hitachi). Extinction spectra were obtained by illuminating the sample with a broadband white light from a halogen lamp, and the transmitted light was collected by a microscope with spectrometer.
Model: To investigate the near-field properties of uncontracted and contracted nanoprisms arrays, we developed a 3-dimensional electromagnetic model using the commercial finite element software COMSOL. The software numerically solves over the domain of interest the time-harmonic Maxwell equations, which reduce to the Helmholtz equation [12]. We consider gold nanoprisms with complex permittivity ϵ given by an analytical model [43] of the experimental data [13] for bulk gold. The particles are assumed to be present in free space $\epsilon_m = 1$, and the permeability of both the particles and the surrounding medium are assumed to be $\mu = \mu_m = 1$. The incident electric field amplitude is assumed to be $|\boldsymbol{E}_i| = 1$, and scattering boundary conditions were used to eliminate nonphysical reflections at the domain boundaries. An adaptive mesh was used, and the mesh was refined until further refinements in element number or size of the domain did not cause changes in the result, verifying a converged model. We have also verified our model for geometries with known analytic solutions, such as the sphere [14, 59]. We model nanoprisms with a 50 nm height, and geometry produced by nanosphere diameters of 300 nm. To better simulate the physical structure, nanoprism tips are rounded with a radius of curvature of 2 nm.

3.3 Results and Discussion

The increase in density of the nanoprisms is defined by the contraction the active polymer, which for the polystyrene polymer substrate studied is approximately 14% of its original area. For the nanoprism arrays studied here, this strain is sufficient to create nanogaps and significant change in optical properties, but we note that larger strains (and hence increase in nanostructure density) are achievable; for example a 500% strain has been demonstrated using triblock liquid crystal polymers [60], which would potentially reduce polymer area to 4%. The reduction in area from the active polymer contraction allows the formation of nanostructures in densities above that which are initially defined, regardless of the initial fabrication technique.

Concomitant with the increase in density is the potential to create nanogaps between lithographically defined structures. In Figure 3.4(d-f), we illustrate the nanogap formation in more detail for nanoprisms lengths of 120 nm to 1.6 μm. The nanogaps in Figure 3.4(f) are clearly sub-10 nm, below the resolution limit of even electron beam lithography and focused ion beam (FIB) techniques. Nanogap formation allows the creation of tip-to-tip nanoprism structures (also called bow-ties), which have shown to be excellent substrates for localizing electromagnetic fields [61]. Since the local electromagnetic field increases with decreasing nanogap distance between the nanoprisms,

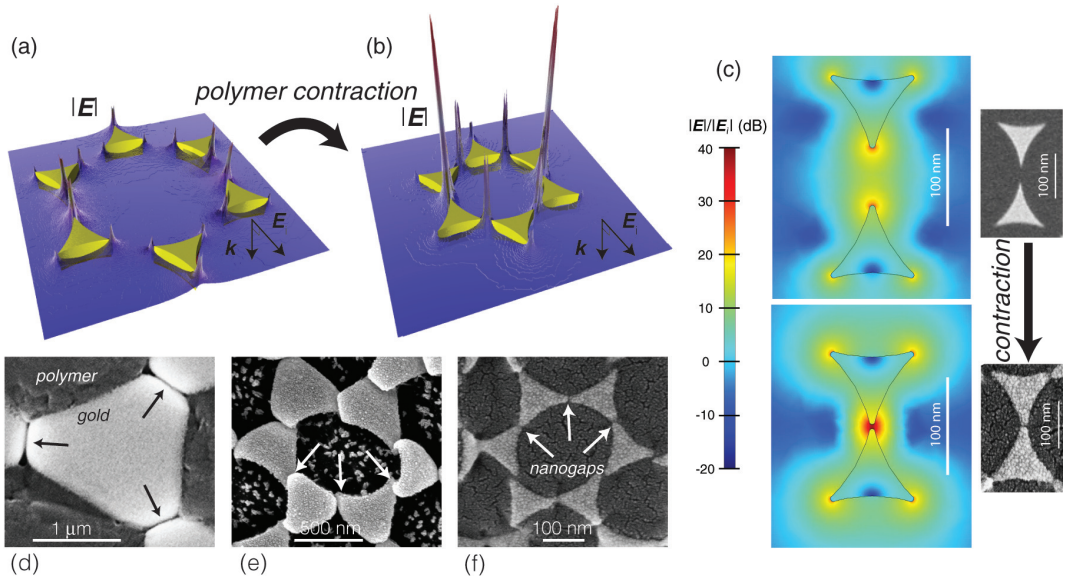

Figure 3.4: Active polymer fabrication of nanoprism arrays; (a)-(c) finite element simulation of electric field amplitude surrounding initial and contracted nanoprism arrays; (d)-(f) SEM images of nanogaps between gold nanoprisms of different sizes; nanoprism lengths are approximately (d) 1.6 μm, (e) 540 nm, and (f) 120 nm.

contracting the substrates should allow for significantly increased molecular sensitivity, as well as enhancing nonlinear effects such as second harmonic generation. Using finite element simulation, we show the order-of-magnitude improvement in local field enhancement upon contraction in Figure 3.4(a-c).

We next consider how deformation of the nanoprisms varies at different length scales. As shown in Figure 3.5, the final substrate morphology is sensitive to the initial nanostructure size and thickness, and buckling and delamination regimes can be distinguished. Assuming the mismatch strain between the gold nanoprisms and the polymer to be the strain induced by the contracting polymer, and the modulus $E = 78$ GPa and Poisson ratio $\nu = 0.44$ for gold, the mismatch stress between the nanostructures and the polymer is $\sigma_m = -52$ GPa.

To obtain a rough approximation of the stress required for buckling, we consider the formula for buckling of a circular patch of a thin film [62, ch. 5]:

$$\sigma_b = -1.2235 \frac{\bar{E}_f h_f^2}{a^2}, \tag{3.1}$$

where σ_b is the critical stress for the lowest axially symmetric buckling mode, $\bar{E}_f$ is the plane strain modulus, h_f is the film thickness, a is the debonded radius, and the negative sign indicates a compressive stress. This formula is a simplification of the

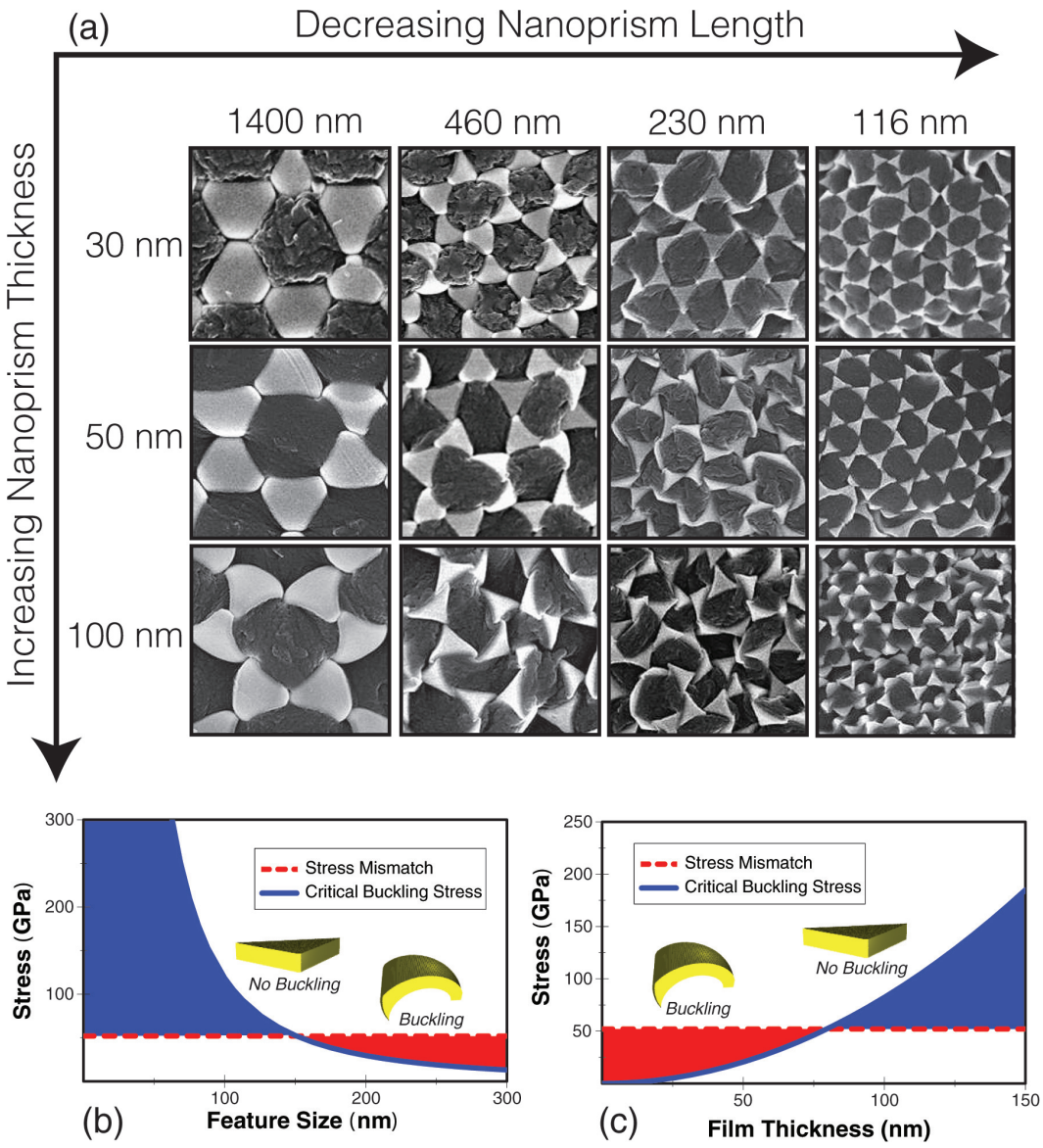

Figure 3.5: Matrix of the morphology achieved for varying gold nanoprism size and thickness; (a) representative SEM images; the different regimes of buckling and delamination can be understood with a basic analytical model shown in (b) and (c), as predicted by equation (3.1).

experimental case studied: an infinite film is assumed (compared to the experimental condition of finite nanoprisms) and the debonded region is assumed to be circular. Nonetheless, the theory provides a good qualitative picture of the physical scenario, and the results agree to an order-of-magnitude with experiment.

The results of equation (3.1) are shown in Figure 3.5(b-c). The stress mismatch allows for buckling to occur until a critical size is reached. Below this critical size, the stress required for buckling is higher than the stress mismatch, and the stress must be relieved by another mechanism, such as delamination. The effect of increasing the thickness of the gold layer is also predicted by equation (3.1). Since the critical buckling stress is proportional to the second power of the nanoprism thickness, thicker films result in reduced buckling for a given size. These predictions match well with experiment: as shown in Figure 3.5(a), buckling is clearly visible for larger and thinner nanoprisms, while smaller and thicker prisms tend to delaminate from the surface and "stand up."

We note that the useful increases in density, nanogap creation, and deformation are partially offset by a decrease in the order of the system: variations in the contraction behavior of the active polymer cause some defects to occur in the resulting nanoprism array. However this is not a fundamental limitation, and improvements in the uniformity of the polymer substrate should allow a reduction in the defects observed. Future research is needed to clarify the fundamental limits at which active polymers may uniformly contract, and how these limits depend on the form of activation (thermal, electrical, etc.).

The changes in substrate morphology are correlated with distinct changes in optical properties. Since the size and periodicity of nanoprisms created by nanosphere lithography are not traditionally independent, active polymer nanofabrication allows a separate handle for tuning nanoprism periodicity, and hence tunability of their spectra. Tunability is an essential characteristic of any plasmonic architecture designed for molecular detection: first, since tuning resonance to the "biological window" is necessary to prevent cellular damage, and second, because tuning to the vicinity of specific molecular resonances can create large increases in both SERS [63] and LSPR-shift [64] signals. As shown in Figure 3.6, upon substrate contraction the extinction peak is blueshifted $200-300\,\mathrm{nm}$ upon contraction, with thicker nanoprisms exhibiting a greater blueshift after contraction.

Three effects contribute to the observed blueshift. Radiative dipole interactions between the nanoprisms cause a blueshift as the lattice spacing is decreased [65]. In addition, touching nanoprisms are no longer electrically isolated, again resulting in a blueshift. Finally, the deformation of individual nanoprisms may also contribute to the observed shift. More study is needed to precisely determine the relative importance of each of these effects. We note that for small and thick nanoprisms ($s = 95\mathrm{nm}$, $h = 45\,\mathrm{nm}$ in Figure 3.6(a)) the lack of a uniform nanostructure prevents a clear extinction peak from emerging for the contracted polymer, consistent with the lack of buckling deformation in this regime.

As discussed above, the contracted polymer substrates can be readily molded into 3-dimensional shapes, such as the lens shown in Figure 3.1(e). We show the uniformity

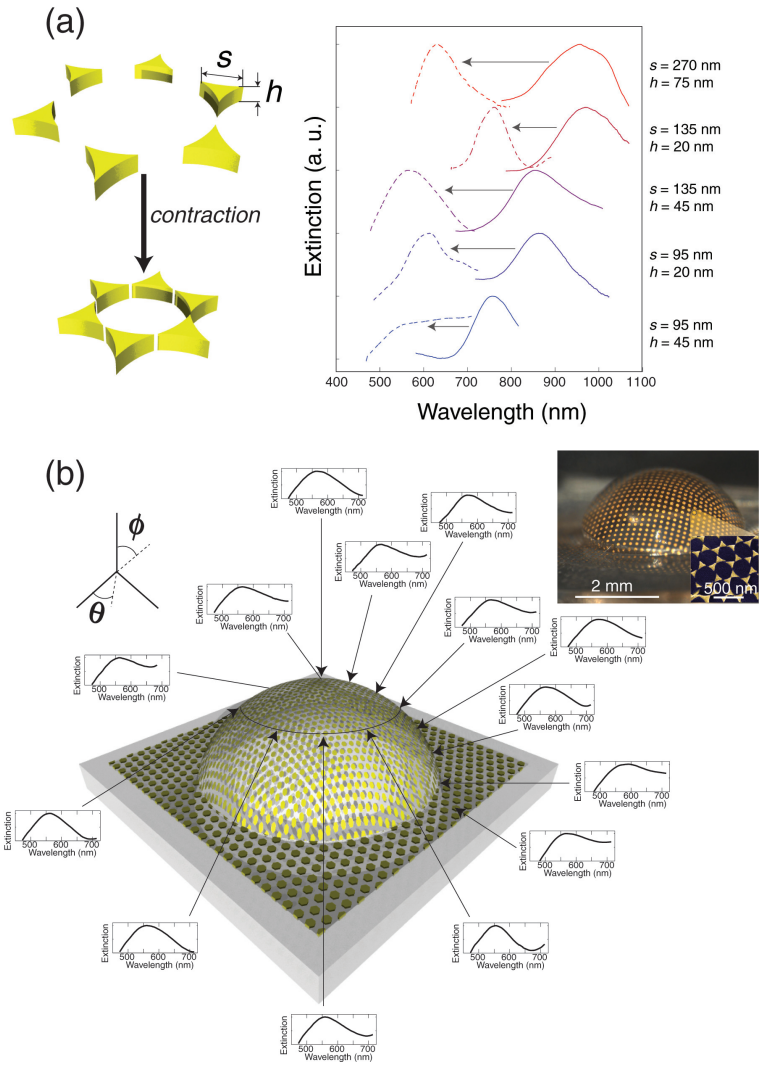

Figure 3.6: Optical changes with substrate contraction; (a) (left) schematic of nanoprism contraction and (right) representative extinction spectra of nanoprism arrays before (solid line) and after contraction (dashed line) for varying nanoprism size and height; (b) extinction spectra taken with varying ϕ and θ positions demonstrate the uniformity of pixels in the omnidirectional nanoplasmonic antenna lens shown in inset.

of spectra taken from different pixels of this substrate in Figure 3.6(b). Despite the significant change in structure curvature on the macroscale, the spectra obtained from varying positions on the lens are nearly identical; hence, we have achieved an omnidirectional nanoplasmonic antenna lens. By integrating such devices with flexible electronics [57], individual pixels may be addressed simultaneously, thus achieving a

"plasmonic compound eye."

3.4 Conclusion

To conclude this chapter, we have proposed a biologically inspired morphogenetic transformation of hybrid metal and polymer structures for defining nanostructure morphology, and have demonstrated its utility in creating omnidirectional nanoplasmonic antenna arrays. Active polymer nanofabrication allows the potential to alter structure-to-structure distance down to sub-10 nm, surpassing both resolution and structural density of the initial placement. In addition, polymer molding offers macroscopic deformation of plasmonic architectures into arbitrary 3-dimensional geometries. We have demonstrated the size-dependent mechanical response of nanoplasmonic prism antenna arrays fabricated with active polymer fabrication, and have correlated the results with analytic theory. Finally, we have correlated the changes in morphology with optical response. We believe active polymer nanofabrication will have wide utility for developing high density device architectures for MEMS, NEMS, and nanoplasmonic devices.

Chapter 4

Nanogap Formation via Electroless Deposition

4.1 Introduction

In the previous chapter, we introduced active polymer fabrication, which uses the contraction of polymers to manipulate the morphology of nanoplasmonic structures. Here, we present a second approach for controlling nanogaps in plasmonic devices. We demonstrate that electroless deposition provides a simple but powerful tool for the fine control of plasmonic nanostructures. Using gold nanoparticles (nanoprism arrays) initially fabricated with nanosphere lithography, we show electroless deposition of gold in both bulk solution and in Y-channel microfluidic devices can tune the morphological and nanoplasmonic properties of the device. We characterize the change in the nanogap and morphology, plasmonic optical properties, and surfaced-enhanced Raman spectroscopy (SERS) signal before and after electroless growth.

Electroless plating, (also called chemical or auto-catalytic plating) is the deposition of metal *via* chemical reactions in an aqueous solution, and without the use of external electrical power (as in the case of electrodeposition). Electroless deposition is attractive due to its simplicity, and minimal equipment requirements: in comparison to electrodeposition [66], electroless deposition does not require a conductive substrate, electrodes, and power supply. Since it does not require light excitation (as used in photochemical assisted deposition [67]) it can be carried out over arbitrarily large areas. Processing can be conducted in open air conditions at room temperature.

We characterize the electroless deposition of nanostructures using two complementary techniques: bulk deposition and microfluidic deposition (4.1(a-b)). Bulk deposition is carried out over arbitrarily large areas of substrate in solution. The primary advantage of this technique is its simplicity, and by specifying the deposition time we are able take "snapshots" of nanostructure growth over time. In contrast, mi-

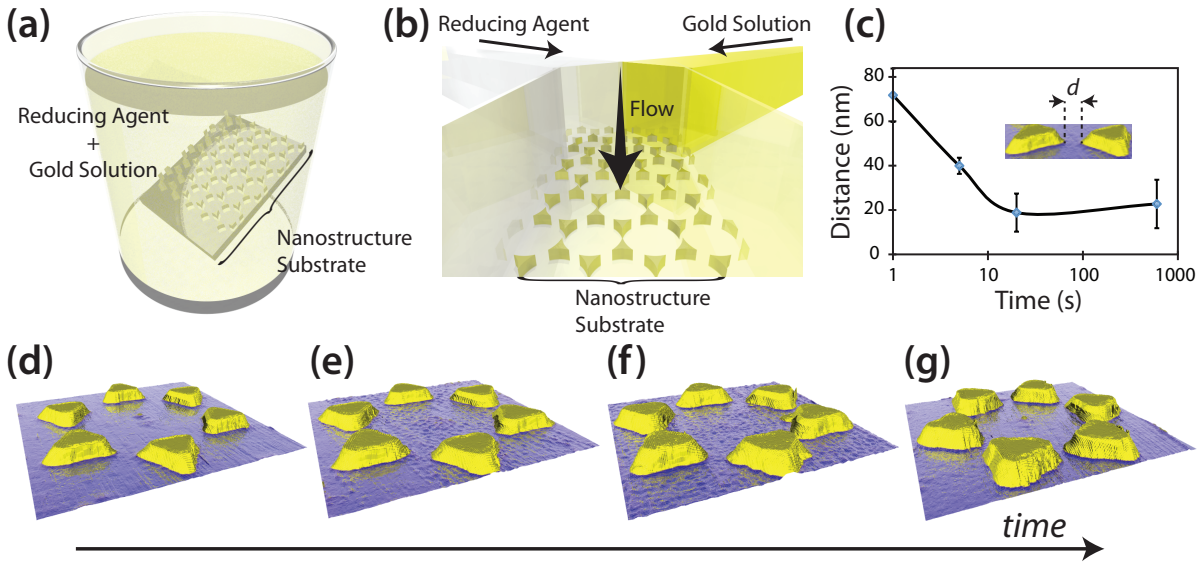

Figure 4.1: Electroless growth of nanoprisms; schematic of electroless growth of nanoprism arrays in (a) bulk solution and (b) a microfluidic Y-channel device; (c) average distance between adjacent triangles as a function of deposition time (error bars represent one standard deviation, n=6); AFM height maps of representative nanoprisms after electroless growth in bulk solution for (d) 0 s, (e) 5 s, (f) 20 s, and (g) 10 min.

crofluidic deposition allows us to carefully control flow and reduction of gold solution over both space and time, and allows us to observe the dynamic change in nanoplasmonic optical properties in real time. Additionally, microfluidics allows deposition with small volumes ($\sim$50 μL), which saves both cost and waste.

4.2 Methods

The gold nanoprism arrays were fabricated using standard nanosphere lithography [5], as discussed in Chapter 3. After the nanoprism arrays were fabricated, electroless deposition was carried out as follows. For the bulk deposition, first an aqueous solution of 3.2 mM sodium borohydride ($NaBH_4$, Alfa Aesar) was freshly prepared. The substrates were then submerged into a commercial sulfite gold plating solution (Techni-Gold 25 ES RTU, Technic), and the deposition was initiated by adding the sodium borohydride solution in a 1:1 volume ratio with the gold solution while the substrate was emerged. The sodium borohydride reduces the gold ions in solution, which preferentially attach to the gold nanostructure surface. After a specified deposition time, the substrates were removed from the solution and immediately cleaned

with deionized water. We note that lower concentrations of sodium borohydride became ineffective in reducing the gold ions in solution over several hours, while higher concentrations caused the gold to immediately "crash," resulting in uncontrollable deposition. At the sodium borohydride concentration used, gold particulate gradually became visible, but did not accumulate noticeably on the glass substrate. However, further fine tuning of the reducing agent is a potential area of focus in the future development of this method.

For deposition in microfluidic devices, an SU-8 mold was prepared using a chrome mask and standard lithography, and Polydimethoxysilane (PDMS) devices were fabricated from the mold. Devices consisted of a Y-channel, with two inputs and one output. Before deposition, the devices were vacuum loaded with water: devices were submerged in water and placed in vacuum for ∼30 min. For deposition, in one arm of the "Y," the gold plating solution flowed, while the other arm contained the sodium borohydride reducing solution as described above. The flow in both inputs was controlled by a syringe pump with a flow rate of 10 μL/min.

4.3 Results and Discussion

Using bulk electroless deposition for specified times, we characterized the change in substrate morphology as a function of time using atomic force microscopy (AFM), shown in 4.1(c-g). The distance between the tips was quantified for 6 data points, where the distance was taken at a height of 3 nm from the substrate surface (4.1(c)). The distance between adjacent nanoprisms decreases approximately linearly with the log of time for the first 20 seconds of deposition, from the initial gap distance of ∼70 nm to a final gap distance of ∼20 nm. Longer times did not result in an appreciable change in morphology. We expect that buildup on the nanoparticle surface (e.g. charge or organic molecules) was the cause of this observation; growth did not noticeably resume after submerging the substrate in a fresh solution, suggesting the slowing of growth is not a reagent limited process. Of course, it is not just the gap size that is affected during deposition; each nanoprism also grows in size. Notably, the overall shape of the nanoprisms, including their sharp features, appear to be well retained during growth, in contrast to structures altered with electrodeposition [66].

The nanoplamonic optical properties of nanoprism arrays are highly sensitive to both the particle geometry and interparticle distances. Tunability is an essential characteristic of any plasmonic architecture designed for molecular detection: firstly, since tuning resonance to the "biological window" is necessary to prevent cellular damage, and secondly, because tuning to the vicinity of specific molecular resonances can create large increases in both SERS [63] and LSPR–shift [64] signals. We show the evolution of the absorption spectra of gold nanoprism arrays during electroless growth in Figure 4.2. A redshift in the spectrum is expected due to increased plasmonic

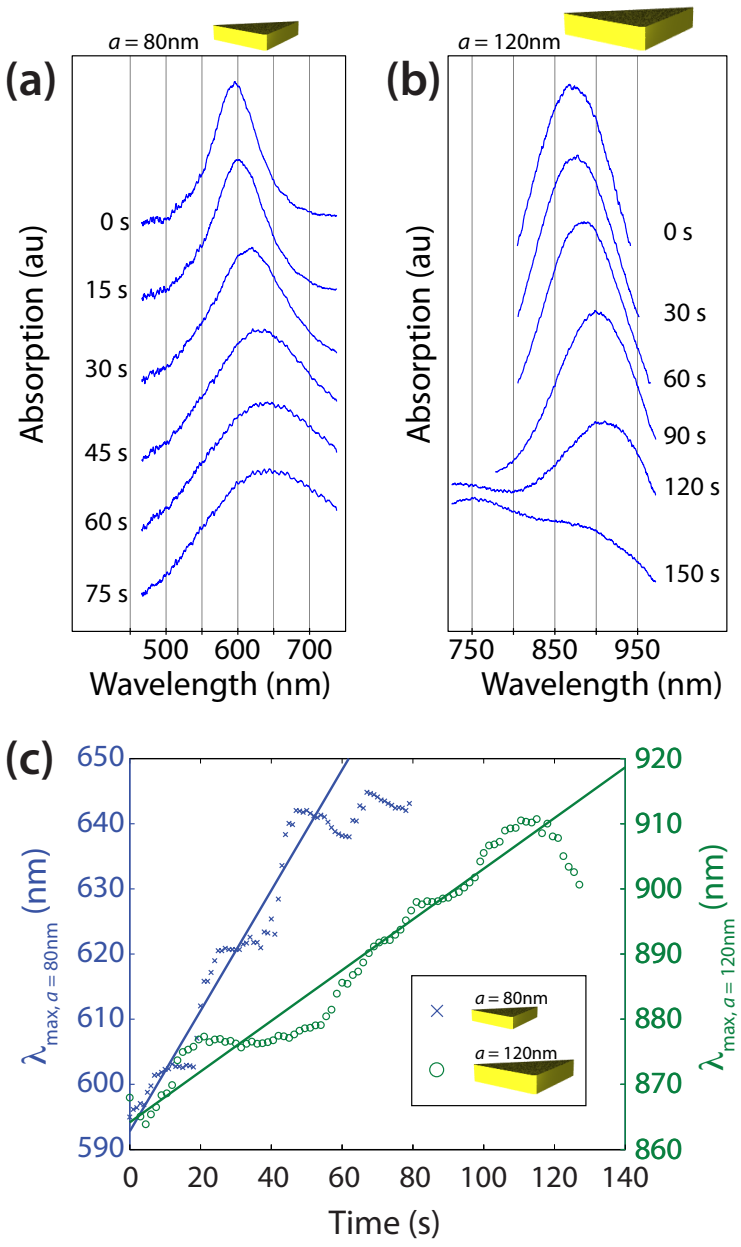

Figure 4.2: Realtime observation of electroless growth; absorption spectra evolution during electroless growth inside a microfluidic Y-channel device for (a) 80 nm (b) 120 nm nanoprisms; (c) peak wavelength as a function of time during realtime growth.

coupling between the nanoprisms as the gap between them decreases [68], and this is indeed observed. Additionally, the change in shape and size of individual nanoprisms

may contribute to the observed shift. As the nanoprisms merge together to form a continuous gold film, the plasmon peak broadens and eventually vanishes, as expected.

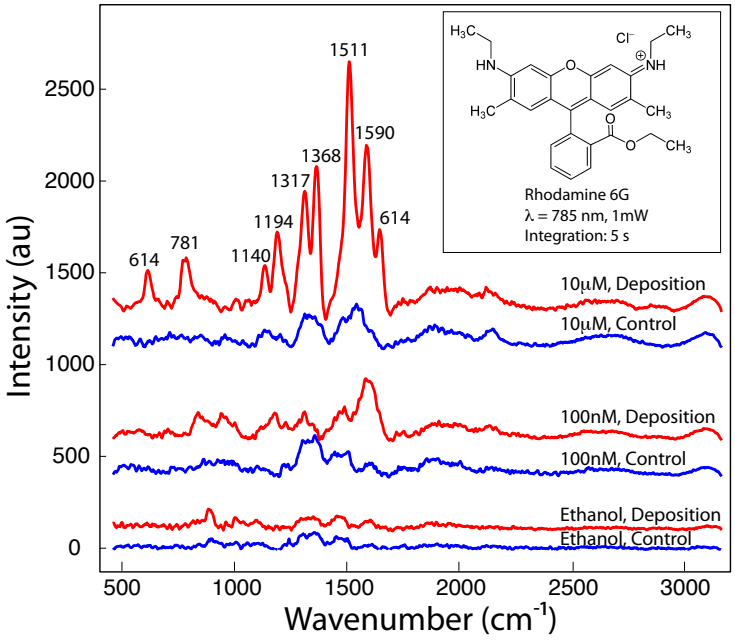

Figure 4.3: Effect of electroless deposition on SERS spectra; comparison of normalized SERS signal of R6G for gold nanoprism arrays before and after electroless deposition (10 min in bulk solution); inset shows molecular structure of R6G and measurement conditions.

Both the decrease in nanogap distance and optical redshift observed during electroless growth suggest an improvement in the enhancement of the electric field at resonant wavelengths. To test this, we investigated the SERS signal of a common test molecule, Rhodamine 6G (R6G). We tested the SERS signal before and after 10 min electroless deposition in bulk solution with an excitation wavelength of 785 nm, near the resonance wavelength of the structures. We observed a consistently higher SERS signal for the electrolessly deposited structures, as shown in 4.3: Electroless deposition extended the limit of detection of the device by 2 orders of magnitude, and at the signature peak at 1511 cm^{-1} at a concentration of 10μM, the deposited structure shows an 8-fold higher signal. We emphasize that the versatility of electroless deposition should allow similar improvements for other plasmonic structures.

4.4 Conclusion

To conclude, we have introduced electroless deposition as a method to tune plasmonic nanoarchitectures, and we have characterized the morphological, optical, and SERS response for the electroless deposition of gold on nanoprism arrays fabricated with nanosphere lithography. The gap distance between nanoprisms was reduced by a factor of 4 within tens of seconds. Using microfluidic Y-channels, we observed the realtime evolution of the optical spectrum as nanoprisms grew and merged into a gold film. The SERS sensitivity was shown to have increased two orders of magnitude after electroless deposition. We believe electroless deposition provides a powerful and widely useful tool for fine control and nanogap creation for a wide range of structures.

Chapter 5

Nanocrescent

> "Coming together is a beginning. Keeping together is progress. Working together is success."
>
> Henry Ford

As was shown theoretically in Chapter 2, shape is an effective way to tune the resonances of both the near and far fields of nanoplasmonic antenna. Tunability is essential for nanoplasmonic antennas designed for molecular detection, since i) resonances often must be tuned to the "biological window" where absorption is low, and ii) tuning near molecular resonances may greatly increase spectroscopic signal [63, 64].

Next, in this and the following three chapters, we investigate the issue of geometry in great detail for four structures. We are particularly interested in systems which utilize plasmon-coupling; that is, the close proximity of two or more components of the nanoplasmonic system causes their resonances to be linked together. As will be demonstrated, the coupling in these structures can cause high electric fields ideal for molecular detection.

Four such structures will be discussed: the nanocrescent, the crescent-shaped nanohole, the plasmon enhanced particle-cavity (PEP-C) system, and the core-satellite system. The nanocrescent and its counterpart, the crescent-shaped nanohole, utilize both sharp tips and "intra-particle coupling" to achieve high local field enhancement. The PEP-C system combines particle and cavity geometries to create a high density of hot-spots. Finally, the core-satellite system is based on the interaction of a central nanoparticle with multiple smaller particles.

5.1 Introduction

This chapter focuses on nanoplasmonic resonances of the nanocrescent structure, shown in Fig. 5.1. Nanoplasmonic molecular sensors must exhibit plasmon resonance in the near-infrared (NIR) regime [69], and must be mobile, robust, non-toxic, manufacturable, and produce high local field enhancement within a single probe. While nanorods or nanoshells can meet many of these requirements, typically these structure only demonstrate high field enhancement when they aggregate into clusters. While *inter-particle* plasmon coupling has shown to create high field enhancement between structures such as spheres [70], cylinders [71], rods [72], triangles [61], and squares [73], these systems strongly rely on a several nanometer distance (nanogap) between two or more particles, which is typically random and difficult to control. As a better alternative to interparticle coupling of these structures, the nanocrescent was proposed to utilize *intra-particle* coupling, and achieve high local field enhancement in a single probe. In addition, the sharp tips of the nanocrescent allow it to take advantage of the lightning rod effect as well as the capacitor effect (through intra-particle coupling).

Nanocrescents have begun to be established as powerful plasmonic biosensors in recent years, both theoretically [74, 75] and experimentally [76–82]. Despite these results, there is no systematic study of the nanocrescent available to answer key questions regarding nanoparticle geometry: what is the extent of the plasmon resonance tunability of the nanocrescent, and how does geometry affect plasmon resonance? In addition, what are the critical features necessary to obtain high local field enhancement? In this chapter we focus on computation to elucidate these issues.

We show that by varying the nanocrescent geometry, the plasmon resonance peak can be tuned into the near-infrared and local field enhancement can be increased significantly, with maximum enhancement of the electric field amplitude reaching approximately 100 for realistic geometric parameters. Because of its wide tunability, high local field enhancement, and geometry which utilizes both sharp features and intra-particle coupling, the nanocrescent is a structure well-suited for *in vivo* cellular imaging as well as *in vitro* diagnostic applications.

5.2 Model

The geometry of the nanocrescent, shown in Figure 5.1, is defined by four parameters: an outer radius r_o, an inner radius r_i, the center-to-center distance between the circles (cavity offset) d, and the fillet radius of the sharp tips s. Two distinct geometries bear the title nanocrescent: the geometry resulting from extruding Figure 5.1b out of the page, and the geometry resulting from revolving the same figure about the vertical axis. The "revolved" nanocrescent shown in Figure 5.1a was fabricated by depositing

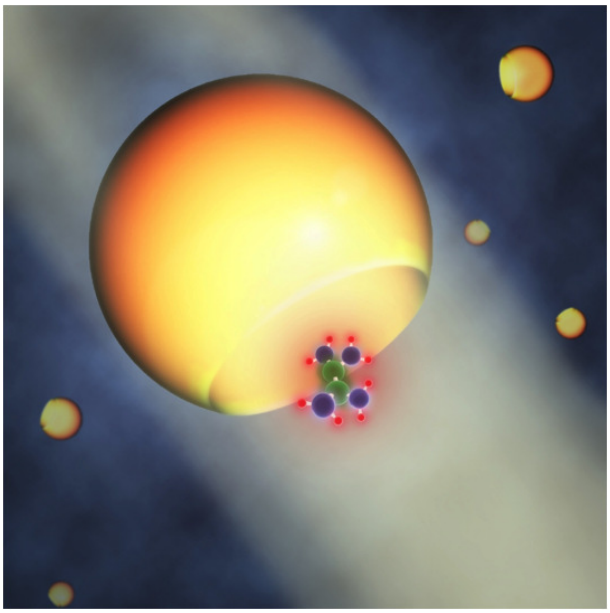

(a)

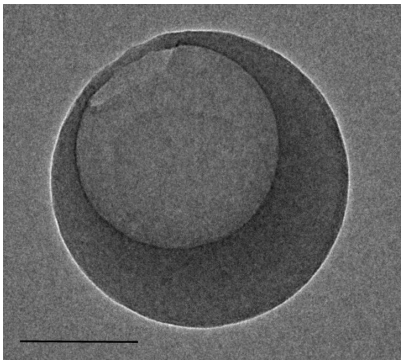

(b)

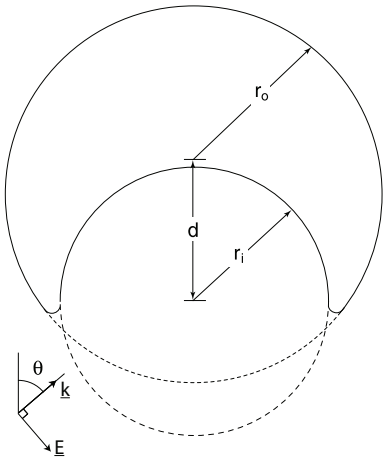

(c)

Figure 5.1: The nanocrescent; (a) artistic rendering, (b) TEM image of a 3D nanocrescent (scale bar represents 100 nm) and (c) diagram of the nanocrescent illustrating key geometric parameters.

a thin gold layer on polystyrene (PS) nanospheres at specified angles, followed by removal of the nanospheres, as described elsewhere [78]. A similar process is also discussed in further detail in the following chapter.

We consider a 2D gold nanocrescent present in free space (vacuum) with a trans-

verse magnetic (TM) plane wave incident at an angle θ measured from the vertical axis. We assume the relative permeability of gold $\mu_r = 1$ and the complex permittivity ϵ to be a function of wavelength [83]. A finite element model was developed using the commercial software *COMSOL* to solve over the domain of interest the time-harmonic Maxwell equations, which reduce to the Helmholtz equation [12]. The domain consisted of the 2D nanocrescent, a region of free-space (greater than half the free-space wavelength) surrounding the nanocrescent, and a perfectly matched layer (PML) to eliminate nonphysical reflections at the domain boundaries [84]. Scattering boundary conditions were used to further eliminate nonphysical results. An adaptive mesh was used, and the mesh was refined until the maximum electric field converged. We selected the finite element method primarily because of the ability to adaptively mesh, and because it has been shown to be advantageous over the finite difference time domain (FDTD) method for complex geometries [85].

We briefly note that we have observed the local field distribution for 3D (i.e. "revolved") nanocrescents to be similar to that of nanocrescents in 2D, with the high local field enhancement extending around the sharp edge in 3D. The 3D nanocrescent appears to follow trends similar to those discussed in this chapter; however, the 2D models discussed in this chapter are strictly valid only for nanocrescents "extruded" to very large thicknesses. The 2D study was chosen primarily because it allowed the vast parameter space of nanocrescent geometries to be investigated in a timely manner, where this would not be feasible for 3D geometries due to the intensive computation required.

5.3 Results and Discussion

Unless otherwise noted, we have chosen a nanocrescent with the nominal parameters $r_o = 70\,\text{nm}$, $r_i = 50\,\text{nm}$, $d = 40\,\text{nm}$, $s = 1\,\text{nm}$, and $\theta = 0°$. In all cases we compute the maximum electric field enhancement, defined as the ratio of the maximum value of the electric field amplitude $|\vec{E}|_{max}$ to the amplitude of the incident field $|\vec{E}_i|$. The maximum field enhancement occurs near the tips of the nanocrescent in all cases we have studied. We graphically depict the enhancement on a dB scale, defined as $10\log_{10}(|\vec{E}|/|\vec{E}_i|)$.

We first consider varying the outer radius r_o of the nanocrescent and incident free-space wavelength λ_0, while keeping the other parameter ratios fixed. Thus, all geometric parameters can be linearly scaled, resulting in a change in the overall size of the nanocrescent while keeping its relative geometry fixed. In this way, we observe how the plasmon band of the nanocrescent varies with the nanocrescent size as shown in Figure 5.2. The resonance peak of the nanocrescent is red-shifted as the nanocrescent size increases, and the relationship is roughly linear. The red-shift is also accompanied by a broadening of the peak, and is consistent with the size-effect

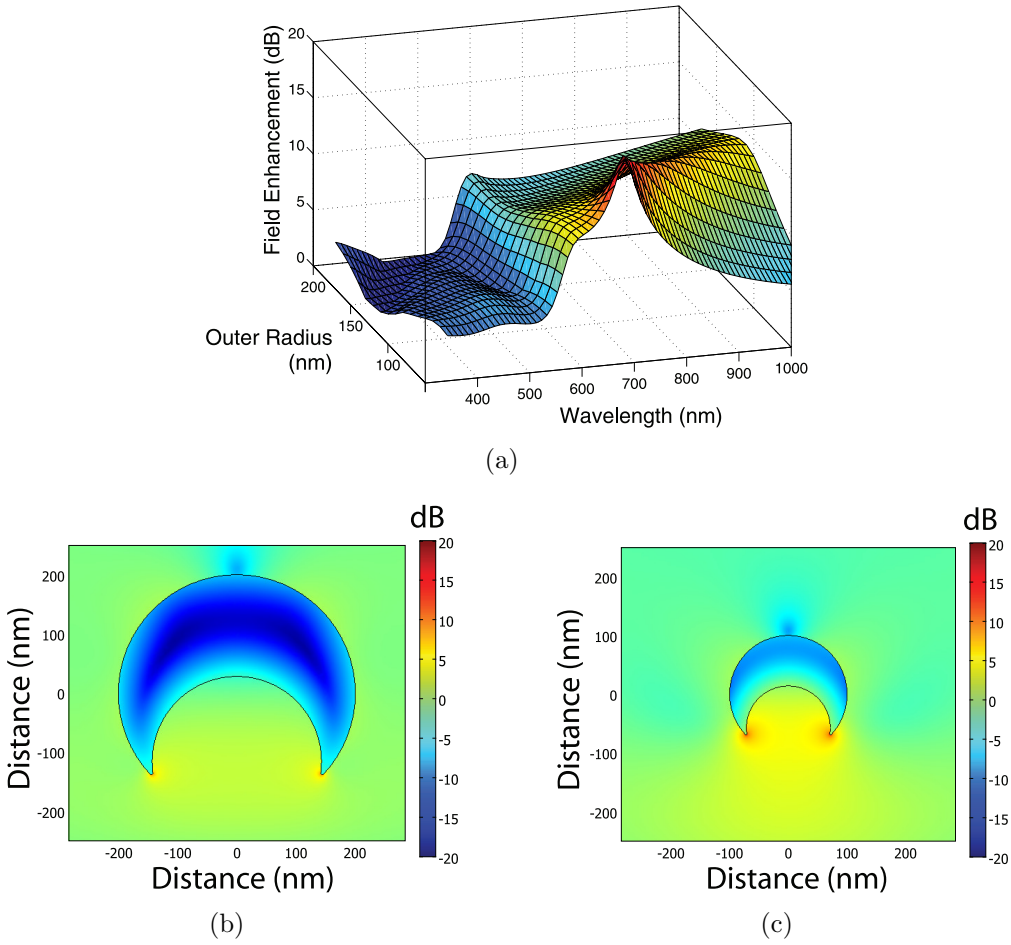

Figure 5.2: (a) Maximum local field enhancement as a function of outer radius r_o and incident free-space wavelength λ_0, (b) field distribution for $r_o = 200\,\text{nm}$, $\lambda_0 = 785\,\text{nm}$, and (c) field distribution for $r_o = 100\,\text{nm}$, $\lambda_0 = 785\,\text{nm}$ ($r_i = 50r_o/70$, $d = 40r_o/70$, $s = r_o/70$, $\theta = 0°$).

observed in gold nanoparticles [86], and is also consistent with recent experimental studies of the nanocrescent [79, 80]. Physically, the peak resonance is characterized by a dipole-like resonant coupling between the tips.

Significant plasmon band tuning can also be seen by varying the cavity offset d, keeping the other parameters constant. As shown in Figure 5.3, by decreasing d, the plasmon resonance peak can be brought well into the NIR regime. Varying d affects the tip-to-tip distance of the nanocrescent, and as d is reduced, dipole-like coupling increases between the tips (Figure 5.3b). This result is consistent with experimental results showing in increased resonance for decreasing tip-to-tip distance [79, 81]. We also note that varying d has the effect of changing the thickness of the

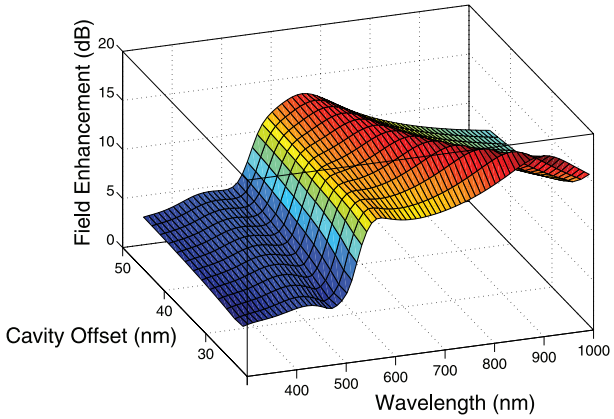

(a)

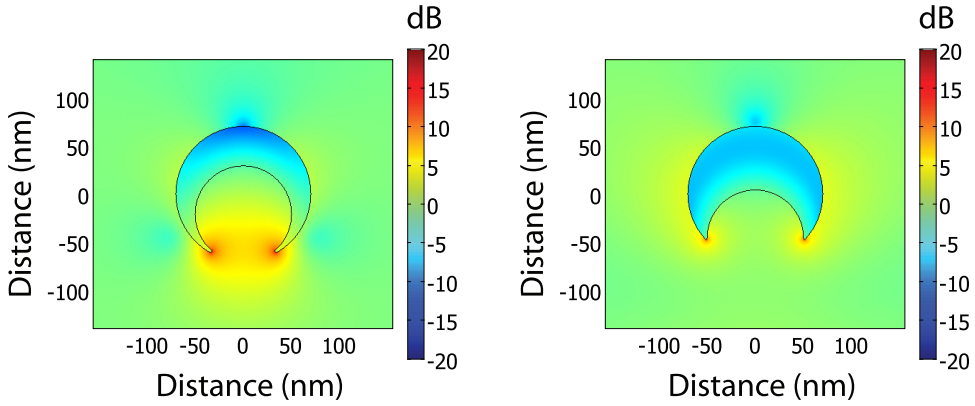

(b) (c)

Figure 5.3: (a) Maximum local field enhancement as a function of cavity offset d and incident free-space wavelength λ_0, (b) field distribution for $d = 21\,\text{nm}$, $\lambda_0 = 785\,\text{nm}$, and (c) field distribution for $d = 46\,\text{nm}$, $\lambda_0 = 785\,\text{nm}$ ($r_o = 70\,\text{nm}$, $r_i = 50\,\text{nm}$, $s = 1\,\text{nm}$, $\theta = 0°$).

nanocrescent shell, and tuning in this manner might be thought of as analogous to plasmon resonance tuning in metallic nanoshells [87, 88]. Since high enhancement can be achieved for fairly large tip-to-tip distances (e.g. 50 nm in Figure 5.3b) and enhancement does not increase significantly as the distance is reduced, the high enhancement is not simply due to the capacitor effect between the tips. Instead, the shape of the nanocrescent is being tuned to allow a stronger dipolar resonance.

Varying the inner radius r_i has comparatively little affect on the plasmon band, as shown in Figure 5.4. However, decreasing r_i reduces the tip-to-tip distance, increasing coupling between the tips, and affecting the field distribution (Figure 5.4b). Physically, one would expect the optimum wavelength for the dipole-like resonance

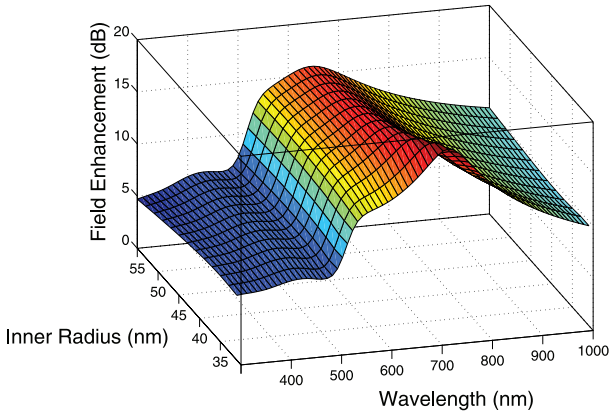

(a)

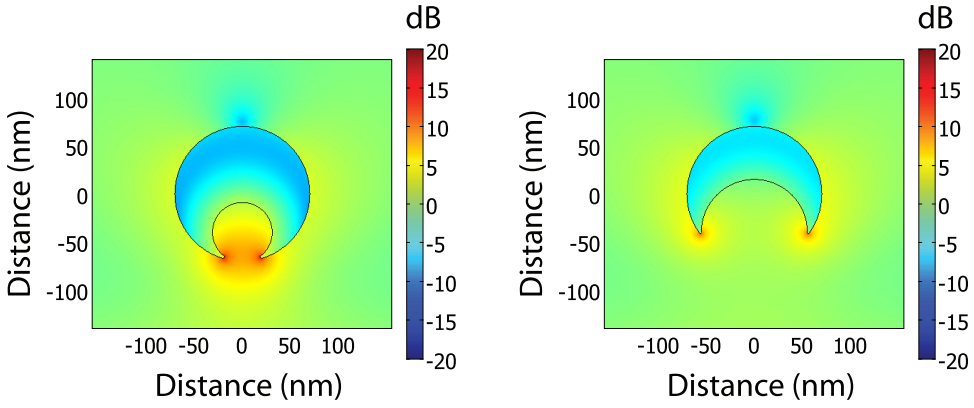

(b) (c)

Figure 5.4: (a) Maximum local field enhancement as a function of inner radius r_i and incident free-space wavelength λ_0, (b) field distribution for $r_i = 31\,\text{nm}$, $\lambda_0 = 785\,\text{nm}$, and (c) field distribution for $r_i = 55\,\text{nm}$, $\lambda_0 = 785\,\text{nm}$ ($r_o = 70\,\text{nm}$, $d = 40\,\text{nm}$, $s = 1\,\text{nm}$, $\theta = 0°$).

between the tips to depend on their distance; specifically, a redshift is expected as the distance is reduced, as can be observed in Figure 5.4.

In experimental practice, it is difficult to fabricate nm and sub-nm sharp features such as the tips of the nanocrescent. For this reason, the sharp tips of the nanocrescent were rounded with a fillet radius s. As shown in Figure 5.5, varying the fillet radius does not significantly affect the plasmon band; thus, the plasmon resonance of the nanocrescent is fairly robust with respect to the tip sharpness. The maximum field enhancement, however, can be increased significantly as s decreases, especially below 1 nm. We have observed the phenomenological relationship $|\vec{E}|_{max}/|\vec{E}_i| = a + b\,s^{-1/2}$, where a and b are constants which depend on the wavelength and geometry. As can

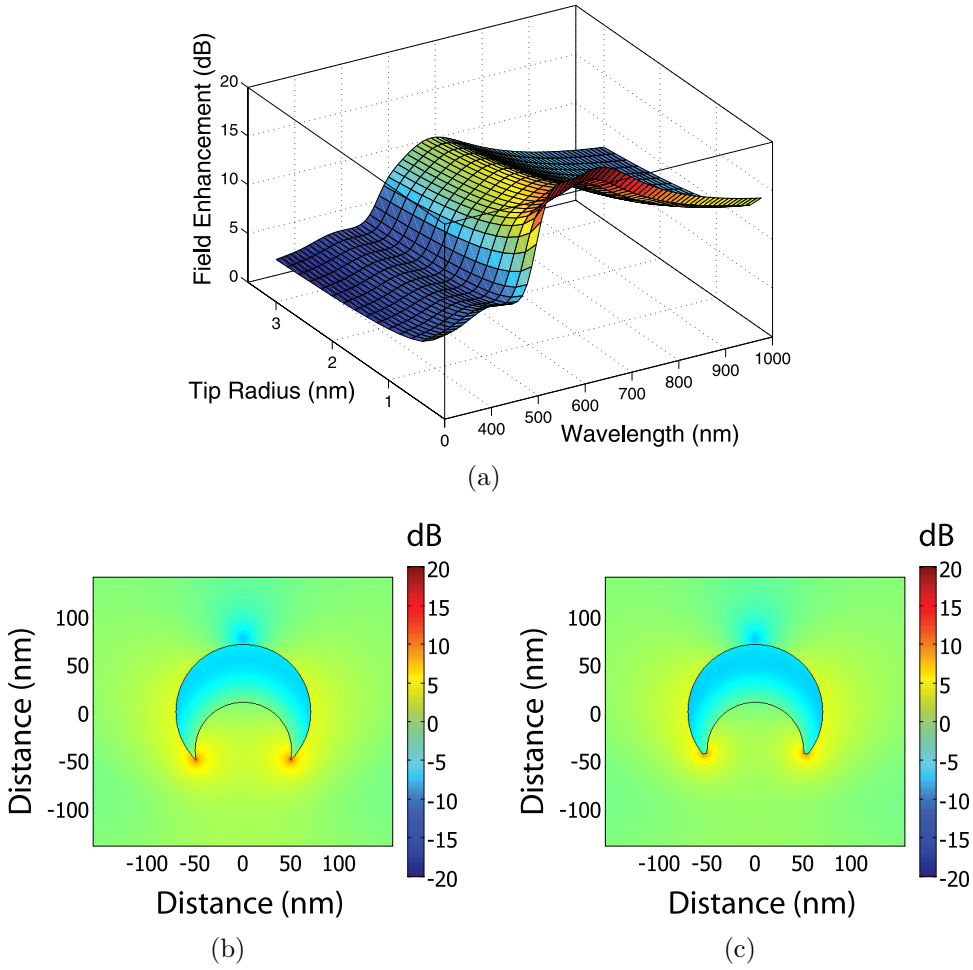

Figure 5.5: (a) Maximum local field enhancement as a function of fillet radius s and incident free-space wavelength λ_0, (b) field distribution for $s = 0.2\,\text{nm}$, $\lambda_0 = 785\,\text{nm}$, and (c) field distribution for $s = 3\,\text{nm}$, $\lambda_0 = 785\,\text{nm}$ ($r_o = 70\,\text{nm}$, $r_i = 50\,\text{nm}$, $d = 40\,\text{nm}$, $\theta = 0°$).

be seen in Figures 5.5b and 5.5c, the field enhancement remains highly localized near the sharp tips. While increasing the sharpness of the tips increases the "lighting rod" effect, thus increasing enhancement in close proximity to the tips, it has little affect on the dipole-like coupling between the tips or cavity. We note that the multiple nodes for resonant coupling of the sharp tip noted previously [74] vanish for the more physical tip radii chosen here.

Figure 5.6 shows the result of varying the angle of incidence θ of the incoming plane wave. A splitting of the plasmon resonance peak is prominent when θ is between 90° and 135°, agreeing with earlier results [74]. It is clear from Figures 5.6b

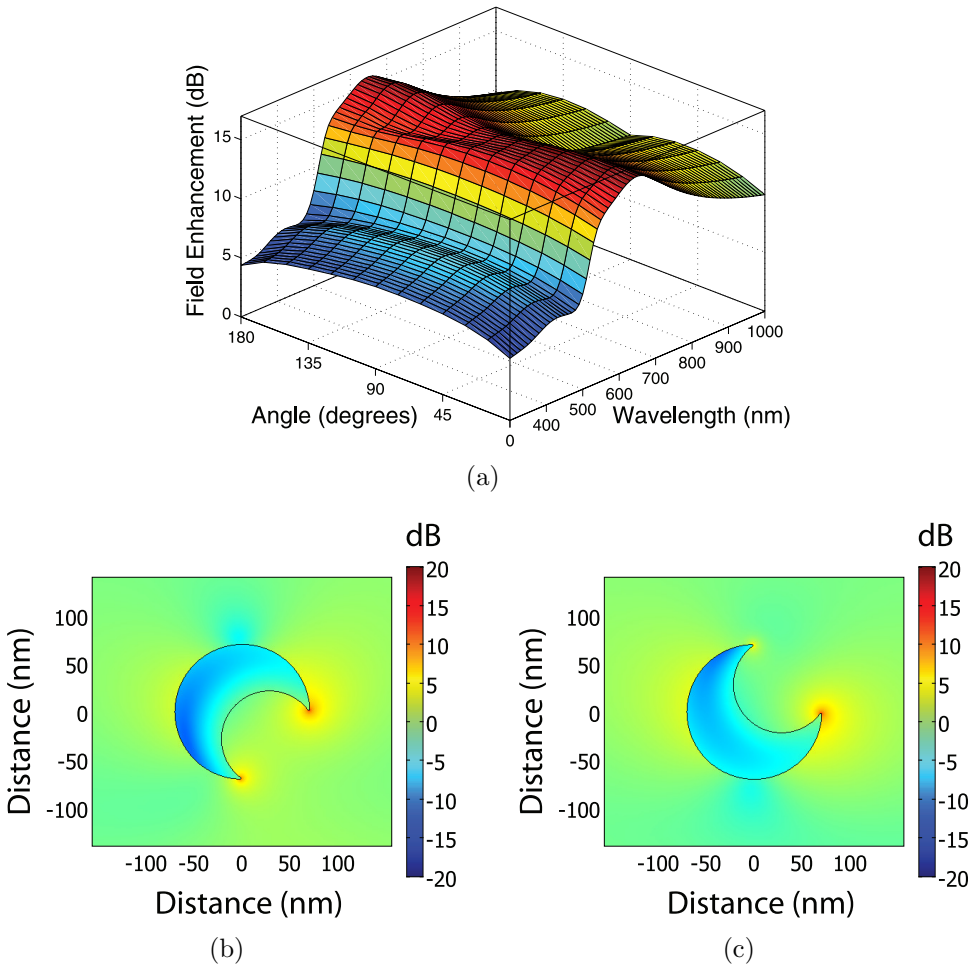

Figure 5.6: (a) Maximum local field enhancement as a function of incident plane wave angle θ and incident free-space wavelength λ_0, (b) field distribution for $\theta = 45°$, $\lambda_0 = 785\,\text{nm}$ and (c) field distribution for $\theta = 135°$, $\lambda_0 = 785\,\text{nm}$ ($r_o = 70\,\text{nm}$, $r_i = 50\,\text{nm}$, $d = 40\,\text{nm}$, $s = 1\,\text{nm}$).

and 5.6c that non-normal incidence induces a significant asymmetry in the local field distribution, caused by the asymmetry of the nanocrescent itself. Such angle dependence is expected from the dipole-like nature of the coupling modes. For example, for $\theta = 90°$, the driving field is perpendicular to the dipole coupling of the tips, so one would expect a reduced enhancement near this regime, as is indeed seen in Figure 5.6.

Finally, the model was adapted to allow consideration of smaller tip-to-tip distances of the nanocrescent as follows: We fixed $r_o = 70\,\text{nm}$, $r_i = 50\,\text{nm}$, and $d = 15\,\text{nm}$, which produces a small circle completely inside of a larger circle. We

then made a rectangular cut (and rounded the edges with a radius of 2 nm) such that the tip-to-tip distance t can be precisely chosen. We then observed the effect of varying t, as shown in Figure 5.7. As t becomes less than 10 nm, strong coupling occurs between the tips and high local field enhancement occurs, concentrated in a small region near the tips. Interestingly, high local field enhancement can also be achieved in the NIR for larger t, and a physically larger region of enhancement occurs near the nanocrescent. This high local field enhancement for two different geometries can be explained by the multiple modes of resonance of the nanocrescent: for close tip-to-tip distances, the lightning rod effect and tip-to-tip coupling result in large field enhancement that is highly localized, while for larger tip-to-tip separations, tip, cavity, and surface coupling result in a physically broader region of field enhancement. This result emphasizes that while decreasing the tip-to-tip distance can increase enhancement for a wide range of wavelengths, resonance at a particular wavelength can be achieved by tuning the remaining geometric parameters.

5.4 Conclusion

In summary, we have observed that plasmon resonance of the nanocrescent is highly tunable: by varying the overall nanocrescent size or by varying the position of the cavity, the plasmon resonance can be brought into the NIR regime. Local field enhancement can be maximized by decreasing the inner radius, and by increasing the sharpness of the tips, and maximum enhancement $|\vec{E}|_{max}/|\vec{E}_i| \approx 100$ (corresponding to 20 dB) for realistic geometric parameters. Varying the angle of incidence can cause splitting of the plasmon resonance peak, and also induces an asymmetry in the local field distribution. Finally, small tip-to-tip distances result in highly localized field enhancement for a broad range of wavelengths, but comparable enhancement for a specific wavelength can also be achieved by tuning the overall structure such that multiple mode resonance occurs.

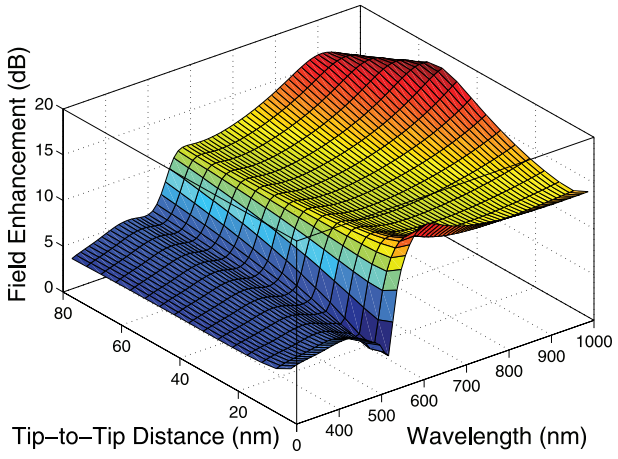

(a)

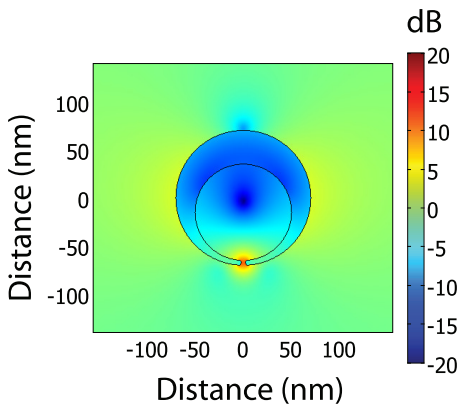

(b)

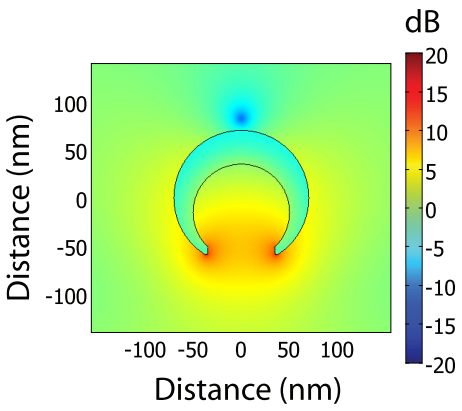

(c)

Figure 5.7: (a) Maximum local field enhancement as a function of tip-to-tip distance and incident free-space wavelength λ_0, (b) field distribution for $t = 5\,\text{nm}$, $\lambda_0 = 1000\,\text{nm}$ and (c) field distribution for $t = 70\,\text{nm}$, $\lambda_0 = 1000\,\text{nm}$ ($r_o = 70\,\text{nm}$, $r_i = 50\,\text{nm}$, $d = 15\,\text{nm}$, $\theta = 0°$).

Chapter 6

Crescent-Shaped Nanohole

6.1 Introduction

Since the discovery of extraordinary transmission of light through subwavelength holes [7], much attention has been devoted to understanding the role of material properties, film thickness, hole geometry, and relative hole placements in the optical response of hole and hole arrays [89, 90]. Recently, it has been shown that such structures may also act as optical antennae–utilizing local surface plasmon resonances (LSPR) of the nanohole structures to focus electromagnetic fields into extremely small regions [91].

Hole-based nanoplasmonic architechtures may offer significant advantages over their "positive structure" counterparts. They can be integrated into optical micro/nanofluid devices, such as the flow-through scheme [92]. Hole architectures may offer robustness, since they are more mechanically stable, and heat can be better dissipated versus nanoparticle structures. In addition, hole structures offer the potential to nanoconfine analyte in hot-spot regions [91, 93].

Hole-based nanoplasmonic sensors have suffered from two problems. Firstly, the hole structures have not achieved the sensitivity of nanoparticle-based approaches (e.g. [94]). This may be largely attributed to limited effort in designing for molecular detection. The optimal hole structures for biomolecular sensing are likely to be different than structures for maximizing transmission, which has been a large focus since the discovery of extraordinary optical transmission. Much as with nanoparticle structure, nanohole sensors should achieve higher sensitivity through coupled architectures.

Secondly, virtually all studies of hole based arrays have been based on slow and expensive "top-down" approaches such as e-beam lithography or focused ion beam (FIB) fabrication. The serial nature of these techniques allows only small regions to be fabricated, and it is both difficult and not cost-effective to integrate such structures into integrated sensing architectures, such as optical microfluidic and nanofluidic

devices. In addition, such top-down techniques typically cannot define feature sizes less than 10 nm, which is a critical limitation in creating ultra-sharp features for plasmonic detection. We note that several methods to develop large-area *circular* hole arrays, such as nanosphere lithography [95], microsphere lenses [96], and soft interference lithography [97] have recently been developed.

In this chapter, we present the first optical study of large-area random arrays of crescent-shaped nanoholes. The crescent-shaped nanohole antennae, fabricated using wafer-scale nanosphere lithography, provide a complement to crescent-shaped nanostructures, called nanocrescents, which have been established as powerful plasmonic biosensors, as discussed in the previous chapter. With both systematic experimental and computational analysis, we characterize the optical properties of crescent-shaped nanohole antennae, and demonstrate tunability of their optical response by varying all key geometric parameters. Crescent-shaped nanoholes have reproducible sub-10 nm tips and are sharper than corresponding nanocrescents, resulting in higher local field enhancement (LFE), which is predicted to be $|\mathbf{E}|/|\mathbf{E}_0| = 1500$. In addition, the crescent-shaped nanohole hole-based geometry offers increased integratability and the potential to nanoconfine analyte in "hot-spot" regions–increasing biomolecular sensitivity and allowing localized nanoscale optical control of biological functions.

6.2 Methods

The process flow of crescent-shaped nanohole fabrication is shown in Figure 6.2. Briefly, a 2 nm thick titanium adhesion layer and a gold layer of defined thickness were deposited onto clean glass slides by e-beam evaporation (Edwards EB3). Random monolayer arrays of polystyrene (PS) spheres (Polysciences) were then deposited on the gold films as follows: PS sphere suspension, 10 mM N-(3-Dimethylaminopropyl)-N'-ethylcarbodiimide (Sigma-Aldrich) solution in PBS (pH 7.4, Gibco), and DI water (Millipore) were mixed at a ratio of 1:0.9:1. The gold surfaces were immersed in the mixture for 1 hour, during which PS spheres were adsorbed to the substrate. Non-adsorbed spheres were washed away with a copious amount of deionized water and the substrates were dried with N_2 gas. The size of the adsorbed PS spheres can be tailored with oxygen plasmon treatment (Plasma-Therm PK-12 RIE, at 50 sccm, 100 W).

The sphere-coated substrates were then etched using vertical angle ion milling (Veeco Microtech System), after which all of the gold is removed except for a nanodisk masked by each PS sphere. A second gold layer was then deposited on the substrate at a defined angle using e-beam evaporation, at a thickness which matched the initial gold layer. The gold can not enter the area shadowed by the PS sphere, and a crescent-shaped void results. Finally, PS spheres were removed using tape (Scotch, 3M) and sonication in acetone for 1 hour. For comparison, we also fabricated nanocrescents

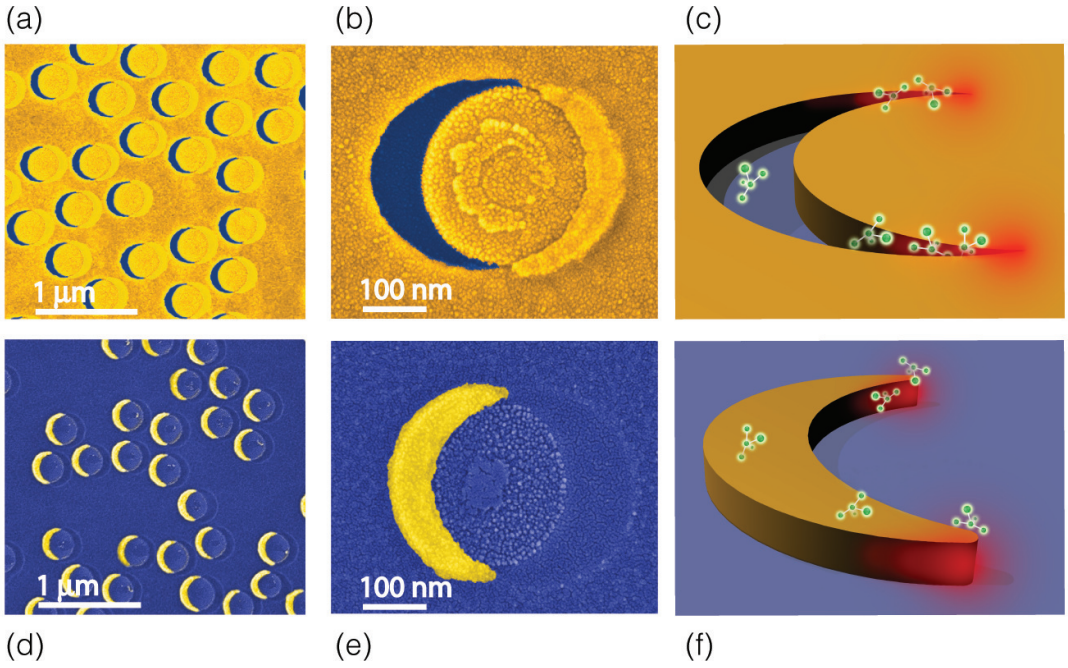

Figure 6.1: Overview of the crescent-shaped nanohole and nanocrescent structures; SEM images (false color) of (a)(d) random arrayed and (b)(e) single structures, and (c)(f) a conceptual illustration of molecular detection for (a)-(c) crescent-shaped nanoholes and (d)-(f) nanocrescents. The crescent-shaped nanohole achieves sharper tips with $< 10\,\text{nm}$ radius of curvature, and is amenable to integrated flow-through architectures for molecular detection.

using a similar PS sphere process as shown in Figure 6.2(e-h) [79]. The resulting crescent-shaped nanohole (as well as nanocrescent) antennae were thus fabricated into large-area random arrays, as shown in Figure 6.1. We used random arrays to isolate the plasmonic characteristics of individual nanostructures from short- and long-range coupling between structures that can result from periodic arrays.

Dark-field scattering microscopy was used to characterize the optical response of crescent-shaped nanoholes and nanocrescents. While transmission measurements are typical for hole studies, the significant absorption and scattering of sharp crescent-shaped nanohole antennae are more appropriately measured via scattering. In our experimental configuration, broadband white light from a halogen source was passed through a dark-field water immersion condenser (NA $= 1.2 \sim 1.4$) to illuminate the sample at an angle larger than the collection angle of the objective lens (NA $= 0.65$). The scattering from the substrate alone was imaged by a CCD camera with spectral resolution better than $2\,\text{nm}$.

To complement the experimental scattering results, we developed a three-dimensional

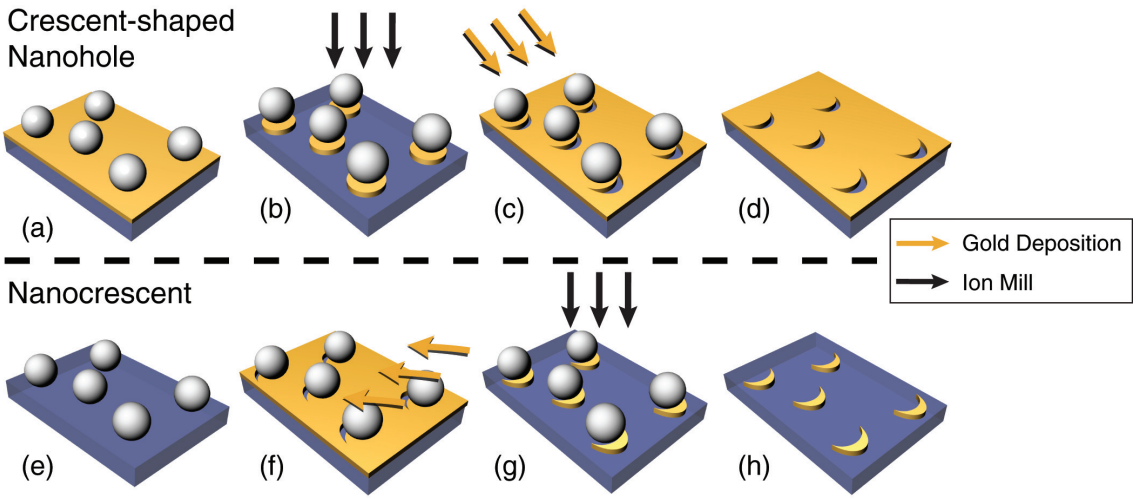

Figure 6.2: Crescent-shaped nanohole and nanocrescent fabrication; nanosphere lithography fabrication process for (a)-(d) crescent-shaped nanoholes and (e)-(h) nanocrescents.

numerical model using the commercial finite element software *COMSOL*. We consider a single crescent-shaped nanohole in a large gold sheet with complex permittivity ϵ given by an analytical model [83] of the experimental data [13] for bulk gold, and with relative permeability $\mu = 1$. The crescent-shaped nanohole shape is approximated by an extruded circle subtracted from an extruded ellipse, where the major and minor axis are determined by the angle of deposition and PS sphere radius, respectively. The surrounding environment is assumed to be vacuum.

Due to the nature of shadow-based nanofabrication, the tips of the crescent-shaped nanohole are extremely sharp–achieving a radius of curvature well under 10 nm without e-beam lithography or FIB. Such dimensions give the crescent-shaped nanohole sharper features than rectangular holes [98], bowtie holes [99], double holes [100], and similar structures which have been fabricated using FIB techniques. Interestingly, the tips are found to be sharper than those of positive nanocrescents fabricated by the same PS sphere template (Fig 6.2(c,g)). We expect this is due to the differences in fabrication between the positive and negative crescents: some unavoidable removal of the PS sphere mask during ion milling of the nanocrescent limits tip sharpness (Figure 6.2(g)), while the crescent-shaped nanohole is defined by gold evaporation through the shadow of the PS nanosphere (Figure 6.2(c)). The increased sharpness causes a higher computed local field enhancement for crescent-shaped nanoholes.

Since it is nearly impossible to completely isolate the positive and negative masking properties of PS spheres during fabrication, a positive nanocrescent typically forms opposite each crescent-shaped nanohole during fabrication, as can be seen in the SEM

images of Figure 6.1(b). However it is clear that this "secondary" nanocrescent does not contribute significantly to the optical signal: dark field scattering measurements were nearly identical when taken on both sides of the films (while the nanocrescent appears on only one side), and experimental results agree well with computational results of pure crescent-shaped nanoholes.

6.3 Results and Discussion

For the application of plasmonic based molecular detection, we particularly wish to study plasmon resonances of the sharp tips of the crescent-shaped nanoholes which occur in the optical regime, hence fitting within the "biological window" of visible and near infrared wavelengths that will not harm biological tissue. For both the crescent-shaped nanohole and its nanocrescent counterpart, in the optical regime the particle plasmon (pp) resonances are dominant, and occur at wavelengths near 600 nm for crescent diameters near 300 nm to 400 nm. Hence, these structures are the focus of this chapter.

The geometric asymmetry of the crescent-shaped nanohole antenna causes a significant polarization dependence, as shown in Figure 6.3. In the case of the crescent-shaped nanohole, the plasmon resonance occurs across the cavity: when the incident electric field polarization is parallel to the long dimension of the crescent-shaped nanohole, denoted pp(c), primarily the tip-cavity modes are excited; when the incident field is perpendicular to the long dimension, denoted pp(u), a resonance across the center of the cavity occurs (Figure 6.3(a-c)). These resonances are mirrored in the nanocrescent (Figure 6.3(d-f)). While the peak positions of the two modes appear almost identical, the pp(u) resonance exhibits a slight redshift compared to the pp(c) mode, and this trend has also been observed in nanocrescents [79]. This supports that the polarization dependence is related to separate resonance modes, while the sharp tips may contribute significantly to the signal in both modes (as is discussed further below).

Since resonances of sharp tips are known to achieve sensitive biomolecular detection, we focus on the pp(c) polarization in the remainder of this chapter, and note that the plasmon band tuning is nearly identical for pp(u) polarization.

Nanosphere lithography offers three primary handles for geometric control: namely sphere diameter d, gold deposition angle θ, and thickness of the gold film h. Understanding the effect of each of these handles is crucial for designing useful devices well as in probing the underlying physics.

We fabricated crescent-shaped nanoholes with a wide range of PS sphere sizes, finding that a strong plasmonic response in the optical regime occurred primarily for PS sphere diameters d near 300 nm, as shown in Figure 6.4. Within the size regime of $d \approx 300$ nm to 400 nm a redshift in the scattering peak occurs with crescent-

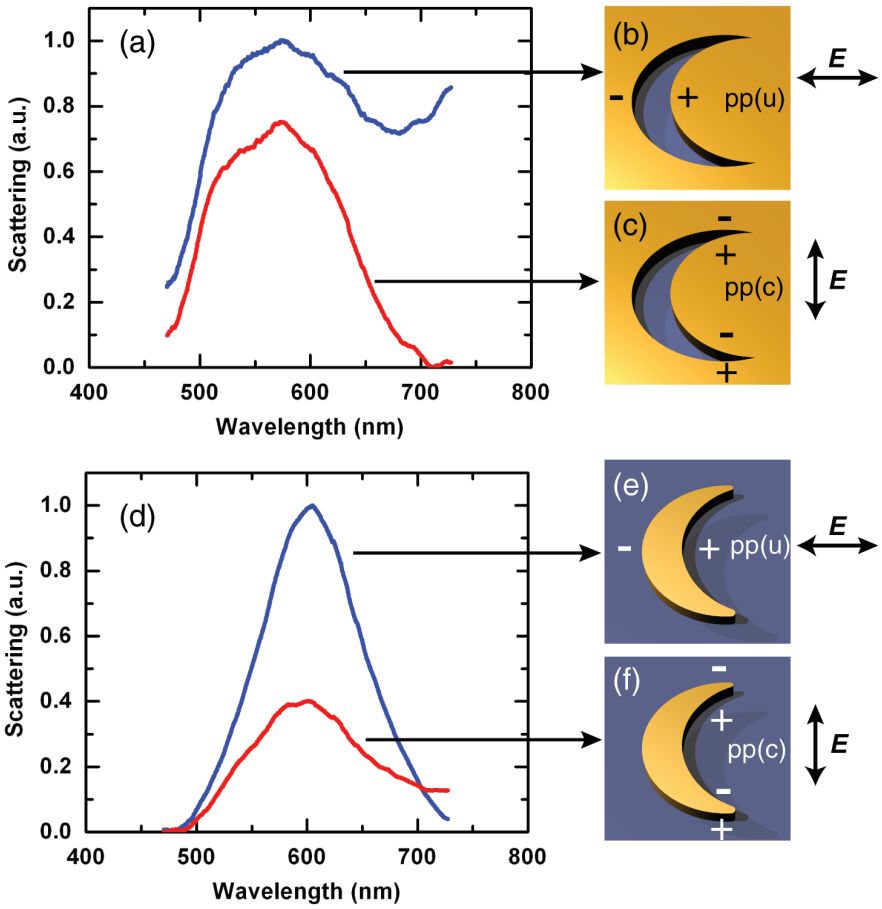

Figure 6.3: Crescent-shaped nanohole polarization dependence; polarization induced resonant modes of (a)-(c) crescent-shaped nanoholes and (d)-(f) nanocrescents. The pp(c) polarization excites the sharp tips useful for molecular detection. The scattering curves are shown for $d = 293\,\text{nm}$, $\theta = 30°$, $h = 25\,\text{nm}$.

shaped nanohole size: for example increasing the sphere diameter from 307 nm to 333 nm results in a 25 nm resonance peak position difference. This behavior has been observed for many different particle and cavity geometries, and is due to radiation damping and retardation [11]. We note the magnitude of redshift agrees well with that seen for nanocrescents [79]. In each case in Figure 6.4, the computed local field enhancement is redshifted roughly 100 nm compared to the experimental results. This difference can likely be explained from oversimplification of the computational model, and real differences between resonances in the near- and far-field. Specifically, the effect of the substrate has been shown to be significant for circular holes [101], and

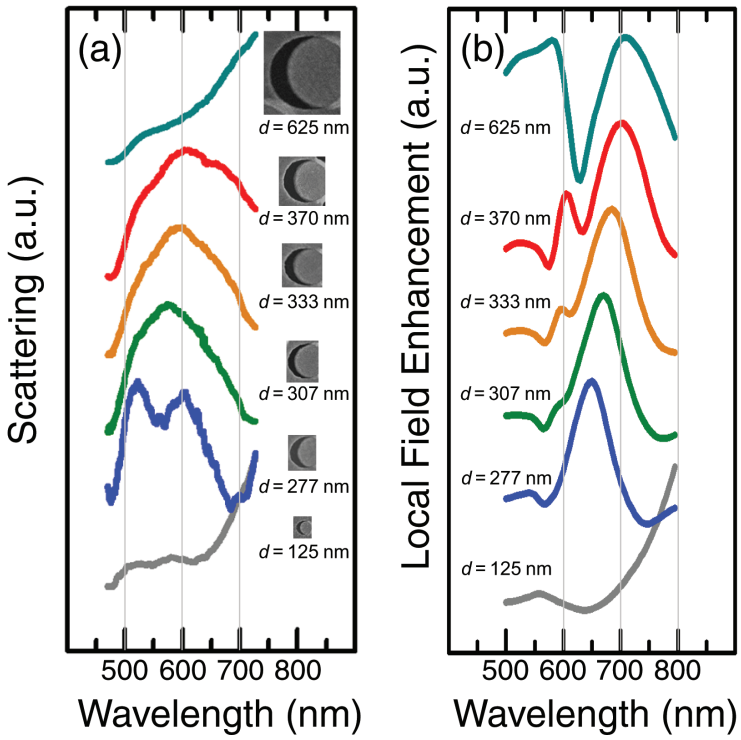

Figure 6.4: The dependence of crescent-shaped nanohole optical response on size; (a) experimental scattering response and (b) computed near-field show a redshift with increasing crescent-shaped nanohole size ($\theta = 30°$, $h = 53\,\text{nm}$, polarization is pp(c))

we suspect the presence of the substrate causes differences between single and double peaks observed in the experimental and computational results. The magnitude of peak change with increasing nanohole size is nearly identical in the experimental and computational results.

Varying the gold deposition angle during crescent-shaped nanohole fabrication allows some control over the nanohole geometry without significantly changing its size, as shown in Figure 6.5. Surprisingly, though the nanohole shape changes significantly as the deposition angle θ ranges from 10° to 45°, the peak scattering position remains nearly unchanged. To understand this result, we computationally investigated the electric field inside the crescent-shaped nanohole. It is clear from the local electric field presented in Figure 6.5(c) that the plasmonic response of the crescent-shaped nanohole is dominated by the sharp tips. Since the tip geometry changes only minimally with deposition angle, little change in plasmon peak wavelength would indeed be expected. Thus, the computational and experimental results are in good agreement.

For a small deposition angle, a thin slit-like crescent-shaped nanohole forms, which

results in increased coupling–and a sharper peak. In the near-field, our computation predicts local fields of $|\mathbf{E}|/|\mathbf{E}_0| = 1500$ (Figure 6.5(c)) at resonance, where this value is taken at least 2 nm from the gold surface. The reduction of this coupling mode with increasing deposition angle causes a broadening of the plasmon peak, as seen in Figure 6.5(d).

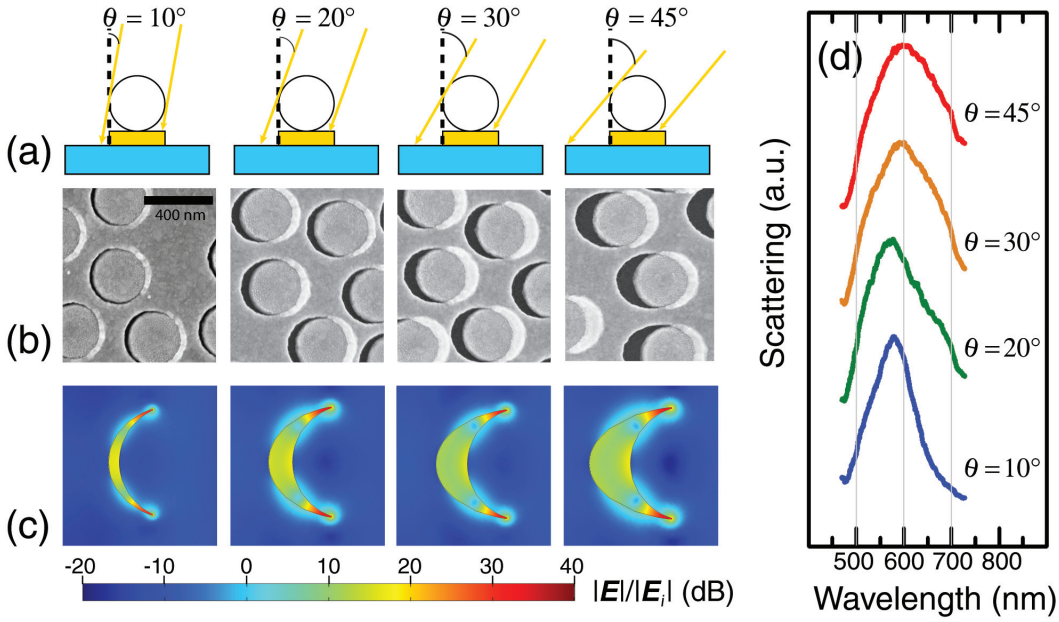

Figure 6.5: The dependence of crescent-shaped nanohole optical response on deposition angle; (a) side view schematic of varying deposition angle, (b) SEM images, (c) computed local electric field enhancement at resonance, and (d) experimental scattering peak for the corresponding crescent-shaped nanohole structures ($d = 333$ nm, $h = 53$ nm, polarization is pp(c)). The sharp tips dominate both the local and far-field response.

We also considered the effect of varying film thickness as shown in Figure 6.6. Since the skin depth thickness of gold is roughly 30 nm at optical frequencies, in varying the film thickness from 13 nm to 65 nm we progress from an optically thin film toward an optically thick film. There is an experimental limitation of the aspect ratio of crescent-shaped nanohole size to height of roughly 4 to 1, since the PS sphere template is also deformed during the ion milling process (etching rate of PS : gold $\approx 1 : 2$). This limitation may be overcome in the future by replacing PS nanospheres with a more resilient material such as silica.

The effect of film thickness on the crescent-shaped nanohole resonance position stresses that the resonance is not purely a 2D effect. Simulation results suggest that at resonance the locally enhanced field progresses completely through the cavity. This is

consistent with observations in holes, where the electromagnetic field is concentrated into a plasmon mode inside the cavity, and is then re-emitted as light on the other side [90]. In the crescent-shaped nanohole structures in this study, we found transmission minima at the resonance wavelength, which is in contrast to transmission enhancement reported in many hole and hole arrays in films much thicker than the skin depth of gold. At the thicknesses below 65 nm used in this study, light that transmits directly through the gold film may destructively interfere with, or become significant in comparison with, the re-emitted light resulting from the plasmon resonance [102]. Similar transmission minima of hole structures have also been reported in hole studies in films of thickness close to the skin depth [103–105].

It is clear in Figure 6.6 that as the film thickness decreases, the scattering peak is redshifted. This follows a general rule seen in many plasmonic structures [11] including holes [104], namely that as the aspect ratio of structure size to height is increased, a redshift in plasmon peak position occurs. This can occur either by increasing the size (Figure 6.4) or by decreasing the height (Figure 6.6) of the nanostructure. We also note that similar shifts are seen in the resonance of positive nanocrescents [79]. Again, experimental and computational results are in good agreement. As the film thickness increases, two distinct peaks in the plasmon band begin to emerge. As shown in Figure 6.6(d), this splitting is caused by a secondary coupling mode on the rounded side of the crescent-shaped nanohole. This splitting is also observed for thin crescent-shaped nanoholes with smaller diameter, as shown in Figure 6.4(a), which indicates that a critical aspect ratio is required for the double peak to emerge.

6.4 Conclusion

It is clear that strong similarities exist between the optical responses of crescent-shaped nanoholes and nanocrescents. While Babinet's principle does not rigorously apply in the regime studied here of finite conductivity and films of finite thickness [12], the similarities presented here between the complementary structures imply that Babinet's principle is at least qualitatively upheld in this nonideal regime. This has also been recently noted in slit ring resonators (SRR's) and their hole complements [106].

Like the positive nanocrescent, the crescent-shaped nanohole can be readily tuned by varying its geometric parameters. However, the crescent-shaped nanohole geometry may offer significant advantages over its positive nanocrescent counterpart. As we have shown, the crescent-shaped nanoholes can be fabricated in large-area arrays with sub-10 nm tips. The tip sharpness exceeds that of positive nanocrescents obtained with the same nanosphere mask, and is sharper than rectangular holes, bowtie holes, and double holes that have been fabricated. Such sharp features will be critical in improving molecular sensitivity of hole-based devices. In addition, the hole geometry

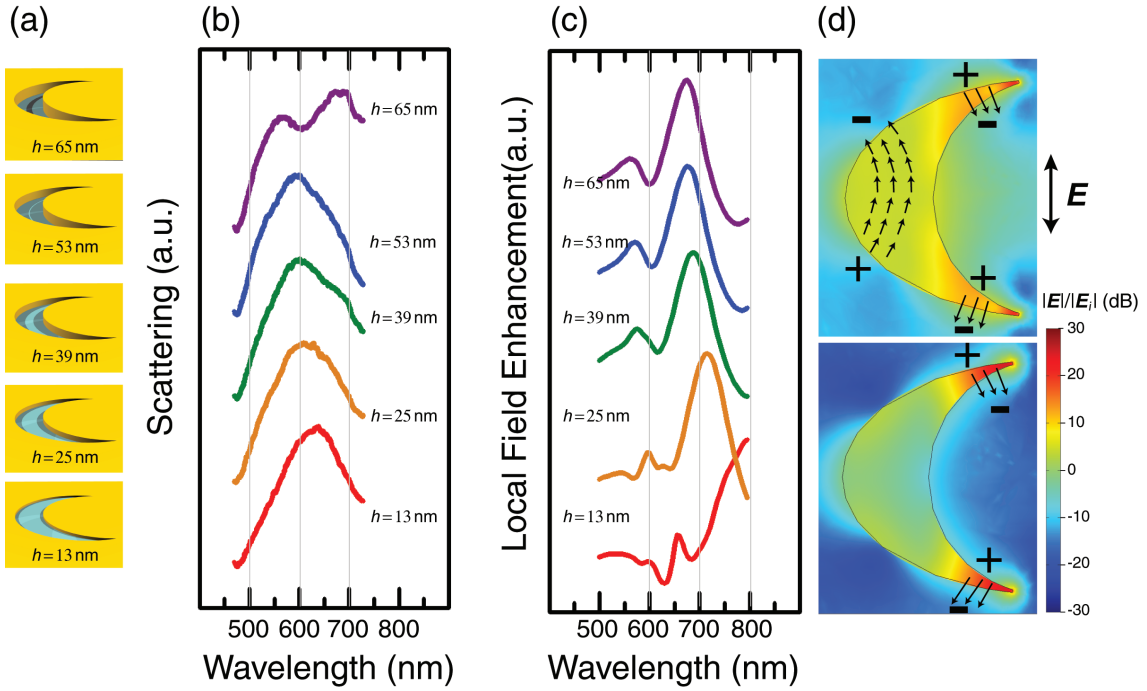

Figure 6.6: The dependence of crescent-shaped nanohole optical response on crescent-shaped nanohole thickness; (a) schematic of varying thicknesses, (b) experimental scattering response and (c) computed near-field and (d) near-field electric field distribution for (top) the secondary peak and (bottom) primary peak shown in part (c) ($d = 333\,\text{nm}$, $\theta = 30°$, polarization is pp(c)). A redshift occurs with decreasing crescent-shaped nanohole thickness, while a second peak emerges for optically thick films.

offers significant advantages over particle-based sensors, including integratability, robustness, and the potential to nanoconfine analyte in hot-spot regions. In short, the crescent-shaped nanohole may provide the best-of-both-worlds between hole-based and particle-based biological and chemical plasmonic sensors.

Chapter 7

Plasmon Enhanced Particle-Cavity (PEP-C)

7.1 Introduction

While recently much attention has been paid to maximizing the local electromagnetic fields surrounding metallic nanoparticles and substrates in the hope of increasing molecular sensitivity [75, 107–112], increasing the density of locally enhanced regions has been generally neglected, and may be at least as important in achieving sensitive and reliable devices. If a molecule is to be detected using such plasmon-based techniques as surface enhanced Raman spectroscopy (SERS) [113], surface enhanced fluorescence [33], local surface plasmon resonance (LSPR) shift [36], or plasmon resonance energy transfer (PRET) [34], then the important question may not be solely the strength of the localized field, but the probability that a molecule will occupy a region of enhancement. If a molecule can be thought analogous to a fish in a lake, then the more hooks, the better the chance of a catch.

A major focus of plasmonic antennae recently has been on particle-particle interactions [114–117] and sharp-tip structures [108, 118, 119]. Such antenna can produce extremely high localized electromagnetic fields (hot-spots), resulting in molecular sensitivities up the level of single molecule detection [94]. However to date, large scale reliable single molecule nanoparticle-based plasmonic detection remains elusive. We suggest two issues have limited progress: i) detection regions are limited to the sparsely (and often randomly) distributed hot-spot regions surrounding antenna and ii) hot-spots are critically dependent on the distance between two points or sharp-tip curvature of a structure, both of which are extremely difficult to control. These issues are intimately tied to fabrication limitations, as even nanometer-sized tolerances can cause large fluctuations in local field intensity, and the most precise fabrication approaches (e.g. electron-beam lithography) are typically not amenable to large-scale

fabrication and cannot generate nanogap features less than 3 nm.

Increasing the density of hot-spots has the potential to achieve both increased sensitivity, because more regions are available to detect molecules, and reliability, since the tolerance of a particular hot-spot becomes less critical for device functionality. However, increasing hot-spot density requires a paradigm shift in the plasmonic architectures that have been proposed. In this chapter, we propose that the plasmonic coupling between a plasmonic nanoparticle and a plasmonic mirror in a structure, which we call a plasmon enhanced particle-cavity (PEP-C), can provide significant increases in both hot-spot intensity and density. In addition, precise control of hot-spot geometry in the PEP-C antenna allows reproducible nanoarchitectures for high device reliability. We note that flat mirror and sandwich structures have been studied recently and shown to be powerful SERS substrates [120–122]; however these studies do not consider complementary geometries (the positive curvature of the particle and the negative curvature of the cavity) between a particle and cavity as studied here.

In this chapter, we propose a coupled nanoplasmonics solution for high hot-spot density creation by coupling a particle and a cavity in a structure dubbed a plasmonic enhanced particle-cavity (PEP-C) antenna. In comparison to analogous particle-based dimer antenna structures, the PEP-C allows both a higher maximum field and an order-of-magnitude higher hot-spot density. In addition, the hot-spots of the PEP-C antenna can be precisely controlled, resulting in increased reliability. We elucidate the photonic characteristics of the PEP-C antenna and show tuning and optimization through choice of geometric parameters. These properties make the PEP-C antenna an excellent candidate for nanoplasmonic-based biomolecular sensors.

We illustrate the PEP-C antenna in Figure 7.1. The structure can be defined geometrically by a particle of radius r, a spacer layer (which may be a dielectric) of thickness d, and an offset h of the particle-cavity centerline from the surface. In this study both the particle and the surface are considered to be gold, but in general either could be replaced with any plasmonic material. Because both cavities and nanoparticles can be made to self-assemble into arrays [123, 124], the PEP-C can be fabricated into large-areas entirely with "bottom-up" techniques and integrated into microfluidic chips, as illustrated in Fig. 7.1(b)-(c).

7.2 Methods

The basic unit of the PEP-C antenna consists of a truncated spherical void in a metallic surface, a spacer layer (which may be a dielectric), and a spherical nanoparticle. The geometry can be described mathematically using the particle radius r, spacer thickness d, and height of the nanoparticle-cavity centerline from the surface h. To create a physically relevant model, the sharp edge of the truncated spherical void is rounded with a 2 nm radius of curvature, and we find that this parameter is not

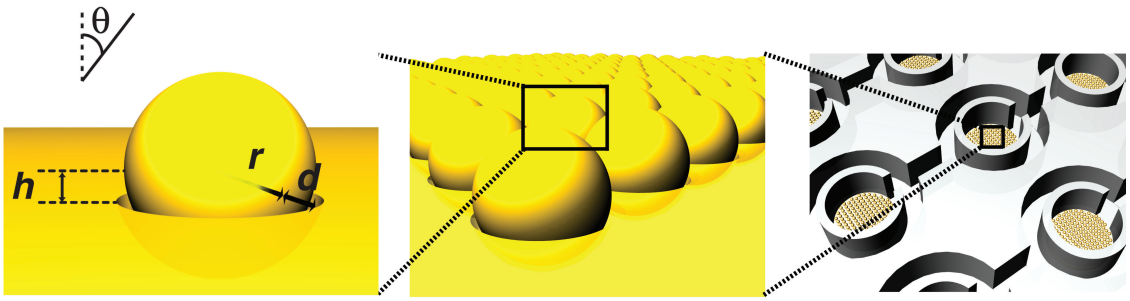

Figure 7.1: A schematic of (a) a single PEP-C antenna with relevant geometric parameters labeled, (b) PEP-C antennae in a self-assembled array, and (c) PEP-C arrays integrated into a microfluidic cell-culture device for biomolecular detection.

critical to the resonant modes and magnitude of local field enhancement.

We consider both the surface and the nanoparticle to be gold, with complex permittivity ϵ given by an analytical model [83] of the experimental data [13] for bulk gold, and with relative permeability $\mu = 1$.

We consider both the surface and the nanoparticle to be gold, with complex permittivity ϵ given by an extension of the Drude model [83]:

$$\epsilon(\lambda) = \epsilon_\infty - \frac{1}{\lambda_p^2(1/\lambda^2 + i/\gamma_p\lambda)} + \sum_{j=1,2} \frac{A_j}{\lambda_j}\left[\frac{e^{i\,\phi_j}}{(1/\lambda_j - 1/\lambda - i/\gamma_j)} + \frac{e^{-i\,\phi_j}}{(1/\lambda_j + 1/\lambda + i/\gamma_j)}\right], \tag{7.1}$$

where $\epsilon_\infty = 1.53$, $\lambda_p = 145$, $\gamma_p = 17000$, $A_1 = 0.94$, $\phi_1 = -\pi/4$, $\lambda_1 = 468$, $\gamma_1 = 2300$, $A_2 = 1.36$, $\phi_2 = -\pi/4$, $\lambda_2 = 331$, and $\gamma_2 = 940$ to fit the experimental data for bulk gold [13]. The relative permeability of gold is assumed to be $\mu = 1$.

The PEP-C structure is assumed to be present in free-space ($\epsilon = \mu = 1$), and for generality the dielectric spacer layer is also assumed to have the properties of free-space. We define a linearly polarized plane wave incident on the structure at angle θ.

The complexity of the PEP-C geometry requires numerical solution, as no known analytic techniques are available. We developed a three-dimensional model using the commercial finite element software *COMSOL*. The software numerically solves over the domain of interest the time-harmonic Maxwell equations, which reduce to the Helmholtz equation [12]. Scattering boundary conditions were used to eliminate nonphysical reflections at the domain boundaries. An adaptive mesh was used, and the mesh was refined until further refinements in element number or size of the domain did not cause changes in the result, verifying a converged model. We also verified our model in the limiting case of a single isolated sphere against the analytic Mie theory [14].

For the results presented below, we compute the surface-average local field enhancement as follows:

$$|\mathbf{E}|_{SA} = \frac{1}{4\pi r^2} \int_S |\mathbf{E}|/|\mathbf{E}_0| dS, \tag{7.2}$$

where S is the surface of the sphere, and herein the incident electric field is assumed to be $|\mathbf{E}_0| = 0$. Since we are motivated by surface enhanced spectroscopies, where molecular interaction occurs in the near field and molecules may attached on any region of the nanoparticle surface, the surface average electric field is the most relevant measure of plasmon resonance.

7.3 Results and Discussion

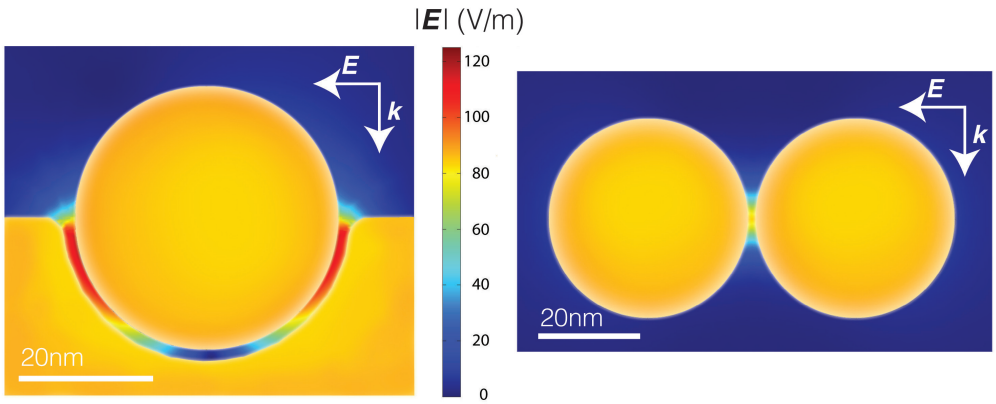

Figure 7.2: A comparison of PEP-C and particle dimer antennae. The computed local electric field amplitude distribution surrounding (a) the PEP-C antenna at resonance and (b) a gold particle dimer of the same nanoparticle size and gap distance at resonance.

The local electromagnetic fields surrounding the PEP-C antenna are significantly different from those in particle-particle or sharp-tip antennae, where high local fields derive from the gap between the closest points of two particles or at sharp tips. Because of the complimentary positive and negative curvature of the particle and cavity, respectively, in the PEP-C structure the plasmonic interaction occurs over a physically extended region, as shown in Fig. 7.2. The gold surfaces of the particle and cavity act as plasmonic mirrors, trapping the light in the curved nanogap region between them. The result is that the hot-spot extends through nearly the entire nanogap, causing the computed surface-average local field enhancement ($|\mathbf{E}|_{SA} = 40$) to be an order of magnitude larger than for gold particle dimers [125]. Since the hot-spot regions are known to determine both LSPR shifts [35] and the enhancement

factor for surface-enhanced spectroscopies such as SERS, the significant increase in hot-spot density should correspond to an increase in molecular sensitivity.

It is important to consider, does an increase in hot-spot density require a concomitant reduction in the maximum local intensity achievable? Ultimately, the total electromagnetic energy distributed throughout hot-spots must be limited by conservation of the incident energy. However, it is clear from Fig. 7.2 that this regime has not yet been reached: the maximum local electric field amplitude $|\mathbf{E}|_{max} = 120$, corresponding to a SERS electromagnetic enhancement of $|\mathbf{E}|^4_{max} > 2 \times 10^8$ (achieved for $\lambda = 700\,\text{nm}$, $r = 20\,\text{nm}$, $d = 2\,\text{nm}$, $h = \theta = 0$), is a 5-fold increase in SERS enhancement compared to a particle dimer with the same particle radius and gap distance at resonance. Thus, the PEP-C is clearly a more efficient antennae, as it can simultaneously attain both a higher maximum field and higher hot-spot density than a particle dimer.

We next consider the tunability of the PEP-C; namely, can the resonances be tuned by varying the geometric parameters? And which parameters are critical for achieving high field enhancement? Tunability is an essential characteristic of any plasmonic architecture designed for molecular detection: firstly, since tuning resonance to the "biological window" is necessary to prevent cellular damage, and secondly, because tuning to the vicinity of specific molecular resonances can create large increases in both SERS [63] and LSPR-shift [64] signals.

As the radius of the particle-cavity system is increased, while keeping a fixed spacer distance, the primary plasmon resonance peak is redshifted significantly (Fig. 7.3(a)). Unlike the redshift observed in isolated nanoparticles, the shift is quite sensitive to particle size, and does not significantly broaden as it is redshifted. Thus, the particle-cavity size presents a simple way to tune the plasmon resonance of the PEP-C into the near infrared (NIR) without a large loss in enhancement or the sharpness of the plasmon peak. The sharpness of the plasmon peak is critical for detecting a LSPR shift upon molecular binding [36].

The primary plasmon peak resonance is dipole-like, with opposite sides of the nanoparticle coupled to the corresponding sides of the cavity, as shown in Fig. 7.2. However, it is clear in Fig. 7.3(a) that as the PEP-C increases in size, multiple peaks emerge as the result of multipole resonance modes. We show schematically in Fig. 7.3(c) the dipole, tripole, and quadrapole resonant modes which cause the primary, secondary, and tertiary peaks, respectively. It is notable that these resonances exist for a relatively small PEP-C size; for example, such resonances would not be seen in an isolated nanoparticle of similar radius. The PEP-C structure thus allows the possibility of tuning to multiple resonances for multiplexed sensing while keeping the structure size small–keeping particle (and hot-spot) density high.

Each resonance peak can be further tuned by varying the thickness of the spacer layer d, as shown in Fig. 7.3(b). Decreasing the spacer causes a redshift in plasmon

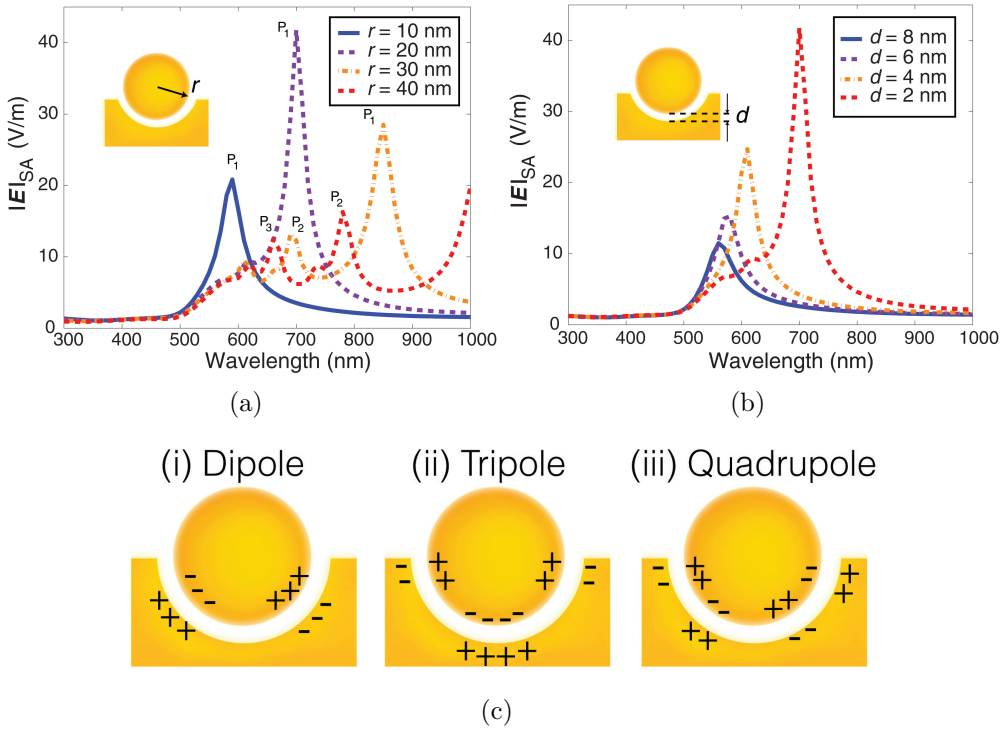

Figure 7.3: The computed surface-average field enhancement surrounding the PEP-C nanoparticle as a function of wavelength for (a) varying particle-cavity radius r ($d = 2\,\text{nm}$, $h = \theta = 0$) and (b) varying spacer thickness d ($r = 20\,\text{nm}$, $h = \theta = 0$); (c) schematic of the (i) dipole ($P = P_1$), (ii) tripole ($P = P_2$), and (iii) quadrupole ($P = P_3$) plasmon resonances, where the values of P correspond to the peaks in part (a).

resonance and significant increase in local field enhancement, analogous to the effect shown in nanoparticle dimer systems [116]. As with nanoparticle dimer and other nanogap systems, the magnitude of the local field enhancement, and hence the effectiveness of the device, depends strongly on controlling the spacer thickness. However, in the PEP-C structure, this spacer layer can be precisely controlled (e.g. by growth of an oxide layer). Furthermore, since the nanogap is not between two points, but two surfaces, there is greater tolerance in the PEP-C structure. As a result, we expect that the reliability of PEP-C antennae should be significantly higher than other plasmonic nanogap structures.

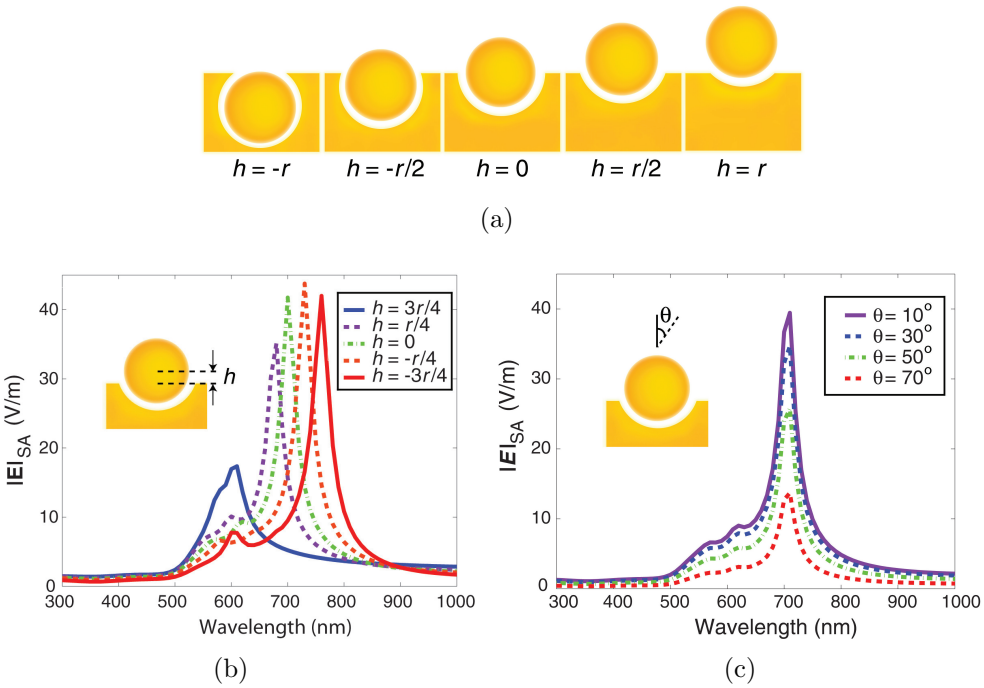

Figure 7.4: (a) Schematic of the PEP-C antenna as the height of the particle-cavity centerline is varied; (b) the computed surface-average field enhancement surrounding the nanoparticle as a function of wavelength for varying particle-cavity height h ($r = 20\,\text{nm}$, $d = 2\,\text{nm}$, $\theta = 0$) and (c) varying incident angle θ ($r = 20\,\text{nm}$, $d = 2\,\text{nm}$, $h = 0$).

Each resonance is also affected by the location of the height of the particle-cavity centerline from the surface, with a redshift occurring as the centerline is lowered beneath the surface, as shown in Fig. 7.4(b). For the limiting case of the particle-cavity centerline above the surface with a distance $h > r$ the cavity vanishes, resulting in a particle above a flat surface. In this case the particle and surface are only weakly coupled, and the plasmon resonance is dominated by the particle resonance, which for

gold is between $500-600$ nm for small particles. The plasmon peak indeed approaches this value for $h = 3r/4$ in Fig. 7.4(b). As the particle-centerline is lowered beneath the surface, increased coupling between the particle and cavity causes a redshift in the plasmon peak and significant increase in the local field enhancement. However, the surface begins to prevent effective transfer of light into the coupled mode. In the limiting case, light would be completely reflected for a particle-cavity far below the surface. Hence, the optimal enhancement occurs for the centerline of the particle-cavity near the plane of the surface, in the regime $0 < h < -3r/4$.

Finally, we investigated the effect of varying the angle of incidence, as shown in Fig. 7.4(c). We find that the local field enhancement systematically decreases as the incident angle is brought away from the normal. Because of its symmetry, the resonance of the spherical nanoparticle should have little dependence on the angle of incidence, but for the truncated cavity this is not the case. Indeed, it has been shown both experimentally and computationally that the strongest resonances of truncated spherical nanocavities occur for normal incidence [126]. We note that normal incidence remains the optimal condition for PEP-C structures with $h \neq 0$ as well.

7.4 Conclusion

We have introduced and optimized the PEP-C structure as a tunable plasmonic antenna. Because of its complementary geometry, PEP-C can achieve both higher maximum local field ($|\mathbf{E}|_{max} = 120$) and an order of magnitude higher hot-spot density ($|\mathbf{E}|_{SA} = 40$) than comparable particle dimer structures. Furthermore, precise control of hot-spot geometry in the PEP-C antenna allows for high device reliability. We have elucidated the multipole resonances of PEP-C, shown plasmon band tuning across the visible and near-infrared spectrum, and shown optimization of the structure through choice of geometric parameters. We believe PEP-C antennae can provide a significant step toward label-free sensitive and selective plasmonic sensors.

Chapter 8

Core Satellite Biosensors

8.1 Introduction

In this chapter we focus on a coupled system comprising coupled metal nanoparticles, also known as nanoclusters or nanoassemblies. Coupled noble metal nanoclusters have localized surface plasmon resonances (LSPR) in the visible spectrum that are highly dependent upon the overall construct geometry, interparticle distance, and the dielectric permittivity of the surrounding medium. Variations of nanoassemblies have included lattice networks [127, 128], dimer and trimer configurations [129, 130], and core-satellite constructs [115, 130–132]. These nanoassemblies have enabled investigations of plasmon coupling [133, 134] and plasmon-based detection of biological and chemical analytes [24, 135, 136].

Our particular focus is on core-satellite nanoparticle systems, which are made up of a central core nanoparticle attached to multiple satellite nanoparticles. While core-satellite nanoassemblies are a promising platform for plasmon-based detection, basic questions remain on how to maximize their sensitivity. For example, will many small satellite nanoparticles produce a larger shift-upon-attachment (or release) than a few large ones? What is the importance of the core particle size? What is the optimal core-satellite linker distance? These questions are critical for the next generation of sensors, since optimization of core-satellite scattering spectra will maximize the signal-to-noise ratio during spectroscopic sensing, enabling simple colorimetric assays and improving sensitivity. In addition, the core-satellite system serves as a platform to understand the fundamentals of plasmon coupling in nanoassemblies. We illustrate the core-satellite nanoassembly in Figure 8.1.

In this chapter we present a systematic theoretical study of core-satellite gold nanoparticle assemblies using the Generalized Multiparticle Mie formalism. We consider the importance of satellite number, satellite radius, the core radius, and the satellite distance, and we present approaches to optimize spectral shift due to satel-

lite attachment or release. This provides clear strategies for improving the sensitivity and signal-to-noise ratio for molecular detection, enabling simple colorimetric assays. We quantify the performance of these strategies by introducing a figure of merit. In addition, we provide an improved understanding of the nanoplasmonic interactions that govern the optical response of core-satellite nanoassemblies. While theoretical results for cluster assemblies have been reported [133, 137, 138], this work represents the first systematic study of the core-satellite nanoplasmonic system.

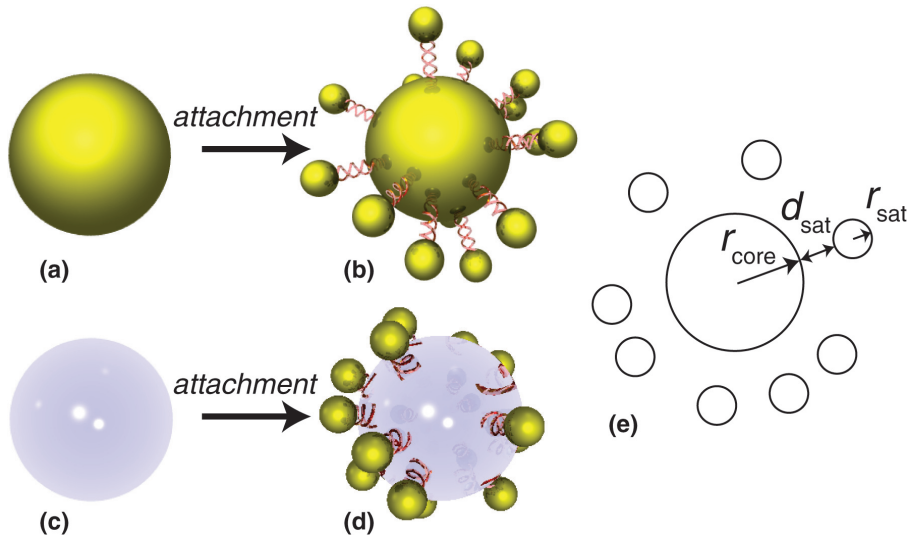

Figure 8.1: The core-satellite nanoassembly; (a) gold core nanoparticle with (b) gold satellites attached via a molecular linker to form a core-satellite nanoassembly; (c,d) alternatively, gold satellites may attach to a glass core nanoparticle; (e) a schematic of the core-satellite system with the key geometric parameters labeled.

8.2 Model

The exact solution of electromagnetic scattering by a single sphere was solved by Gustav Mie over 100 years ago [2, 14], but only recently has this technique been extended to the case of multiple spheres at arbitrary distances, with the Generalized Multiparticle Mie (GMM) solution [16–20]. Using this exact solution, we compute the scattering cross section of core-satellite nanoparticle assemblies. We assume both the core and satellites are made of gold, with complex permittivity ϵ given by an analytical model [43] of the experimental data [13] for bulk gold, and with relative permeability $\mu = 1$. The surrounding medium is assumed to be free-space with $\epsilon = \mu = 1$. For comparison, we also consider glass core nanoparticles, with $\epsilon = 2.25$.

To model the stochastic nature of satellite positions around the core, satellites were successively placed around the core at a fixed radius using a random number generator, until the desired number of satellites was reached. For all spectra shown in this chapter, 10 such random core-satellite assemblies were generated, and the scattering results were averaged to give more physically relevant results, and to avoid trends due to symmetric placement of satellites. Even for nanoassemblies with defined satellite placement [128], nanoassemblies are typically at random orientations relative to the polarization of the incident light; hence a stochastic model is relevant to a wide range of physical systems.

8.3 Results and Discussion

Four primary handles exist to potentially vary the optical properties, and most importantly the shift-upon-attachment (or release), of the core-satellite system: the satellite number n_{sat}, the satellite radius r_{sat}, the core radius r_{core}, and the satellite distance d_{sat} (Figure 8.1). Herein we demonstrate the importance of each of these parameters. We focus on shift-upon-attachment; defined as the difference in the LSPR wavelength between the entire core-satellite assembly and that of the single core particle: $\Delta\lambda = \lambda_{\text{peak,core+sat}} - \lambda_{\text{peak,core}}$. This shift is identical (but opposite in sign) for shift-upon-release of satellites.

As satellite number increases, a nearly linear redshift occurs in the scattering spectrum, as shown in Figure 8.2(a-b). For the physically relevant parameters chosen ($r_{\text{core}} = 50$nm, $r_{\text{sat}} = 10$nm, and $d_{\text{sat}} = 2$nm), this redshift is roughly 1nm per satellite; hence a 50 nm redshift is achievable by nearly maximizing coverage of satellites, and these peak shifts are similar to that seen in comparable experimental systems [133]. The redshift upon satellite attachment is caused by the local plasmonic coupling between the core and satellite nanoparticles. In this case, since both the core and satellite sizes are much smaller than the incident wavelength of light, the quasi-static approximation is valid, and the interaction can be closely modeled by coupled dipoles. We note that the plasmon bandwidth decreases with increasing satellite number, and this effect is also due to the local plasmonic coupling, while the small particle size prevents damping effects from broadening the plasmon bandwidth. Since a glass core with 60 gold nanoparticle satellites shows only a broad peak near 550 nm (dashed line in Figure 8.2(a)), it is clear that both the plasmon shift and bandwidth narrowing are due primarily to core-satellite interactions and not satellite-satellite interactions. Both the peak shift and the plasmon bandwidth are important in the figure of merit (FOM) for detecting plasmonic peak shifts [37]. To take into account both of these effects, for core-satellite systems we define FOM = $\Delta\lambda$/FWHM, where FWHM is the full width at half maximum of the plasmon band. For 60 satellite nanoparticles, the figure of merit FOM = 0.64

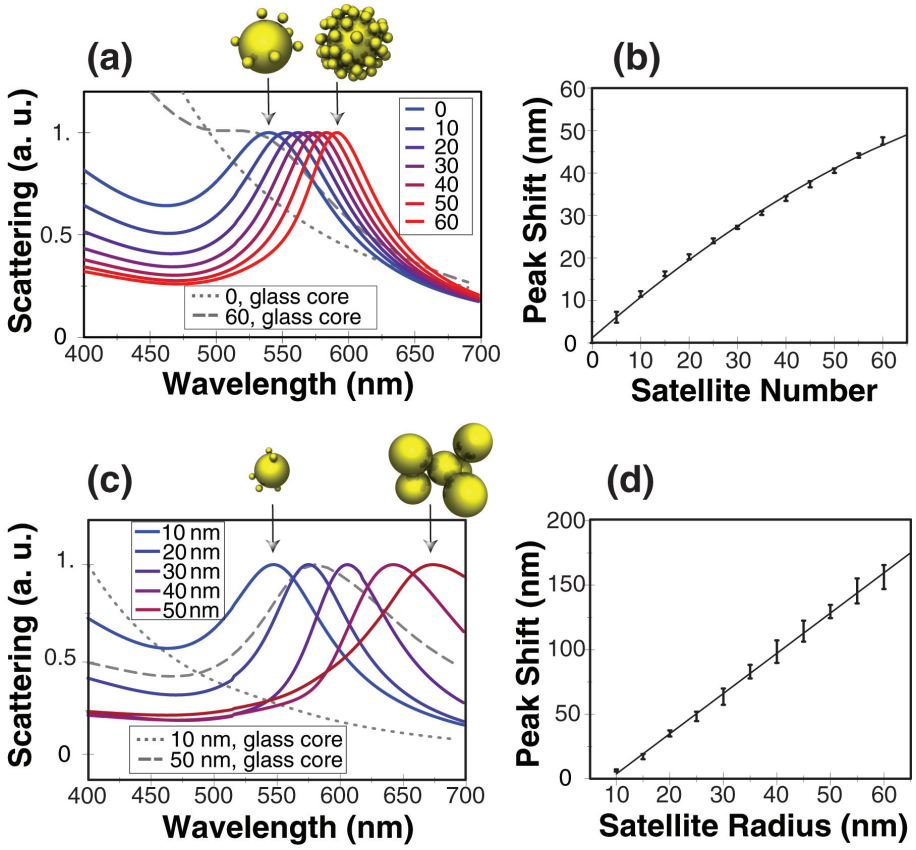

Figure 8.2: Effect of varying satellite number and size; normalized scattering cross section of core-satellite nanoassemblies for (a) increasing satellite number ($r_{\text{core}} = 50$ nm, $r_{\text{sat}} = 10$ nm, $d_{\text{sat}} = 2$ nm) and (c) increasing satellite radius ($r_{\text{core}} = 50$ nm, $n_{\text{sat}} = 5$ nm, $d_{\text{sat}} = 2$ nm); the peak shift $\Delta\lambda$ for increasing (b) satellite number and (d) satellite radius; solid line shown as a guide, error bars represent standard deviation from 10 randomly generated core-satellite assemblies.

While increasing satellite number presents one strategy for maximizing shift-upon-attachment, increasing the satellite size presents another scheme, as shown in Figure 8.2(c-d). In varying the satellite radius from 10 to 50 nm, a 150 nm redshift is seen in the plasmon band. This relationship is also nearly linear, with a 3 nm redshift per 1 nm increase in satellite radius. As the satellite radius increases past 50 nm, the plasmon band broadens significantly. This is mainly due to retardation effects as the nanoassembly size becomes significant compared to the wavelength of light. Radiation damping, which depends on particle volume, has been shown to be largely responsible for redshifts in both near- and far-fields scattered from nanoparticles as they increase in size (as shown in Chapter 2). Therefore, compared to the "many

small satellite" approach, the "few large satellites" approach takes advantage of the increases in redshift due to the nanoassembly size becoming large compared to the wavelength of incident light. As Figure 8.2 shows, the latter approach can generate much larger peak shifts. Hence, increasing satellite size presents a method of creating larger shift-upon-attachment versus using many smaller satellites. We believe this approach has been greatly under-utilized in the literature–the figure of merit for five 60 nm satellites reaches FOM = 1.52, over twice that of the "many small satellite" approach.

We note that the spectra of nanoassemblies with few satellites show wider variation due to the stochastic nature of satellite placement. For example, with only a handful of satellites, there is a greater chance they may be placed out of the plane of the incident electric field and only weakly couple to the core nanoparticle. In contrast, for large satellite numbers, the variation between assemblies is reduced, as shown in the standard deviation in peak shift in Figure 8.2(b) versus Figure 8.2(d). The physical importance of this phenomenon may also depend on the mechanism of satellite attachment. We also note that again both the plasmon shift and bandwidth properties are due primarily to core-satellite interactions, since a broad peak near 575 nm is observed for $r_{\text{sat}} = 50$ nm gold satellites and a glass core (dashed line in Figure 8.2(c)). Next, we consider the effect of the core size in Figure 8.3(a). Again, retardation effects occur as the core radius increases, broadening the spectral peak, and the peak shift decreases with increasing core size. This result is consistent with that shown for increasing satellite size–if we consider the ratio of the satellite size to the core size, in both Fig. 8.2(c-d) and Figure 8.3(a-b), an increasing ratio causes an increased peak difference upon attachment. The relationship between peak shift and core sphere size is approximately linear in the quasi-static regime (core radius < 50 nm), while the relationship becomes nonlinear for larger core sizes as damping effects become significant, and the peak shift becomes small (Figure 8.3(b)). In contrast, without the core-satellite coupling, the plasmon peak is blueshifted for a class core (Figure 8.3(a)), and for large glass cores a broad peak emerges near 450 nm due to the glass. These results might lead one to conclude that minimizing the core size is a desirable route to increasing peak shift. While this is correct, it is limited by practical concerns: nanoparticle absorption scales with the particle volume, while scattering scales with the volume squared. Thus, smaller particles become difficult to observe, and the absorption signal will become large compared to the scattered signal. In addition, the reduced surface area for smaller particles limits the number of satellites that can be attached. Thus, for scattering detection schemes, a minimum core radius of $r_{\text{core}} \approx 25$ nm is desirable.

Finally, we consider the importance of the distance between the core and satellite particles, typically determined experimentally by a chemical linker, such as an oligonucleotide. As shown in Figure 8.3(c-d), decreases in core-satellite distance cause

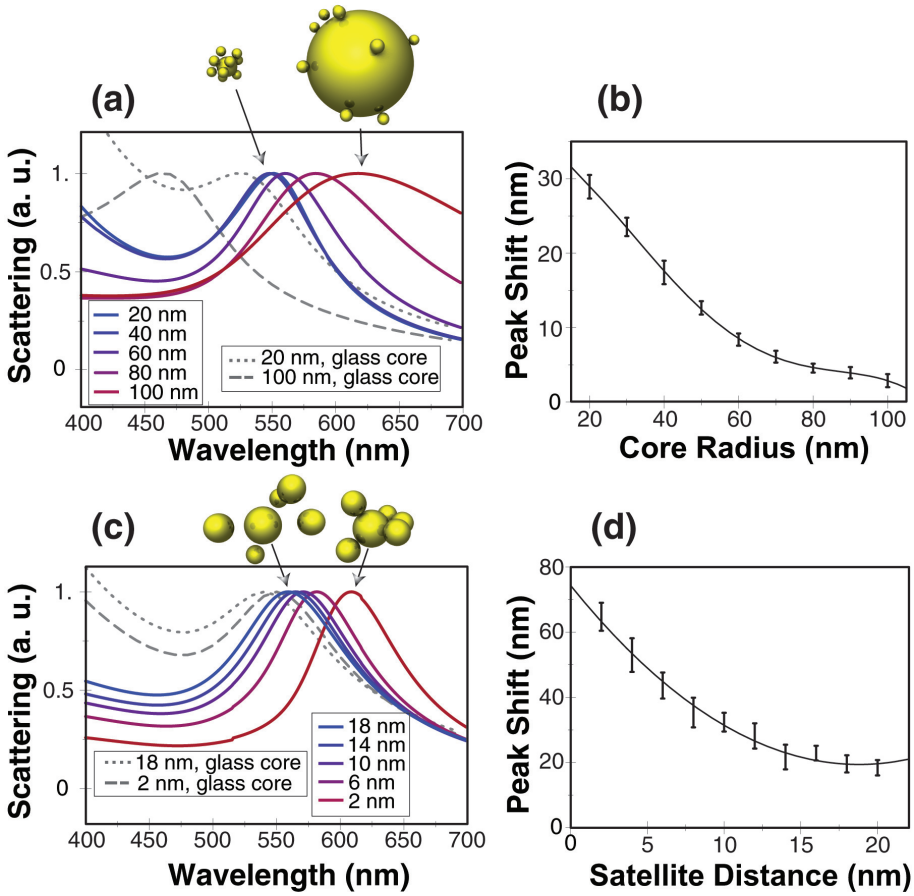

Figure 8.3: Effect of varying core size and satellite distance; normalized scattering cross section of core-satellite systems for (a) increasing core radius ($r_{\text{sat}} = 10$ nm, $n_{\text{sat}} = 10$, $d_{\text{sat}} = 2$nm) and (c) increasing satellite distance ($r_{\text{core}} = 50$nm, $r_{\text{sat}} = 30$nm, $n_{\text{sat}} = 5$nm); the peak shift $\Delta\lambda$ for increasing (b) core radius and (d) satellite distance; solid line shown as a guide, error bars represent standard deviation from 10 randomly generated core-satellite assemblies.

an increase in the redshift in a nonlinear fashion. To take advantage of this nonlinearity, particularly close core-satellite distances (< 5nm) are desirable. This nonlinearity is due to the rapidly decaying near field, determined by distance^{-3} in the quasi-static approximation, and typical decay lengths are tens of nanometers. This gap-dependent redshift behavior has been observed and predicted in many different systems, for example molecular rulers [134] and particle dimer systems [116]. With a glass core, only a minimal redshift occurs when the satellite distance decreases; hence core-satellite interactions again dominate the satellite distance dependence. We note that the assumptions of classical electromagnetics are no longer physically valid when the gap

size is less than ≈ 2 nm; hence this was the smallest gap distance used in this study.

We believe the strategies described here are achievable with current fabrication techniques. Core-satellite architectures of noble metal and silica nanoparticles have been demonstrated primarily using directional conjugation methods, specifically, by combining complementary motifs that tether nanoparticles to a linking agent, such as a modified oligonucleotide functionalized with a high affinity biomolecule. Directional assembly commonly exploits binding motifs such as mercaptan/metal [104, 115, 128, 131, 134], biotin/streptavidin [104, 134], antibody/antigen [139], digoxingenin/anti-digoxigenin [134], and cyclic disulfide phosphoramidite moiety/Ag [140] bonds. The directional hybridization of half complementary, modified oligonucleotides further extends directional arrangement of nanoassembled constructs [104, 131]. Additionally, 2-dimensional analogues of the 3-dimensional core-satellite structures could conceivably be fabricated using top-down methods such as photo, nanoimprint, electron beam, focused ion beam, or soft lithographies.

8.4 Conclusion

To conclude this chapter, we have demonstrated simple strategies for improving shift-upon-attachment or shift-upon-release for core-satellite systems. While increasing satellite number produces a near linear redshift reaching ≈ 50 nm, a larger shift (≈ 150 nm) can be achieved by increasing satellite size in the same system. Core size should be minimized, constrained by the minimum size required for detection of the core scattering signal. Linker distances should be minimized to improve core-satellite coupling, which scales nonlinearly with distance. By taking these simple strategies into account, more sensitive and higher shift-upon-attachment core-satellite nanoplasmonic sensors are achievable.

8.5 Coupled Nanoplasmonic Antennas Conclusions

In Chapter 5-8 , four distinct coupled nanoplasmonic architectures were investigated. In each case, we started with a general concept of the system, introduced its potential advantages over other systems, and systematically investigated the effect of each geometric parameter that makes up the system. Each system has its own advantages and disadvantages to other systems, and more than simply the maximum local field enhancement must be considered. For example, the nanocrescent is able to achieve reasonably high field enhancements without interparticle coupling, thus is well-suited to *in-vivo* applications. The crescent-shaped nanoholes offer the possibility of flow-through applications, which offers potential advantages over the traditional flow-over techniques. PEP-C architectures offer not only a high field enhancement, but also an

extremely high density of hot-spots. Core-satellite systems offer a unique switching modality between a red and blue state when satellites are attached or detached.

The primary disadvantages of coupled architectures, vs traditional spheres or rods, are their complexity and fabrication. As shown in this chapter, the resonance of coupled structures is often closely dependent on the system geometry. While this allows tuning of the resonance over a wide range of wavelengths, the complexity of the geometry-resonance relationship makes it difficult to design a structure to match a particular resonance. The studies presented in this chapter have helped elucidate these dependences. The fabrication of these structures, with the exception of core-satellite systems, typically involves at least one top-down fabrication step (e.g. evaporation). In contrast, spherical or rod-like nanoparticles can be fabricated entirely with solution-based methods.

Chapter 9

Nanocorals: Bio-Inspired Multi-Functional Cellular Probes

"To wear your heart on your sleeve isn't a very good plan; you should wear it inside, where it functions best."

Margaret Thatcher

9.1 Introduction

We concluded Chapter 8 by noting that each system may have its own advantages and disadvantages depending on the way it is intended to be used. The specific case of molecular sensing inside (and on the surface of) a living cell is a particularly demanding application, and many issues must be considered. This chapter focuses entirely on this topic. We introduce a special class of bioinspired nanoplasmonic structures called nanocorals, designed for molecular sensing within or on the surface of living cells. Nanocorals are unique in that they combine cellular specific targeting with biomolecular sensing, yet decouple the two functional modes. Analogous to natural sea corals that use rough surfaces to maximize surface area for efficient capture of light and food particles, nanocorals utilize a highly roughened surface at the nanoscale to increase analyte adsorption capacity, and create a high density of surface-enhanced Raman spectroscopy (SERS) hot-spots.

The ability to sense and detect local biological information inside a living cell may lead to a revolutionary improvement in diagnostic accuracy and therapeutic strategy [141, 142], wherein the molecular components or processes that represent detailed mechanisms of pathologies and treatment responses can be directly investigated. Hence, there is a strong driving force to engineer small probes, ranging from tens to hundreds of nanometers in size, that can be positioned in specified regions inside or surrounding living cells in order to facilitate molecular detection. Most nanoprobes developed for this purpose serve as labels or markers that bind to and report the presence of specific molecules, and their read-out signals are based on the intrinsic properties of the probe, such as the emission of quantum dots or the scattering of metal nanoparticles [143–146]. In contrast, nanoprobes that enhance molecular spectral information, such as surface-enhanced Raman spectroscopy (SERS), are promising since the read out signal is intrinsic to the *molecule*. This molecular fingerprint offers the potential for label-free multi-channel read out of local biochemical composition [30–32].

A key technology in achieving useful cellular nanoprobes is the attachment of ligands to their surface to allow targeting to specific cell types or subcellular regions. While targeted drug delivery, photothermal therapy, and MRI contrast enhancement have been demonstrated and have large potential for clinical diagnosis and treatment, nanoprobes which can achieve both targeting and SERS have not yet been reported. Achieving both targeting and SERS in a single nanoprobe is challenging because targeting ligands attached on the surface will impede the SERS detection. Therefore, part of the nanoprobe surface must be kept ligand-free to allow direct SERS measurement, or alternatively for conjugation with a different ligand to bind molecules of interest.

In contrast to other SERS cellular nanoprobes, such as nanoshells [12] and nanocre-

scents [115] composed purely of gold, the PS hemisphere of the nanocoral can be selectively functionalized with antibodies to target the receptors of specific cells. This functionalization leaves the roughened gold region of the nanocoral clean for SERS measurements. Therefore, the targeting and sensing mechanisms are decoupled, and can be separately engineered for a particular experiment. In addition, the PS region may also be used as a carrier for drugs or other input chemicals by surface hydrophobic adsorption [147] or encapsulation [148], making the nanocoral a multifunctional nanosensor (Figure 9.1).

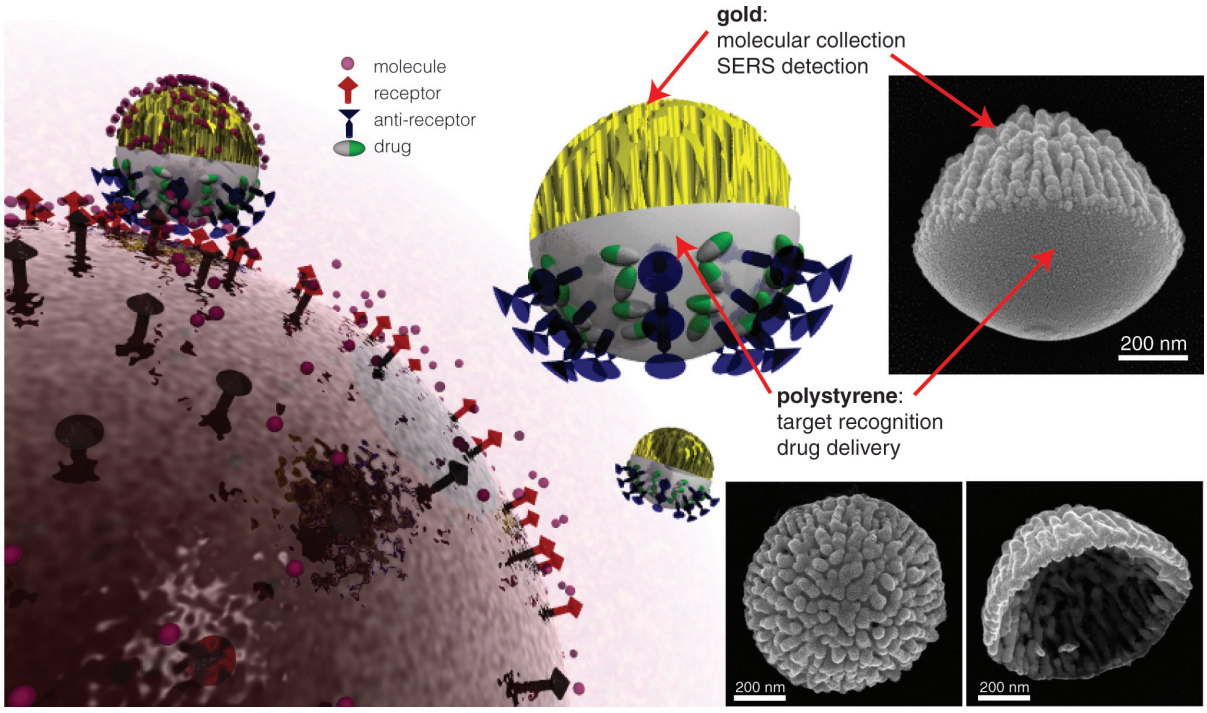

Figure 9.1: Schematic of nanocorals as multifunctional nanoprobes for targeting, sensing and drug delivery; insets show SEM images of fabricated nanocoral probes; the PS template has been etched in the bottom right inset.

9.2 Methods

The fabrication of the nanocoral array is a simple and cost-effective 3-step process, as illustrated in Figure 9.2. The process starts with the formation of a hexagonal close-packed monolayer of PS nanospheres on a glass substrate by a drop-cast method [149]. The substrate is then loaded into an oxygen plasma etching system (Plasma-Therm PK-12, at 50 sccm, 100 W), and the etching time is adjusted based on the original

PS nanosphere size. For example, the PS nanospheres in Figure 9.1 were etched for 100 seconds to generate nanocorals that were 800 nm in diameter. The plasma etching induces shrinkage of the PS nanospheres as well as deeper trenches on the surface with longer etch times. Gold is then deposited on the PS template (Edwards e-beam evaporator EB3) to obtain a specific thickness, and the resulting nanocoral array can be directly used for SERS measurements. To achieve stand-alone probes, the nanocoral array is immersed in deionized water and sonicated for 5 mins, after which all nanocorals are released from the surface and suspended in solution (Figure 9.2(d)).

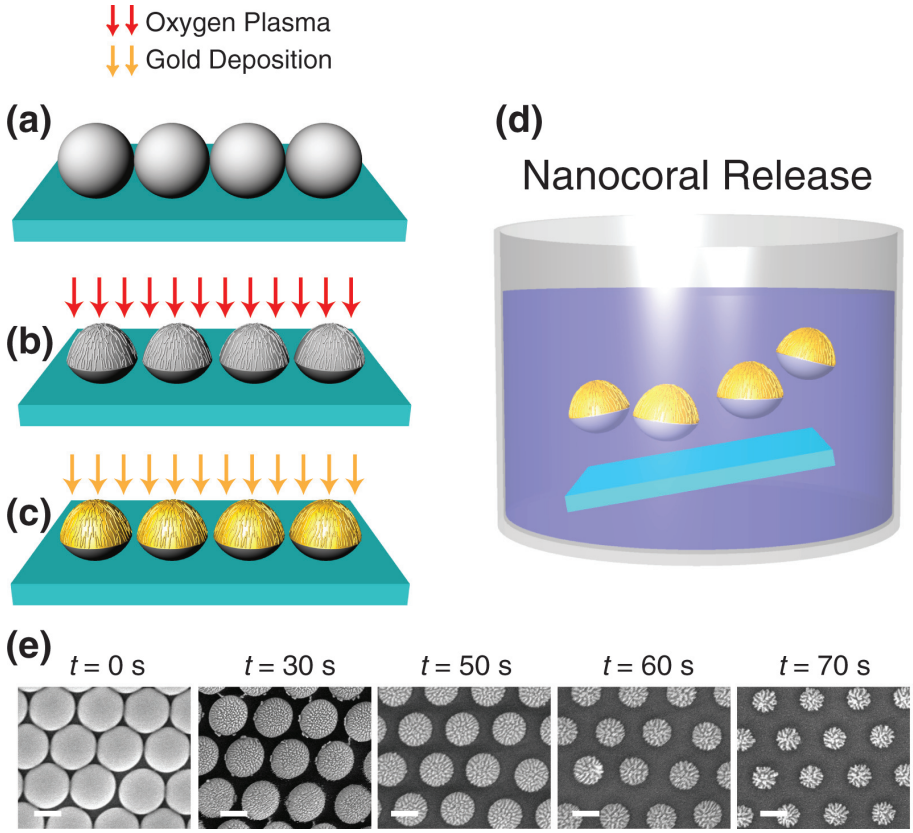

Figure 9.2: Nanocoral fabrication process; (a) self-assembly of PS nanospheres on glass, (b) oxygen plasma etching, (c) gold deposition and (d) release of nanocorals into solution; (e) the gradual etching of the PS template to create the nanocoral template (scale bar = 200 nm)

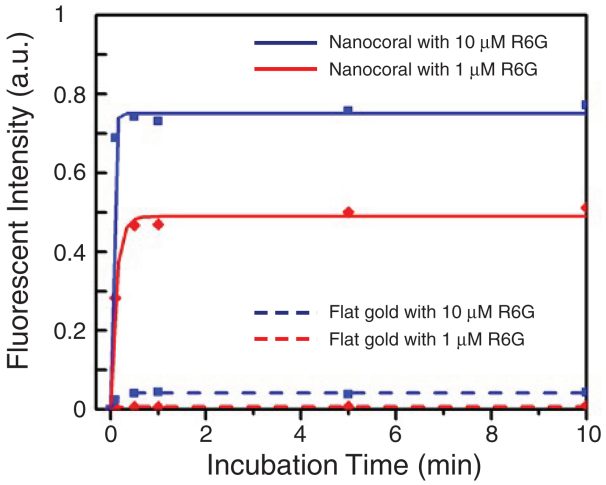

Figure 9.3: R6G molecular adsorption on nanocoral array; by incubating nanocoral arrays and flat gold substrates with 1 μM and 10 μM R6G solution, followed by water cleaning and nitrogen drying, we compared the fluorescent intensity from the nanocoral (300 nm in diameter) and flat gold substrates. In the case of 1 μM R6G incubation, the equilibrium fluorescent intensity from the nanocoral array (red line) is 53 times larger than the flat gold substrates (red dashed line).

9.3 Results and Discussion

Polystyrene (PS) nanospheres provide a simple and versatile template for nanostructure fabrication because of their monodisperse size distribution, large range of available particle sizes from several nm to several mm, simplicity of forming self-assembled hexagonal arrays on surfaces, and well-developed chemical processes for etching. A large number of recent substrates, including nanodisks [150], nanoholes [105], nanovoids [151], nanopillars [152], nanocrescents [153] and crescent-shaped nanoholes [154] have been built using nanosphere lithography by using the PS nanospheres as masks for thin film deposition and directional dry etching. Oxygen plasma is a common technique for tailoring the size and interparticle distance of the PS nanospheres, and as the etching process proceeds, the PS nanosphere size decreases while the surface roughness increases. Although the surface roughness of the nanosphere template is usually considered a drawback that limits the range of PS sphere sizes upon etching, here we utilize this etching-induced roughness as the basic template structure of our nanocorals. Roughness formation during etching has been observed in PS nanospheres during plasma etching [155], though the causes for surface roughness formation are still not completely understood. We suggest the roughness observed in the nanocorals can be explained by a combination of etchant shadowing and first-order reemission effects [156, 157], however more study is needed to prove the cause(s)

of roughening. Presence of crystalline domains in the PS may also effect the resulting geometry. The gradual change of the surface roughness of nanocorals during etching is shown in Figure 9.2(e).

We demonstrate the sensing capability of the ultra-rough region of the nanocoral by characterizing the nanocoral array before release into solution (after process step shown in Figure 9.2(c)). In contrast to smooth nanoparticle probes, the high surface area of the nanocoral causes increased adsorption capacity. To demonstrate this effect, we incubated the nanocoral array with Rhodamine 6G (R6G) solution, dried the substrate with nitrogen gas, and measured the fluorescent signal intensity of adsorbed R6G on the nanocoral substrate versus that of a flat gold film. We note that while R6G is not a biomolecule and would likely not be used for sensing in a cellular environment, it is a common molecule used to characterize SERS and fluorescence, and hence allows a comparison of nanocorals with previous and future substrates. As shown in Figure 9.4(a) and Figure 9.3, the nanocoral region has a 50 times higher fluorescence intensity per unit area than the flat gold surface. The increase in fluorescent signal is at least partially due to increased adsorption of R6G on the nanocoral substrate; however, we cannot rule out surface enhanced fluorescence due to hot-spots or quenching on the gold surface contributing to the observed signal as well. We note the higher fluorescence intensity from the nanocoral array is not attributed to surface enhanced fluorescence due to localized surface plasmon resonance (LSPR) of the nanocoral, since there is no overlapping of the LSPR of the nanocoral substrate (Figure 9.8(a)) with the adsorption/emission spectra of R6G (530 nm/570 nm).

As shown in the inset to Figure 9.4(a), the nanocoral region has significantly higher fluorescence intensity than the flat gold surface: the arrayed nanocorals adsorb 50 times more R6G molecules per unit area than the flat gold surface (Figure 9.3). We note the higher fluorescence intensity from the nanocoral array is not attributed to surface enhanced fluorescence due to localized surface plasmon resonance (LSPR) of the nanocoral, since there is no overlapping of the LSPR of the nanocoral substrate (Figure 9.8(a)) with the adsorption/emission spectra of R6G (530 nm/570 nm).

We then performed SERS measurement of the nanocoral array to characterize the utility of the rough region of the nanocoral as a SERS biosensor. The SERS measurements were taken from nanocorals immersed in known concentrations of R6G solution. We used a 785 nm excitation laser, which is a widely adopted wavelength within the biological window, with a 0.3 mW excitation power. The measurement area was 3μm by 1μm, defined by the focused laser spot size and the slit in front of the spectrometer. The SERS measurement was conducted with a 1 mm thick layer of R6G solution on top of the nanocoral substrate; the solution was sandwiched between the substrate and a glass cover slip, with a 1 mm Polydimethylsiloxane (PDMS) spacer. We note that small peaks observed for DI water, which are coincidentally near the

R6G peaks, are likely caused by the by-product of oxygen plasma-etched polystyrene.

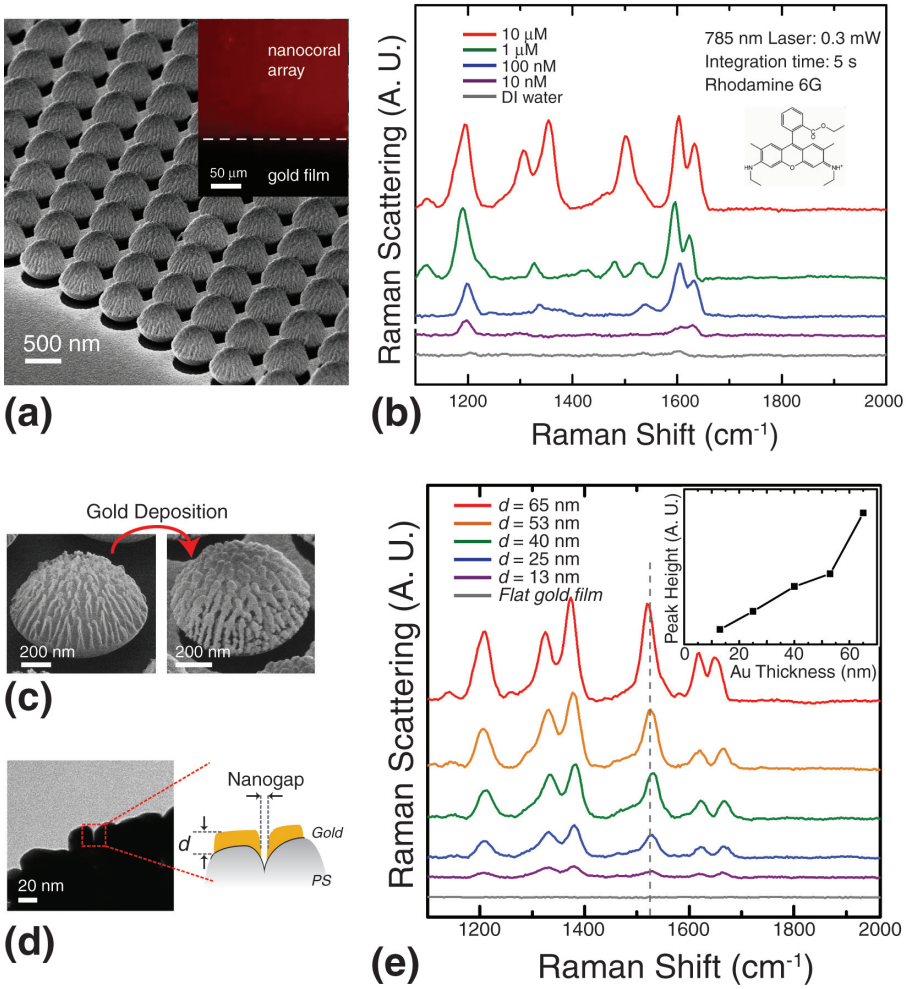

Figure 9.4: SERS signal from nanocorals; (a) SEM images of a nanocoral array; inset shows R6G fluorescent intensity from the nanocoral array and flat gold film; (b) SERS spectra for varying R6G concentration from nanocoral substrate; (c) SEM images of nanocorals before and after gold deposition, (d) representative TEM image of sub-10 nm nanocoral nanogap and (e) SERS spectra for nanocorals with different gold thickness (R6G concentration 10 μM).

We observe a limit of detection of approximately 10 nM of R6G (Figure 9.4(b)) due to the roughness of the nanocoral surface. This SERS performance is good compared to other arrayed gold substrates that have been reported for R6G detection [27, 158, 159]. Importantly, we find the SERS intensity does not fluctuate significantly across different regions of the sample (Figure 9.5), which is in stark contrast

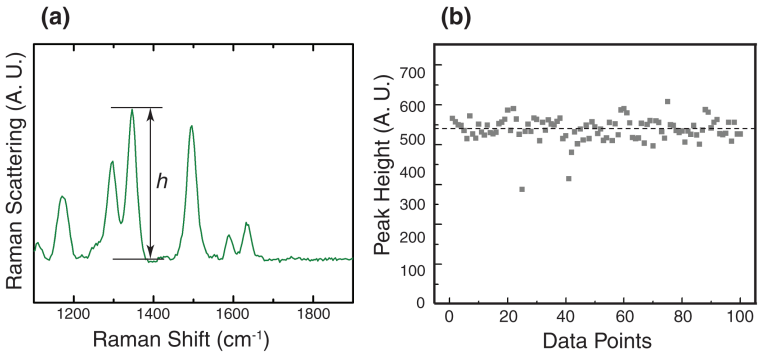

Figure 9.5: SERS signal uniformity test of the nanocoral substrate with 800 nm PS template and 53 nm gold coating (the same sample as in Figure 3); (a) a representative SERS spectrum for 10 μM R6G solution; (b) the scattering plot of peak height at 1360 cm^{-1} (h marked in (a)) for 100 data points. The standard deviation is 7%, which is in stark contrast to many previous roughened SERS substrates.

to many previously reported roughened SERS substrates. Across a nanocoral substrate, the standard deviation in SERS signal was found to be 7% ($n = 100$); this finding emphasizes the reproducibility of the oxygen plasma roughening method. We note that while local hot-spots (which lead to SERS) are likely to vary in intensity at different locations, the distribution of these hot-spots over a nanocoral produces a uniform signal. To further characterize the SERS signal from *single* nanocorals, we fabricated sparsely distributed nanocorals on the glass substrate, allowing us to focus on a single nanocoral. The single nanocoral exhibits consistent SERS results to those of the nanocoral arrays (Figure 9.7): some R6G peaks are apparent at 10 nM and clear fingerprint spectrum is present at 10 μM.

While retaining the same PS template, the Raman signal enhancement capability of the nanocorals can be tuned by the thickness of gold deposition. We speculate that as the gold coats the PS template, the trenches become narrower, resulting in sub-10 nm gaps between the adjacent ridges (Figure 9.4(d), TEM image). We hypothesize that these sub-10 nm gaps are the primary cause of the good SERS signal from the nanocorals. This hypothesis is supported by the thickness dependence of the SERS signal shown in Figure 9.4(e): the signal increases as thickness increases up to approximately 63 nm, resulting in narrower nanogaps on the surface. Further gold thickness begins to fill the trenches and reduces SERS signal.

Having characterized the sensitivity and uniformity of the roughened gold region of the nanocoral, we next demonstrate the targeting function of the PS region. While the gold coated surface of the nanocorals can be used for SERS detection, the PS template of the nanocorals can simultaneously be used to adsorb antibodies or other biological ligands based on hydrophobic attraction, which is widely used for immunological

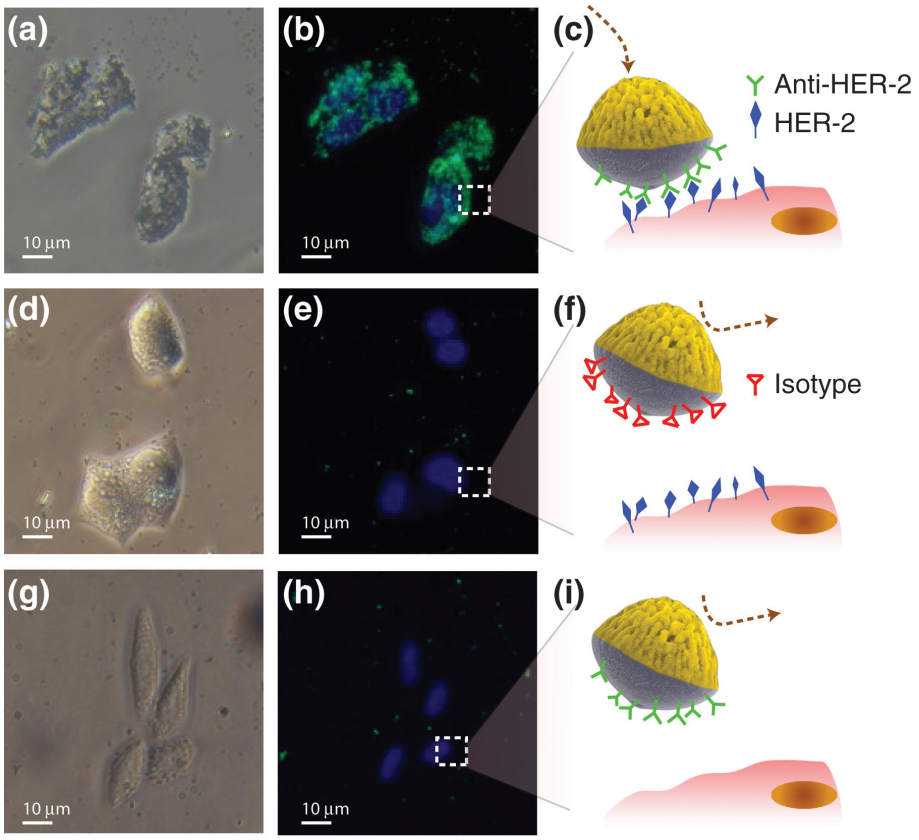

Figure 9.6: Nanocorals as multifunctional probes for living cells; (a) bright field, (b) fluorescent, and (c) schematic images of 300 nm nanocorals attached to BT474 cell surfaces with HER-2/anti-HER-2 binding; fluorescent PS nanospheres are used as the nanocoral template; (d) bright field, (e) fluorescent, and (f) schematic images for a control experiment where PS is functionalized with isotype antibodies, and very few nanocorals bind to the cells; (g) bright field, (h) fluorescent, and (i) schematic images for a control experiment for HeLa cells with PS functionalized with anti-HER-2, and very few nanocorals bind to the cells.

assays [147].

This targeting is demonstrated in Figure 9.6, where by incubating nanocoral suspensions with antibodies (Anti-HER-2/neu, Becton Dickinson), we are able to specifically target breast cancer cells (BT474 cell line, ATCC). These cells overexpress Human Epidermal growth factor Receptor 2 (HER-2), which is a well known target for cancer treatment. Figure 9.6(a) shows a phase contrast image of anti-HER-2 functionalized nanocorals attached to the surface of BT474 breast cancer cells, after incubation for 30 mins followed by washing steps. To verify the location of the

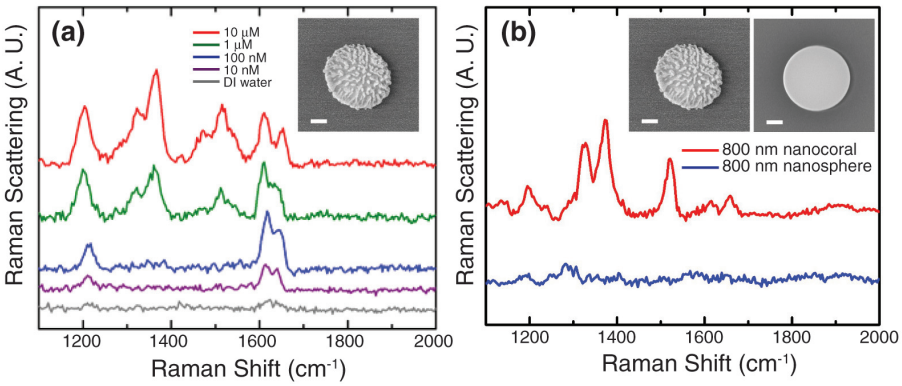

Figure 9.7: SERS from single nanocoral; (a) SERS signal from single nanocoral with different R6G concentration, Raman measurement conditions: 785 nm laser at 0.3 mW, 40X objective lens, and 20 sec integration time. (b) SERS signal from the nanocoral and smooth gold-covered nanosphere; (scale bar = 200 nm, R6G concentration = 100 μM, same Raman measurement conditions as (a) with 5 sec integration time.)

nanocorals, a fluorescent PS nanosphere was used as the PS template, and these nanocorals can be clearly seen on the cell surfaces in Figure 9.6(b) (Hoest 33342 dyed cell nucleus in blue). Control experiments (Figure 9.6(d-i)) show nanocorals do not attach to the cell surface when nanocorals are functionalized with isotype antibodies (Mouse Ig Fluorescence Controls, BD Biosciences), or when cells which do not overexpress HER-2 are used. The HER-2 receptor is known to have a fast recycling rate and therefore we expect the receptor-mediated endocytosis of nanocorals will allow for intracellular imaging [160]. By targeting other slowly recycled cancer markers such as epidermal growth factor receptor (EGFR) [146], we expect nanocorals can be designed to stay on the cell membrane for longer times. We emphasize that the ultimate goal of the nanocoral probes would not be to sense HER-2, but instead to use the SERS portion of the probe for multiplexed local detection of biomolecules. In future work, we plan to combine the specific attachment of the functionalized PS region and the high SERS signal from the roughened gold of the nanocorals to create a molecular map of biomolecules at the cell surface. We confirm that antibody attachment is primarily on the PS surface, leaving the gold surface clean for SERS measurements, in Figure 9.10.

The versatility of the nanosphere fabrication process allows nanocorals to be fabricated over a wide range of sizes for different applications. In Figure 9.9, PS sphere templates for nanocorals with diameters 100 nm, 200 nm, 300 nm, 500 nm, and 800 nm are shown. The rough surface pattern of each nanocoral is observed to be very similar regardless of the PS template size, again supporting the reproducibility of the

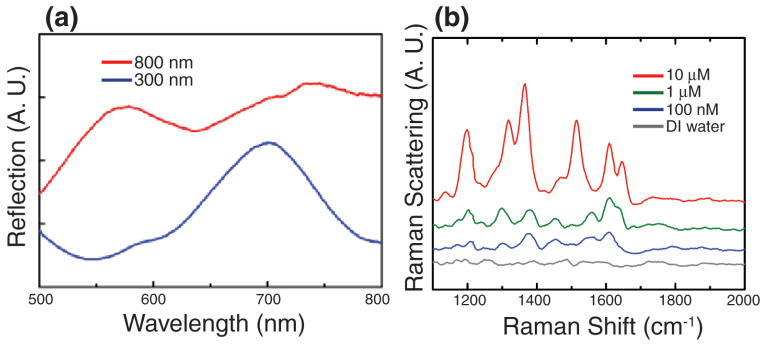

Figure 9.8: LSPR effects in nanocorals; (a) optical reflection spectrum from 800 nm and 300 nm nanocoral arrays; (b) SERS signal from 300 nm nanocorals for varying R6G concentration (same Raman measurement conditions as Fig. 3(b)).

oxygen plasma roughening technique. In the case of 800 nm nanocoral, hot-spots on the roughened surface dominate the Raman signal enhancement. This is confirmed by comparing the SERS signal from single 800 nm nanocorals and single 800 nm PS nanospheres covered with the same gold film thickness: we observe no SERS signal for the smooth gold-coated spheres, while a strong signal is seen for the nanocorals (Figure 9.7(b)).

While there is potential to use the LSPR of the entire nanocoral structure to improve the SERS signal, we find the surface roughness features are dominant. For example, the SERS sensitivity of 300 nm nanocorals are not superior to 800 nm nanocorals, despite a clear LSPR spectral peak near 700 nm. However, further fine-tuning of the size and thickness of smaller nanocorals to optimize both shell LSPR and surface hot-spots may lead to better enhancement capabilities.

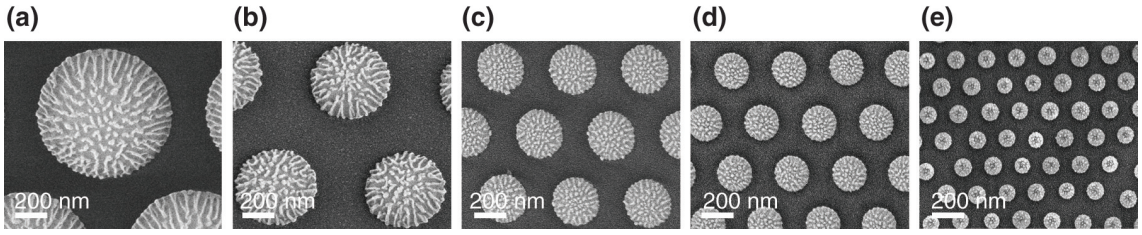

Figure 9.9: Scalability of nanocoral fabrication; SEM images of the roughened PS template of (a) 800 nm, (b) 500 nm, (c) 300 nm, (d) 200 nm, and (e) 100 nm.

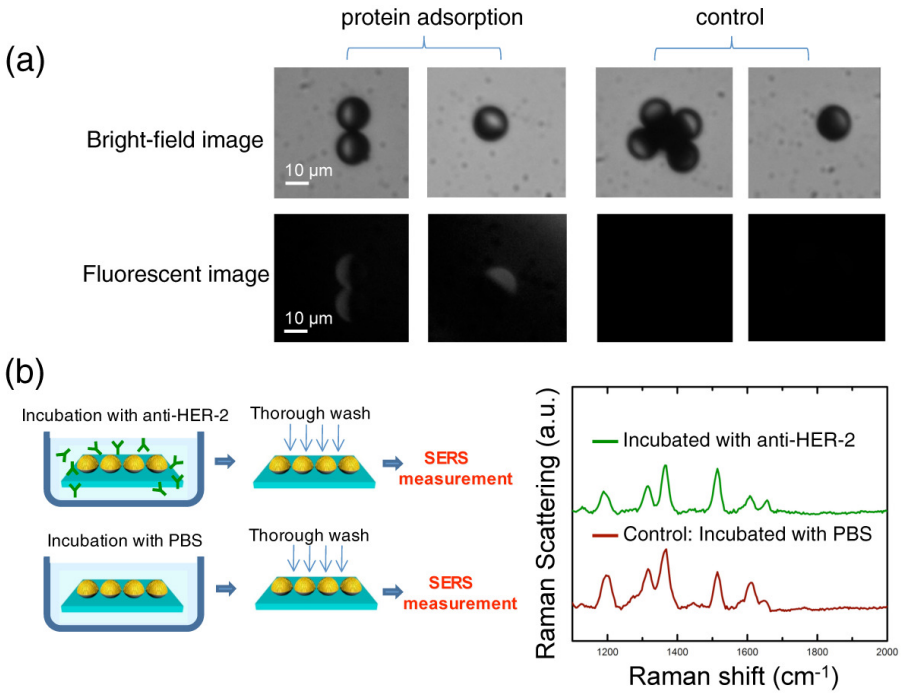

Figure 9.10: Verification of selective attachment of antibody on PS surface; (a) large nanocorals (10 μm) were fabricated and incubated with FITC-tagged BSA solution at 4° C overnight, followed by thorough washing in PBS; the fluorescent image demonstrates the selection adsorption of the protein on the PS surface due to hydrophobic adsorption; (b) to further verify that the gold surface remains clean for SERS detection, 300 nm nanocoral arrays are incubated with HER-2 antibody for 24 hours at 4° C, following by washing, and SERS measurement of R6G (with the same conditions as Fig. 3). The control is conducted by incubating the nanocoral substrate with PBS for the same incubation, washing, and SERS steps. The nearly identical SERS signals indicate the HER-2 antibody has not adsorbed on the gold surface at any concentration significant enough to affect the SERS detection of R6G.

9.4 Conclusion

In conclusion, we have demonstrated nanocorals as simple and cost-effective nanoprobes for SERS sensing and targeting. The highly roughened gold region of the nanocoral can adsorb more R6G than a flat gold surface, and has a SERS limit of detection of 10 nM R6G with high reproducibility. After release from the substrate and functionalization of the PS region with antibodies, nanocorals attach specifically to breast cancer cells. We have shown the scalability of the nanocorals from 100 nm to 800 nm.

Because the nanocoral fabrication technique presented here uses a PS template

to create the roughened features, it is not limited to gold. Any material that can be evaporated can be deposited on the PS template, offering this method not just to other plasmonic metals, but other materials that may be of interest for chemical sensors or catalytic converters. In addition, fluorescent markers, drugs, or other chemicals may be embedded in the PS template region to add increased functionality to the nanocoral probes.

Chapter 10

Conclusion

"The road goes ever on and on,
down from the door where it began."

JRR Tolkien

10.1 Summary

After introducing the near and far field measures of plasmon resonance, we hypothesized in Chapter 2 that these measures may actually occur at significantly different wavelengths, depending on the particle geometry and material. These differences are especially important for molecular detection applications. We developed a mathematical framework based on the quasi-static approximation that successfully predicts the differences among the measures, and how they depend on material and particle geometry. Specifically, we proposed the general relation $\lambda_{\text{max, near}} \geq \lambda_{\text{max, scattering}} \geq \lambda_{\text{max, absorption}}$; that is, the optimum wavelength for near-field resonance is greater than or equal to that for far-field scattering, which in turn is greater than that for absorption. Additionally, the differences among these measures increase with the material loss (e.g. the differences are greater for gold than for silver), and the differences also increase with particle volume due to damping effects. Changing the particle shape can shift the resonance of all measures without causing a significant divergence among them. After predicting these effects with simple algebraic expressions, we verified them using rigorous Mie theory and FEM computation. These rigorous solutions provided quantified differences among the measures for relevant geometries and material properties.

In Chapters 3 and 4, we introduced two new techniques for the fabrication of nanoplasmonic architectures. We focused particularly on the creation of nanogaps using simple large area techniques, in contrast to the expensive serial techniques such as e-beam and FIB lithographies that are commonly used in the literature. Active polymer nanofabrication was introduced as a new technique, inspired by the natural process of morphogenesis, to manipulate nanostructure morphology. Active polymer nanofabrication allows the potential to alter structure-to-structure distance down to sub-10 nm, surpassing both resolution and structural density of the initial placement. In addition, polymer molding offers macroscopic deformation of plasmonic architectures into arbitrary 3-dimensional geometries. Electroless deposition was introduced as a second method to tune the nanogap distances of nanoplasmonic antennas, and we characterized the morphological, optical, and SERS response for the electroless deposition of gold on nanoprism arrays fabricated with nanosphere lithography. The gap distance between nanoprisms was reduced by a factor of 4 within tens of seconds. Using microfluidic Y-channels, we observed the realtime evolution of the optical spectrum as nanoprisms grew and merged into a gold film. The SERS sensitivity was shown to increased two orders of magnitude after electroless deposition.

In Chapters 5-8, we turned our attention to the geometric design of nanoplasmonic antennas, with a focus on a novel group of architectures in which the close proximity of two or more nanoplasmonic components causes their resonances to be linked together *via* plasmon-coupling. Four such structures are discussed: the nanocres-

cent, the crescent-shaped nanohole, the plasmon enhanced particle-cavity (PEP-C) system, and the core-satellite system. In each case, we introduced the general design concept of the system, introduced its potential advantages over other systems, and systematically investigated the effect of each relevant geometric parameter. The nanocrescent and its counterpart, the crescent-shaped nanohole, utilize both sharp tips and intra-particle coupling to achieve high local field enhancement. The PEP-C system combines particle and cavity geometries to create a high density of hot-spots. Finally, the core-satellite system is based on the interaction of a central nanoparticle with multiple smaller particles.

In Chapter 9, we then introduced a new class of bioinspired nanoplasmonic structures called nanocoral, designed specifically for molecular sensing *in vivo*–within or on the surface of living cells. Analogous to natural sea corals that use rough surfaces to maximize surface area for efficient capture of light and food particles, nanocorals utilize a highly roughened surface at the nanoscale to increase analyte adsorption capacity, and create a high density of surface-enhanced Raman spectroscopy (SERS) hot-spots. Nanocorals are unique in that they combine cellular specific targeting with biomolecular sensing, yet decouple the two functional modes. We demonstrated the specific attachment to breast cancer cells, and the reproducible SERS detection of R6G at 10nM.

10.2 Future Work

As nanoplasmonics has evolved in recent years, much focus (including that of this dissertation) has been developing fundamental understanding of design rules for nanoplasmonic systems. As these rules are beginning to be well-known, the key challenges of nanoplasmonics are become focused on fabrication and integration.

A large challenge is in the reproducible fabrication of nanoplasmonic antenna. The $\approx 1/a$ distance dependence of the electric field motivates the creation of nanogap structures, yet the high sensitivity to gap distance makes reproducible fabrication a challenge. While many of the nanoplasmonic fundamentals have been developed in systems using e-beam and FIB lithography, these techniques are in general not feasible for large area applications. Bottom-up fabrication techniques, or a combination of bottom-up and top-down techniques hold much promise for allowing nanoplasmonic systems to be fabricated commercially. Certainly, as fabrication techniques continue to rapidly advance, driven by the semiconductor industry as well as the broad field of nanotechnology, nanoplasmonics will reap the benefits.

The integration of nanoplasmonics into useful systems is still in its early stages. Microfluidics offers a useful a platform for nanosplasmonic molecular sensors, since it can control the amount of analyte delivered to the sensor. While some work on integration was shown in this dissertation (for example, electrolessly deposited

nanoprisms were shown integrated with microfluidics), there are clearly synergies between microfluidics and nanoplasmonics that have yet to be realized.

For those specifically interested in following up on research presented in this dissertation, here we will briefly summarize a few key areas:

Near/Far field Theory:

The theoretical framework developed in Chapter 2 has yet to be rigorously tested experimentally, yet all the tools to test the theoretical predictions are available.

Active polymer nanofabrication:

This technique has many unanswered questions: how well can the gap distance be controlled? Can the technique be extended to structures fabricated with traditional lithographies? Can polymers with a greater shape change be used for more drastic results?

Nanogaps via Electroless deposition:

The technique can be extended to create smaller nanogaps than shown in bulk solution. We expect the growth was limited by buildup on the particle surface; if this can be eliminated by cleaning or by using a different plating solution, significant improvements in the method should be possible. Additionally, the technique was only shown with structures defined by nanosphere lithography; it would be interesting to see if electroless deposition can create useful plasmonic sensors out of structures defined with conventional lithographies.

Nanocrescent:

Nanocrescents are ready for *in-vivo* testing, and have great potential utilizing multiple sensing and targeting modalities, much like nanocorals.

Crescent-shaped Nanoholes:

These structures are particularly intriguing because of their compatibility with flow-through microfluidics, wherein the molecule of interest could be localized in the hole. Additionally, there is further basic understanding of the tuning capabilities crescent-shaped nanoholes that can be conducted. These structures might also provide valuable for metamaterials research.

PEP-C:

While initial work was conducted on fabrication of these structures, they have yet to be reproducibly fabricated and characterized.

Core-satellite Systems:

This work has since been developed for use in an example system, but there are

many valuable diagnostics that can be developed with the design rules presented here.

Nanocorals:

Nanocorals are ready for *in-vivo* testing for a relevant biological question.

References

Bibliography

[1] A. Aubry, D. Y. Lei, A. I. Fernandez-Dominguez, Y. Sonnefraud, S. A. Maier, and J. B. Pendry. Plasmonic light-harvesting devices over the whole visible spectrum. *Nano Lett.*, 10:2574, 2010.

[2] G. Mie. Beiträge zur optik trüber medien, speziell kolloidaler metallösungen. *Ann. Phys.*, 25:377, 1908.

[3] P. Drude. Zur elektronentheorie der metalle. *Ann. Phys.*, 306:566, 1900.

[4] P. Drude. Zur elektronentheorie der metalle; II. Teil. galvanomagnetische und thermomagnetische effecte. *Ann. Phys.*, 308:369, 1900.

[5] C. L. Haynes and R. P. Van Duyne. Nanosphere lithography: A versatile nanofabrication tool for studies of size-dependent nanoparticle optics. *J. Phys. Chem. B*, 105:5599, 2001.

[6] K. Kneipp, Y. Wang, H. Kneipp, L. T. Perelman, I. Itzkan, R. R. Dasari, and M. S. Feld. Single molecule detection using surface-enhanced Raman scattering (SERS). *Phys. Rev. Lett.*, 78:1667, 1997.

[7] T.W. Ebbesen, H. F. Ghaemi, T. Thio, and P. A. Wolff. Extraordinary optical transmission through sub-wavelength hole arrays. *Nature*, 391:667, 1998.

[8] E. Ozbay. Plasmonics: Merging photonics and electronics at nanoscale dimensions. *Science*, 311:189, 2006.

[9] S. Kim, J. Jin, Y.-J. Kim, I.-Y. Park, Y. Kim, and S.-W. Kim. High-harmonic generation by resonant plasmon field enhancement. *Nature*, 453:757, 2008.

[10] L. R. Hirsch, R. J. Stafford, J. A. Bankson, S. R. Sershen, B. Rivera, R.E. Price, J.D. Hazle, N. J. Halas, and J. L. West. Nanoshell-mediated near-infrared thermal therapy of tumors under magnetic resonance guidance. *PNAS*, 100:13549–13554, 2003.

[11] S. A. Maier. *Plasmonics: Fundamentals and Applications*. Springer, NY, 2007.

[12] J. D. Jackson. *Classical Electrodynamics*. John Wiley & Sons, USA, 3 edition, 1999.

[13] P. B. Johnson and R. W. Christy. Optical constants of the noble metals. *Phys. Rev. B*, 6:4370, 1972.

[14] M. Born and E. Wolf. *Principles of Optics*. Permagon Press, 1970.

[15] C. F. Bohren and D. R. Huffman. *Absorption and Scattering of Light by Small Particles*. John Wiley & Sons, 1983.

[16] C. Liang and Y. T. Lo. Scattering by two spheres. *Radio Sci.*, 2:1481, 1967.

[17] J. H. Bruning and Y. T. Lo. Multiple scattering of EM waves by spheres, part I & II. *IEEE Trans. Anten. Prop.*, AP-19:378, 1971.

[18] K. A. Fuller and G. W. Kattawar. Consummate solution to the problem of classical electromagnetic scattering by ensembles of spheres. I & II. *Opt. Lett.*, 13:1063, 1988.

[19] D. W. Mackowski. Analysis of radiative scattering for multiple sphere configurations. *Proc. R. Soc. London Ser. A*, 433:599, 1991.

[20] Y. l. Xu. Electromagnetic scattering by an aggregate of spheres: far field. *Appl. Opt.*, 36:9496, 1997.

[21] M. Fleischmann, P. J. Hendra, and A. J. McQuillan. Raman spectra of pyridine adsorbed at a silver electrode. *Chem. Phys. Lett.*, 26:163, 1974.

[22] D. B. Chase and B. A. Parkinson. Surface-enhanced Raman spectroscopy in the near-infrared. *Appl. Spectrosc.*, 42:1186, 1988.

[23] D. Zeisel, V. Deckert, R. Zenobi, and T. Vo-Dinh. Near-field surface-enhanced Raman spectroscopy of dye molecules adsorbed on silver island films. *Chem. Phys. Lett.*, 283:381, 1998.

[24] J. Liu and Y. Lu. Fast colorimetric sensing of adenosine and cocaine based on a general sensor design involving aptamers and nanoparticles. *Angew. Chem. Int. Ed.*, 45(1):90–94, 2005.

[25] L. A. Dick, A. D. McFarland, C. L. Haynes, and R. P. Van Duyne. Metal film over nanosphere (MFON) electrodes for surface-enhanced Raman spectroscopy (SERS): Improvements in surface nanostructure stability and suppression of irreversible loss. *J. Phys. Chem. B*, 106:853, 2002.

[26] L. H. Qian, X. Q. Yan, T. Fujita, A. Inoue, and M. W. Chen. Surface enhanced Raman scattering of nanoporous gold: Smaller pore sizes stronger enhancements. *Appl. Phys. Lett.*, 90:153120, 2007.

[27] G. Duan, W. Cai, Y. Luo, Y. Li, and Y. Lei. Hierarchical surface rough ordered Au particle arrays and their surface enhanced raman scattering. *Appl. Phys. Lett.*, 89:181918, 2006.

[28] A. Wei, B. Kim, B. Sadtler, and S. L. Tripp. Tunable surface-enhanced Raman scattering from large gold nanoparticle arrays. *ChemPhysChem*, 2:743, 2001.

[29] K. Kneipp, H. Kneipp, I. Itzkan, R. R. Dasari, and M. S. Feld. Surface-enhanced Raman scattering and biophysics. *J. Phys.*, 14:R597, 2002.

[30] K. Kneipp, A. S. Haka, H. Kneipp, K. Badizadegan, N. Yoshizawa, C. Boone, K. E. Shafer-Peltier, J. T. Motz, R. R. Dasari, and M. S. Feld. Surface-enhanced Raman spectroscopy in single living cells using gold nanoparticles. *Appl. Spectrosc.*, 56:150, 2002.

[31] X. Qian, X. Peng, D.Ansari, Q. Yin-Goen, G. Z. Chen, D. M. Shin, L. Yang, A. N. Young, M. D. Wang, and S. Nie. In vivo tumor targeting and spectroscopic detection with surface-enhanced Raman nanoparticle tags. *Nature Biotechnology*, 26:83, 2008.

[32] I. R. Nabiev and H. Morjani nd M. Manfait. Selective analysis of antitumor drug interaction with living cancer cells as probed by surface-enhanced Raman spectroscopy. *European Biophysics journal*, 19:311, 1991.

[33] E. Fort and S. Grésillon. Surface enhanced fluorescence. *J. Phys. D.*, 41:013001, 2008.

[34] G. L. Liu, Y.-T. Long, Y. Choi, T. Kang, and L. P. Lee. Quantized plasmon quenching dips nanospectroscopy via plasmon resonance energy transfer. *Nat. Methods*, 4:1015, 2007.

[35] A. J. Haes, S. Zou, G. C. Schatz, and R. P. Van Duyne. Nanoscale optical biosensor: short range distance dependence of the localized surface plasmon resonance of noble metal nanoparticles. *J. Phys. Chem. B*, 108:6961, 2004.

[36] K. Willets and R. P. van Duyne. Localized surface plasmon resonance spectroscopy and sensing. *Ann. Rev. Phys. Chem.*, 58:267, 2006.

[37] J. N. Anker, W. P. Hall, O. Lyandres, N. C. Shah, J. Zhao, and R. P. Van Duyne. Biosensing with plasmonic nanosensors. *Nat. Mater.*, 7:442–453, 2008.

[38] P. K. Jain, K. S. Lee, I. H. El-Sayed, and M. A. El-Sayed. Calculated absorption and scattering properties of gold nanoparticles of different size, shape, and composition: Applications in biological imaging and biomedicine. *J. Phys. Chem. B*, 110:7238, 2006.

[39] A. N. Grigorenko, N. W. Roberts, M. R. Dickinson, and Y. Zhang. Nanometric optical tweezers based on nanostructured substrates. *Nature Photon.*, 2:365, 2008.

[40] S. E. Lee, G. L. Liu, F. Kim, and L. P. Lee. Remote optical switch for localized and selective control of gene interference. *Nano Lett.*, 9:562, 2009.

[41] B. J. Messinger, K. U. von Raben, R. K. Chang, and P. W. Barber. Local fields at the surface of noble-metal microspheres. *Phys. Rev. B*, 24:649, 1981.

[42] H. Kuwata, H. Tamaru, K. Esumi, and K. Miyano. Resonant light scattering from metal nanoparticles: Practical analysis beyond Rayleigh approximation. *Appl. Phys. Lett.*, 83:4625, 2003.

[43] F. Hao and P. Nordlander. Efficient dielectric function for FDTD simulation of the optical properties of silver and gold nanoparticles. *Chem. Phys. Lett.*, 446:115–118, 2007.

[44] A. D. Rakić, A. B. Djurišić, J. M. Elazar, and M. L. Majewski. Optical properties of metallic films for vertical-cavity optoelectronic devices. *Appl. Opt.*, 37:5271, 1998.

[45] R. C. Jaeger. *Introduction to Microelectronic Fabrication.* Prentice Hall, USA, 2 edition, 2002.

[46] S. F. Gilbert. *Developmental Biology.* Sinauer Associates, USA, 8 edition, 2006.

[47] M. Domínguez and F. Casares. Organ specification-growth control connection: New in–*sights* from the drosophila eye-antennal disc. *Dev. Dyn.*, 232:673–684, 2005.

[48] L. P. Lee and R. Szema. Inspirations from Biological Optics for Advanced Photonic Systems. *Science*, 310(5751):1148–1150, 2005.

[49] K.-H. Jeong, J. Kim, and L. P. Lee. Biologically Inspired Artificial Compound Eyes. *Science*, 312(5773):557–561, 2006.

[50] Y. Bar-Cohen. *Electroactive Polymer (EAP) actuators as artificial muscles.* SPIE, Washington, 2 edition, 2004.

[51] R. Mohr, K. Kratz, T. Weigel, M. Lucka-Gabor, M. Moneke, and A. Lendlein. Initiation of shape-memory effect by inductive heating of magnetic nanoparticles in thermoplastic polymers. *PNAS*, 103:3540–3545, 2006.

[52] A. Lendlein, H. Jiang, O. Jünger, and Robert Langer. Light-induced shape-memory polymers. *Nature*, 434:879–882, 2005.

[53] A. Grimes, D. N. Breslauer, M. Long, J. Pegan, and M. Khine. Shrinky-dink microfluidics: rapid generation of deep and rounded patterns. *Lab Chip*, 8:170, 2008.

[54] C. Sanchez, H. Arribart, M. Madeleine, and G. Guille. Biomimetism and bioinspiration as tools for the design of innovative materials and systems. *Nature Mater.*, 4:277, 2005.

[55] J. Aizenberg and P. Fratzl. Biological and biomimetic materials. *Adv. Mater.*, 21:387, 2009.

[56] J. Aizenberg, J. C. Weaver, M. S. Thanawala, V. C. Sundar, D. E. Morse, and P. Fratzl. Skeleton of Euplectella sp.: Structural hierarchy from the nanoscale to the macroscale. *Science*, 309:275, 2005.

[57] D.-H. Kim and J. A. Rogers. Stretchable electronics: Materials strategies and devices. *Adv. Mater.*, 20:4887–4892, 2008.

[58] B. M. Ross and L. P. Lee. Creating high density nanoantenna arrays via plasmon enhanced particle-cavity (PEP-C) architectures. *Optics Express*, 17:6860, 2009.

[59] B. M. Ross and L. P. Lee. Comparison of near- and far-field measures for plasmon resonance of metallic nanoparticles. *Opt. Lett.*, 34:896–898, 2009.

[60] E. M. Terentjev S. V. Ahir, A. R. Tajbakhsh. Self-assembled shape-memory fibers of triblock liquid-crystal polymers. *Adv. Func. Mater.*, 16:556–560, 2006.

[61] A. Sundaramurthy, K. B. Crozier, G. S. Kino, D. P. Fromm, P. J. Schuck, and W. E. Moerner. Field enhancement and gap-dependent resonance in a system of two opposing tip-to-tip Au nanotriangles. *Phys. Rev. B*, 72:165409, 2005.

[62] L. B. Freund and S. Suresh. *Thin Film Materials: Stress, Defect Formation and Surface Evolution*. Cambridge University Press, Cambridge, 2003.

[63] A. D. McFarland, M. A. Young, J. A. Dieringer, and R. P. van Duyne. Wavelength-scanned surface-enhanced Raman excitation spectroscopy. *J. Phys. Chem. B*, 109:11279–11285, 2005.

[64] A. J. Haes, S. Zou, J. Zhao, G. C. Schatz, , and R. P. van Duyne. Localized surface plasmon resonance spectroscopy near molecular resonances. *J. Am. Chem. Soc.*, 128:10905–1091, 2006.

[65] C. L. Haynes, A. D. McFarland, L. Zhao, R. P. Van Duyne, G. C. Schatz, L. Gunnarsson, J. Prikulis, B. Kasemo, and M. Käll. Nanoparticle optics: The importance of radiative dipole coupling in two-dimensional nanoparticle arrays. *J. Phys. Chem. B*, 107:7337, 2003.

[66] X. Zhang, E. M. Hicks, J. Zhao, G. C. Schatz, and R. P. van Duyne. Electrochemical tuning of silver nanoparticles fabricated by nanosphere lithography. *Nano Lett.*, 5:1503–1507, 2005.

[67] T. Hartling, Y. Alaverdyan, M. T. Wenzel, R. Kullock, M. Kall, and L. M. Eng. Photochemical tuning of plasmon resonances in single gold nanoparticles. *J. Phys. Chem. C*, 112:4920–4924, 2008.

[68] C. L. Haynes, A. D. McFarland, L. Zhao, R. P. van Duyne, G. C. Schatz, L. Gunnarsson, J. Prikulis, B. Kasemo, and M. K all. Nanoparticle optics: the importance of radiative dipole coupling in two-dimensional nanoparticle arrays. *J. Phys. Chem. B*, 107:7337–7342, 2003.

[69] A. Vogal and V. Venugopalan. Mechanisms of pulsed laser ablation of biological tissues. *Chem. Rev.*, 103:577, 2003.

[70] P. K. Aravind, A. Nitzan, and H. Metiu. The interaction between electromagnetic resonances and its role in spectroscopic studies of molecules adsorbed on colloidal particles or metal spheres. *Surf. Sci.*, 110:189, 1981.

[71] J. P. Kottmann and O. J. F. Martin. Plasmon resonant coupling in metallic nanowires. *Opt. Express*, 8:655, 2001.

[72] J. Aizpurua, G. W. Bryant, L. J. Richter, F. J. García de Abajo, B. K. Kelley, and T. Mallouk. Optical properties of coupled metallic nanorods for field-enhanced spectroscopy. *Phys. Rev. B*, 71:235420, 2005.

[73] K. Halterman, J. M. Elson, and S. Singh. Plasmonic resonances and electromagnetic forces between coupled silver nanowires. *Phys. Rev. B*, 72:075429, 2005.

[74] J. Kim, G. L. Liu, Y. Lu, and L. P. Lee. Intra-particle plasmonic coupling of tip and cavity resonance modes in metallic apertured nanocavities. *Opt. Express*, 13:8332, 2005.

[75] B. M. Ross and L. P. Lee. Plasmon tuning and local field enhancement maximization of the nanocrescent. *Nanotechnology*, 19:275201, 2008.

[76] G. L. Liu, Y. Lu, J. Kim, J. C. Doll, and L. P. Lee. Magnetic nanocrescents as controllable surface-enhanced Raman scattering nanoprobes for biomolecular imaging. *Adv. Mater.*, 17:2683, 2005.

[77] J. S. Shumaker-Parry, H. Rochholz, and M. Kreiter. Fabrication of crescent-shaped optical antennas. *Adv. Mater.*, 17:2131, 2005.

[78] Y. Lu, G. L. Liu, J. Kim, Y. X. Mejia, and L. P. Lee. Nanophotonic crescent moon structures with sharp edge for ultrasensitive biomolecular detection by local electromagnetic field enhancement effect. *Nano Lett.*, 5:119, 2005.

[79] H. Rochholz, N. Bocchio, and M. Kreiter. Tuning resonances on crescent-shaped noble-metal nanoparticles. *New J. Phys.*, 9:53, 2007.

[80] R. Bukasov and J. S. Shumaker-Parry. Highly tunable infrared extinction properties of gold nanocrescents. *Nano Lett.*, 7:1113, 2007.

[81] K. Li, L. Clime, B. Cui, and T. Veres. Surface enhanced Raman scattering on long-range ordered noble-metal nanocrescent arrays. *Nanotechnology*, 19:145305, 2008.

[82] N. L. Bocchio, A. Unger, M. Álvarez, and M. Kreiter. Thin layer sensing with multipolar plasmonic resonances. *J. Phys. Chem. C*, 112:14355, 2008.

[83] P. G. Etchegoin, E. C. Le Ru, and M. Meyer. An analytic model for the optical properties of gold. *J. Chem. Phys.*, 125:164705, 2006.

[84] J. P. Berenger. Electrochemical tuning of silver nanoparticles fabricated by nanosphere lithography. *J. Comput. Phys.*, 114:185, 1994.

[85] T. Grosges, A. Vial, and D. Barchiesi. Models of near-field spectroscopic studies: comparison between finite-element and finite-difference methods. *Opt. Express*, 13:8483, 2005.

[86] S. Link and M. A. El-Sayed. Size and temperature dependence of the plasmon absorption of colloidal gold nanoparticles. *J. Phys. Chem. B.*, 103:4212, 1999.

[87] A. E. Neeves and M. H. Birnboim. Composite structures for the enhancement of nonlinear-optical susceptibility. *J. Opt. Soc. Am. B*, 6:787, 1989.

[88] S. J. Oldenburg, R. D. Averitt, S. L. Westcott, and N. J. Halas. Nanoengineering of optical resonances. *Chem. Phys. Lett.*, 288:243, 1998.

[89] C. Genet and T. W. Ebbesen. Light in tiny holes. *Nature*, 445:39, 2007.

[90] J. V. Coe, J. M. Heer, S. Teeters-Kennedy, H. Tian, and K. R. Rodriguez. Extraordinary transmission of metal films with arrays of subwavelength holes. *Annu. Rev. Phys. Chem.*, 59:179, 2008.

[91] R. Gordon, D. Sinton, K. L. Kavanagh, and A. G. Brolo. A new generation of sensors based on extraordinary optical transmission. *Acc. Chem. Res.*, 41:1049, 2008.

[92] F. Eftekhari, C. Escobedo, J. Ferreira, X. Duan, E. M. Girotto, A. G. Brolo, R. Gordon, and D. Sinton. Nanoholes as nanochannels: Flow-through plasmonic sensing. *Anal. Chem.*, 81:4308, 2009.

[93] D. Sinton, R. Gordon, and A. G. Brolo. Nanohole arrays in metal films as optofluidic elements: progress and potential. *Microfluid. Nanofluid.*, 4:107, 2008.

[94] N. P. W. Pieczonka and R. F. Aroca. Single molecule analysis by surfaced–enhanced Raman scattering. *Chem. Soc. Rev.*, 37:946, 2008.

[95] W. Wu, D. Dey, O. G. Memis, A. Katsnelson, and H. Mohseni. Fabrication of large area periodic nanostructures using nanosphere photolithography. *Nanoscale Res. Lett.*, 3:351, 2008.

[96] W. Wu, D. Dey, O. G. Memis, A. Katsnelson, and H. Mohseni. A novel self-aligned and maskless process for formation of highly uniform arrays of nanoholes and nanopillars. *Nanoscale Res. Lett.*, 3:123, 2008.

[97] J. Henzie, M. H. Lee, and T. W. Odom. Multiscale patterning of plasmonic metamaterials. *Nat. Nanotech.*, 2:549, 2007.

[98] K. L. van der Molen, K. J. Klein Koerkamp, S. Enoch, F. B. Segerink, N. F. van Hulst, and L. Kuipers. Role of shape and localized resonances in extraordinary transmission through periodic arrays of subwavelength holes: Experiment and theory. *Phys. Rev. B*, 72:045421, 2005.

[99] E. X. Jin and X. Xu. Plasmonic effects in near-field optical transmission enhancement through a single bowtie-shaped aperture. *Appl. Phys. B*, 84:3, 2006.

[100] A. Lesuffleur, L. K. S. Kumar, A. G. Brolo, K. L. Kavanagh, and R. Gordon. Apex-enhanced Raman spectroscopy using double-hole arrays in a gold film. *J. Phys. Chem. C*, 111:2347, 2007.

[101] K. L. Shuford, S. K. Gray, M. A. Ratner, and G. C. Schatz. Substrate effects on surface plasmons in single nanoholes. *Chem. Phys. Lett.*, 435:123, 2007.

[102] E.-S. Kwak, J. Henzie, S.-H. Chang, S. K. Gray, C. Schatz G, and T. W. Odom. Surface plasmon standing waves in large-area subwavelength hole arrays. *Nano Lett.*, 5:1963, 2005.

[103] W. A. Murray, S. Astilean, and W. L. Barnes. Transition from localized surface plasmon resonance to extended surface plasmon-polariton as metallic nanoparticles merge to form a periodic hole array. *Phys. Rev. B*, 69:165407, 2004.

[104] T.-H. Park, N. Mirin, J. B. Lassiter, C. L. Nehl, N. J. Halas, and P. Nordlander. Optical properties of a nanosized hole in a thin metallic film. *ACS Nano*, 2:25, 2008.

[105] J. Prikulis, P. Hanarp, L. Olofsson, D. Sutherland, and M. Käll. Optical spectroscopy of nanometric holes in thin gold films. *Nano Lett.*, 4:1003, 2004.

[106] T. Zentgraf, T. P. Meyrath, A. Seidel, S. Kaiser, and H. Giessen. Babinets principle for optical frequency metamaterials and nanoantennas. *Phys. Rev. B*, 76:033407, 2007.

[107] D. K. Gramotnev, M. W. Vogel, and M. I. Stockman. Optimized nonadiabatic nanofocusing of plasmons by tapered metal rods. *J. Appl. Phys.*, 104:034311, 2008.

[108] T. H. Taminiau, F. B. Segerink, R. J. Moerland, L. (K.) Kuipers, and N. F. Van Hulst. Near-field driving of a optical monopole antenna. *J. Opt. A*, 9:S315, 2007.

[109] V. Giannini and J. A. Sánchez-Gil. Excitation and emission enhancement of single molecule fluorescence through multiple surface-plasmon resonances on metal trimer nanoantennas. *Opt. Lett.*, 33:899, 2008.

[110] S. Chen, L. Han, A. Schülzgen, H. Li, L. Li, J. V. Moloney, and N. Peyghambarian. Local electric field enhancement and polarization effects in a surface-enhanced Raman scattering fiber sensor with chessboard nanostructure. *Opt. Express*, 16:13016, 2008.

[111] M. Li, Z. S. Zhang, X. Zhang, K. Y. Li, and X. F. Yu. Optical properties of Au/Ag core/shell nanoshuttles. *Opt. Express*, 16:14288, 2008.

[112] L. Guerrini, J. V. Garcia-Ramos, C. Domingo, and S. Sanchez-Cortes. Building highly selective hot spots in Ag nanoparticles using bifunctional viologens: application to the SERS detection of PAHs. *J. Phys. Chem. C*, 112:7527, 2008.

[113] K. Kneipp, M. Moskovits, and H. Kneipp. *Surface-Enhanced Raman Scattering: Physics and Applications*. Springer, Germany, 2006.

[114] E. Hao and G. C. Schatz. Electromagnetic fields around silver nanoparticles and dimers. *J. Chem. Phys.*, 120:357, 2004.

[115] Y. Lu, G. L. Liu, and L. P. Lee. High-density silver nanoparticle film with temperature-controllable interparticle spacing for a tunable surface enhanced Raman scattering substrate. *Nano. Lett.*, 5:5, 2005.

[116] I. Romero, J. Aizpurua, G. W. Bryant, and F. J. García de Abajo. Plasmons in nearly touching metallic nanoparticles: singular response in the limit of touching dimers. *Opt. Express*, 14:9988–9999, 2006.

[117] A. L. Lereu, G. Sanchez-Mosteiro, P. Ghenuche, R. Quidant, and N. F. Van Hulst. Individual gold dimers investigated by far- and near-field imaging. *J. Microsc.*, 229:254, 2008.

[118] H. G. Frey, F. Keilmann, A. Kriele, and R. Guckenberger. Enhancing the resolution of scanning near-field optical microscopy by a metal tip grown on an aperture probe. *App. Phys. Lett.*, 81:5030, 2002.

[119] J. Merlein et al. Nanomechanical control of an optical antenna. *Nature Photon.*, 2:230, 2008.

[120] J. K. Daniels and G. Chumanov. Nanoparticle-mirror sandwich substrates for surface-enhanced Raman scattering. *J. Phys. Chem. B*, 109:17936, 2005.

[121] K.-H. Su et al. Raman enhancement factor of a single tunable nanoplasmonic resonator. *J. Phys. Chem. B*, 110:3964, 2006.

[122] C. J. Orendorff, A. Gole, T. K. Sau, and C. J. Murphy. Surface-enhanced Raman spectroscopy of self-assembled monolayers: sandwich architecture and nanoparticle shape dependence. *Anal. Chem.*, 77:3261, 2009.

[123] V. Santhanam, J. Liu., R. Agarwal, and R. P. Andres. Self-assembly of uniform monolayer arrays of nanoparticles. *Langmuir*, 19:7881, 2003.

[124] Y. K. Hwang et al. Palladium and gold nanoparticle array films formed by using self-assembly of block copolymer. *J. Nanosci. and Nanotechnol.*, 6:1850, 2006.

[125] C. E. Talley et al. Surface-enhanced Raman scattering from individual Au nanoparticles and nanoparticle dimer substrates. *Nano. Lett.*, 5:1569, 2005.

[126] R. M. Cole et al. Understanding plasmons in nanoscale voids. *Nano. Lett.*, 7:2094, 2007.

[127] C. A. Mirkin, R. L. Letsinger, R. C. Mucic, and J. J. Storhoff. A DNA-based method for rationally assembling nanoparticles into macroscopic materials. *Nature*, 382:607–609, 1996.

[128] X. Xu, N. L. Rosi, Y. Wang, F. Huo, and C. A. Mirkin. Asymmetric functionalization of gold nanoparticles with oligonucleotides. *J. Am. Chem. Soc.*, 128(29):9286–9287, 2006.

[129] C. J. Loweth, W. B. Caldwell, X. Peng, A. P. Alivisatos, and P. G. Schultz. DNA-based assembly of gold nanocrystals. *Angew. Chem. Int. Ed.*, 38(12):1808–1812, 1999.

[130] H. Yao, C. Yi, C.-H. Tzang, J. Zhu, and M. Yang. DNA-directed self-assembly of gold nanoparticles into binary and ternary nanostructures. *Nanotechnology*, 18:015102, 2007.

[131] D. S. Sebba, J. J. Mock, D. R. Smith, T. H. LaBean, and A. A. Lazarides. Reconfigurable core-satellite nanoassemblies as molecularly-driven plasmonic switches. *Nano Lett.*, 8(7):1803–1808, 2008.

[132] S. Sadasivan, E. Dujardin, M. Li, C. J. Johnson, and S. Mann. DNA-driven assembly of mesoporous silica/gold satellite nanostructures. *Small*, 1(1):103–106, 2005.

[133] D. S. Sebba, T. H. LaBean, and A. A. Lazarides. Plasmon coupling in binary metal core-satellite assemblies. *Appl. Phys. B*, 93:69–78, 2008.

[134] C. Sönnichsen, B. M. Reinhard, J. Liphardt, and A. P. Alivisatos. A molecular ruler based on plasmon coupling of single gold and silver nanoparticles. *Nat. Biotechnol.*, 23(6):741–745, 2005.

[135] R. Elghanian, J. J. Storhoff, R. C. Mucic, R. L. Letsinger, and C. A. Mirkin. Selective colorimetric detection of polynucleotides based on the distance-dependent optical properties of gold nanoparticles. *Science*, 277:1078–1081, 1997.

[136] L. R. Hirsch, J. B. Jackson, A. Lee, N. J. Halas, and J. L. West. A whole blood immunoassay using gold nanoshells. *Anal. Chem.*, 75(10):2377–2381, 2003.

[137] G. Pellegrini, G. Mattei, V. Bello, and P. Mazzoldi. Interacting metal nanoparticles: optical properties from nanoparticle dimers to core-satellite systems. *Mater. Sci. Eng. C*, 27:1347–1350, 2007.

[138] D. S. Sebba and A. A. Lazarides. Robust detection of plasmon coupling in core-satellite nanoassemblies linked by DNA. *J. Phys. Chem. C*, 112:18331–18339, 2008.

[139] S. Kumar, J. Aaron, and K. Sokolov. Directional conjugation of antibodies to nanoparticles for synthesis of multiplexed optical contrast agents with both delivery and targeting moieties. *Nat. Protoc.*, 3:314, 2008.

[140] J.-S. Lee, A. K. R. Lytton-Jean, S. J. Hurst, and C. A. Mirkin. Silver nanoparticle-oligonucleotide conjugates based on DNA with triple cyclic disulfide moieties. *Nano Lett.*, 7:2112, 2007.

[141] P. Alivisatos. The use of nanocrystals in biological detection. *Nature Biotechnology*, 22:47, 2004.

[142] S. A. Wickline and G. M. Lanza. Nanotechnology for molecular imaging and targeted therapy. *Circulation*, 107:1092, 2003.

[143] W. C. W. Chan and S. Nie. Quantum dot bioconjugates for ultrasensitive nonisotopic detection. *Science*, 281:2016, 1998.

[144] M. Bruchez, M. Moronne, P. Gin, S. Weiss, and A. P. Alivisatos. Semiconductor nanocrystals as fluorescent biological labels. *Science*, 281:2013, 1998.

[145] P. K. Jain, I. H. El-Sayed, and M. A. El-Sayed. Au nanoparticles target cancer. *Nanotoday*, 2:18, 2007.

[146] I. H. El-Sayed, X. Huang, and M. A. El-Sayed. Surface plasmon resonance scattering and absorption of anti-EGFR antibody conjugated gold nanoparticles in cancer diagnostics: Applications in oral cancer. *Nano Lett.*, 5:830, 2005.

[147] L. A. Cantarero, J. E. Butler, and J. W. Osborne. The adsorptive characteristics of proteins for polystyrene and their significance in solid-phase immunoassays. *Anal. Biochem.*, 105:375, 1980.

[148] S. H. Im, U. Jeong, and Y Xia. Polymer hollow particles with controllable holes in their surfaces. *Nature Materials*, 4:671, 2005.

[149] C. L. Haynes and R. P. Van Duyne. Nanosphere lithography: A versatile nanofabrication tool for studies of size-dependent nanoparticle optics. *J. Phys. Chem. B*, 105:5599, 2001.

[150] P. Hanarp, M. Kall, and D. S. Sutherland. Optical properties of short range ordered arrays of nanometer gold disks prepared by colloidal lithography. *J. Phys. Chem. B*, 107:5768, 2003.

[151] Tatiana V. Teperik and Vyacheslav V. Popov. Strong coupling of light to flat metals via a buried nanovoid lattice: the interplay of localized and free plasmons. *Opt. Express*, 14:1965, 2006.

[152] C. L. Cheung, R. J. Nikoli, C. E. Reinhardt, and T. F. Wang. Fabrication of nanopillars by nanosphere lithography. *Nanotechnology*, 17:1339, 2006.

[153] H. Rochholz, N. Bocchio, and M. Kreiter. Tuning resonances on crescent-shaped noble-metal nanoparticles. *New J. Phys.*, 9:1, 2007.

[154] L. Y. Wu, B. M. Ross, and L. P. Lee. Optical properties of the crescent-shaped nanohole antenna. *Nano Lett.*, 9:1956, 2009.

[155] C. Haginoya, M. Ishibashi, and K. Koike. Nanostructure array fabrication with a size-controllable natural lithography. *New J. Phys.*, 71:2934, 1997.

[156] J. T. Drotar, Y.-P. Zhao, T.-M. Lu, and G.-C. Wang. Surface roughening in shadowing growth and etching in 2+1 dimensions. *Phys. Rev. B*, 62:2118, 2000.

[157] J. T. Drotar, Y.-P. Zhao, T.-M. Lu, and G.-C. Wang. Mechanisms for plasma and reactive ion etch-front roughening. *Phys. Rev. B*, 61:3012, 2000.

[158] E. C. Le Ru, P. G. Etchegoin, J. Grand, N. Félidj, J. Aubard, G. Lévi, A. Hohenau, and J. R. Krenn. Surface enhanced Raman spectroscopy on nanolithography-prepared substrates. *Curr. Appl. Phys.*, 8:467, 2008.

[159] M. Baia, L. Baia, and S. Astilean. Gold nanostructured films deposited on polystyrene colloidal crystal templates for surface-enhanced Raman spectroscopy. *Chem. Phys. Lett.*, 404:2005, 3.

[160] S. C. Wuanga, K. G. Neoha, E. Kanga, D. W. Packb, and D. E. Leckband. HER-2-mediated endocytosis of magnetic nanospheres and the implications in cell targeting and particle magnetization. *Biomaterials*, 14:2270, 2008.